Flow and Particle Transport by the Lattice Boltzmann Method

by

YIGUANG YAN

A Dissertation Submitted to the Graduate Faculty in
Engineering in Partial Fulfillment of the Requirements for the
Degree of Doctor of Philosophy

The City University of New York

2008

UMI Number: 3310592

INFORMATION TO USERS

The quality of this reproduction is dependent upon the quality of the copy submitted. Broken or indistinct print, colored or poor quality illustrations and photographs, print bleed-through, substandard margins, and improper alignment can adversely affect reproduction.

In the unlikely event that the author did not send a complete manuscript and there are missing pages, these will be noted. Also, if unauthorized copyright material had to be removed, a note will indicate the deletion.

UMI®

UMI Microform 3310592
Copyright 2008 by ProQuest LLC
All rights reserved. This microform edition is protected against
unauthorized copying under Title 17, United States Code.

ProQuest LLC
789 East Eisenhower Parkway
P.O. Box 1346
Ann Arbor, MI 48106-1346

This manuscript has been read and accepted for the Graduate Faculty in Engineering in satisfaction of the dissertation requirement for the degree of Doctor of Philosophy.

Date	Prof. Joel Koplik Chairman of Examining Committee
Date	Prof. Mumtaz Kassir Executive Officer

Prof. Joel Koplik (Mentor)

Prof. Jeffrey Morris (Co-Mentor)

Prof. Morton Denn

Prof. Yannis Andreopoulos

Prof. Peter Ganatos

Supervisory Committee

THE CITY UNIVERSITY OF NEW YORK

Abstract

Flow and Particle Transport by the Lattice Boltzmann Method

by

Yiguang Yan

Advisor: Prof. Joel Koplik

Three problems involving lattice Boltzmann computations of confined fluid flow and particle transport are studied. First, the flow of shear-thinning and shear-thickening non-Newtonian fluids at finite Reynolds numbers in self-affine fracture channels is considered. Such flows are relevant to the modeling of hydrocarbon recovery processes in geological fracture networks. Microscopic aspects of the flow fields and macroscopic properties such as permeability are obtained under a variety of flow conditions, and the results may be summarized in a number of scaling relationships. Secondly, we study suspension dynamics and particle deposition due to gravity in finite Reynolds number channel flows. The local velocity and concentration fields in the Hele-Shaw case flow domain are found, along with macroscopic characterizations such as fluid flux and particle flux as functions of the control parameters Reynolds number, buoyancy number and bulk suspension concentration. An initial study of the surface evolution of self-affine fracture walls is made, which suggests that height correlations are partially preserved in deposition processes. Lastly, we investigate two-particle hydrodynamic interactions in confined shear flow with finite fluid inertia. The particle trajectories are determined as a function of the initial and flow conditions, and a “phase diagram” of final states is obtained. A variety of fixed point and open and closed limit cycle behaviors are observed, and the results related to particle train and cluster formation in shear and Poiseuille suspension flows.

Acknowledgments

First and foremost, I would like to thank my advisor Prof. Joel Koplik for his unflinching support and guidance throughout my PhD research work. He has been an excellent mentor and above all a good friend. I immensely enjoyed working with him and feel very fortunate to have him as my PhD advisor. I also would like to thank Prof. Jeffrey Morris, my co-advisor for his patient and extensive discussions on my research. I learned a lot from him and I really enjoyed talking with him on all things as a good friend.

Next, I would like to thank my PhD committee members Prof. Denn Morton, Prof. Yannis Andreopoulos and Prof. Peter Ganatos for providing me valuable suggestions and feedback during the duration of my PhD. A special thanks goes to my research colleagues Dr. German Drazer, Dr. Tak-shing Lo, Prof. Charles Maldarelli, Prof. Mark Shattuck and Prof. Taehun Lee for their generous assistance in my research activities and motivating me to do the best.

I thank all my colleagues and friends at Levich Institute or City College: Pengtao Yue, Junjun Mao, Mary Wright, Junming Shi, Zhou Xu, Fenfen, Xiujuan, Jiaju, Rajesh, Parsa, Andy, and many more for their enthusiasm, support and motivation during my PhD, and also for making my life exciting and fun filled during the course of my five and half year stay at CCNY.

Finally, I would like to dedicate this thesis to my parents, Mr. Wenchao Yan and Mrs. Shunming Li, and my wife, Yunyun Zou. It is the result of their enduring and continuous efforts, love and support that I have been able to undertake this task and do justice to it. They gave me the freedom to choose my career path and always encouraged me to achieve higher and higher goals in life.

Contents

List of Figures

List of Tables

Chapter 1

Introduction

1.1 Introduction

Fluid flow and solid particle transport occurs in many industrial processes in the chemical, petroleum, geothermal and environmental processing industries, and so transport processes involving fluid flow have been investigated by many researchers. in particular, fluid flow in geologically disordered media such as subsurface porous reservoirs and fracture channels and networks has attracted a lot of attention due to current energy-related issues. Much research has been therefore been conducted on flow and chemical transport in such systems using a variety of theoretical, computational and experimental techniques. Flow and transport problems in geological disordered media have been addressed mainly in two directions: microscopical modeling and macroscopic correlation. Microscopically, it is of interest to investigate geometrical effects on fluid and transport of other materials, to analyze the different mechanisms for fluid and particle transport, and to compute the details of transport at the constituent level. Macroscopically, the fluid flow rate and pressure values are closely related to production efficiency in processes such as hydrocarbon recovery, and especially for secondary oil recovery. In this thesis, we will focus on flow and other particle transport processes in fractures and in an model systems which are a reasonable approximation to natural fracture channels.

The presence of fractures in geological disordered media such as porous hydrocarbon and water reservoirs, waste repositories, or geothermal sources, has important consequences for the utilization of our energy resources. The motion of energy, fluids and suspended particles may occur predominantly through fracture networks, since these can be more permeable than the microscopic pore system within sedimentary rocks, providing higher throughput rates over longer distances, and can be the dominant mechanism for energy and material transport. In contrast to the relative well-understood case of motion through microscopically porous media, the problem of understanding transport in fractures has several additional technical difficulties, related to correlations both between and within individual fractures[7]. The key simplifying feature in the first case is that the heterogeneities within the pore system of a rock usually have only short range correlations, and straightforward average or mean-field descriptions such as Darcy's law work very well. Problems on larger scales, where other types of heterogeneity occur, may then be treated by using continuum partial differential equation models to consolidate the behavior of individual statistical homogeneous regions. The exceptions, such as long-time tails in dispersion, or more generally two-phase flow, involve longer-ranged correlations in the pore space geometry or the spatial distribution of the fluids. For fractures, there are again "uncorrelated " problems which are well understood, such as the flow of fluids in a single smooth fracture, but for the more challenging questions of transport, spatial variations and their correlations play a crucial role[26, 27, 28].

Although the surface of a naturally fractured rock appears superficially to have merely some random roughness, on careful analysis it is actually a self-affine structure, have a statistical self-similarity extending over decades of distance, characterized by a roughness exponent[7][55] [70]. This thesis focuses on an equally challenging and significant problem at an intermediate scale—the effects of the correlated heterogeneities present within a single rough fracture. A very crucial issue for fluid transport in geological fracture systems is the evolution of their geometry due to the deposition of particles carried by flowing fluids. (There are other mechanisms acting, such as erosion, but their effects occur over very long time scales.) Fine particles such as silt can gradually deposit along fractures and narrow the aperture, and larger particles may deposit and partially block the flow in a fracture or a flowing junction. Such processes may significantly alter the transport properties of a reservoir over "working" time intervals, and have a major impact on the efficiency with which hydrocarbon or water may be recovered. In these situations, one would like to develop diagnostic or predictive tools which allow the effects of fractures to be quantitatively incorporated in reservoir evaluation and modeling.

The understanding of flow and transport in fractures is a non-trivial problem due to the irregularity and roughness of the surfaces of a fracture channel. While this is the major issue we wish to attack, in practice in the petroleum, chemical and related industries, the liquids flowing in disordered media are very often non-Newtonian fluids. A further topic to be investigated is then non-Newtonian fluid flow in geological disordered media, and here we will focus on their flow in self-affine fracture channels. An additional complication is that mobile solid particles are present in many geological and chemical processes and understanding their transport dynamics during processing is important for proper design and prediction. It is thus of equal interest to address this fluid-solid multiphase flow problem. Moreover, because many transport processes in natural and industrial contexts involve high values of fluid flux, the effects of fluid and particle inertia, or even high Reynolds number turbulent flow, become relevant. This motivates our final topic, particle interactions including the effects of inertia. Based on these considerations, in this thesis we address the following transport problems in fractures:

- Investigate non-Newtonian fluid flow in self-affine fractures. Many fluids in industrial processes are non-Newtonian, that is, the viscosity of the fluid is dependent on the local shear rate, or in some cases exhibits memory effects whereby the viscosity depends on the history of the local deformation of the fluid element. As a starting point, It is appropriate to investigate non-Newtonian fluid flow in a single fracture channel, as a prelude to future work on flows in a network of fracture channels or a porous medium. Moreover, a further motivation for this study is the fact that a fluid containing solid particles or a polymer solution or melt often has some shear thinning or thickening rheological behavior even the solvent itself is Newtonian.

- Study the two-particle interaction problem for fluids with finite inertia, in order to develop some insight into experimental and computational results on this problem, and also to build a data set to extend particulate modeling to particle suspensions or other particle transport processes. A substantial literature exists on the effects of finite fluid inertia on particle trajectories, which may help explain experimental observations of particle migration and particle-train formation. Fluid inertia is known to cause particle migration across streamlines, and hence produce interesting new phenomena.
- Study particle suspension and deposition process in pressure-driven fluid flows in both flat and rough single fracture channels. In addition to simulations at the particle level, it is important to investigate the rheology of particulate suspensions and try to model them as bulk continuous materials. Both the microscopic description and the macroscopic modeling facilitate our ability to predict and design industrial process where particulate suspension flow is involved.

The following sections take up the three topics in turn, and provide a review of previous literature on the topic, elaborate on the state of current research and the difficulties present in the subject. The detailed results are given below in separate chapters for each topic.

The principal computational tool to be employed in this thesis will be the lattice Boltzmann (LB) method, which is particularly convenient in situations where an irregular boundary shape changes systematically. The advantage of this method is that since the solid boundary is a set of nodes where fictitious particles moving on a lattice bounce back to keep the right boundary conditions, or using more exact and sophisticated rules. The evolution of the fracture surface simply corresponds to updating a list of such sites. Recent papers[3][19] [32][33][39] [47][73] have shown the utility of this technique in a number of related problems such as suspension dynamics and porous media flow. These numerical results will then be compared to both the simpler models discussed above, and the results of a purely continuum description in terms of surface adsorption rates. We will discuss more on lattice Boltzmann method in next chapter with validations on our computational results.

1.2 Fluid flow in self-affine fracture channels

An understanding of flow and transport processes in geologically disordered media is necessary for the efficient extraction of fluids from underground hydrocarbon reservoirs. Situations where flow proceeds through networks of connected fractures are particularly attractive, because the throughput is generally much higher than may be achieved through intergranular porosity alone [1, 8, 67, 80]. An important feature of subsurface fractures, which considerably complicates the problem, is that the surfaces of naturally fractured rocks are not smooth or even randomly rough, but rather are highly correlated self-affine fractals [11]. A second complication in the analysis is that typical reservoir fluids are often complicated mixtures, which exhibit non-Newtonian flow behaviors such as shear-thinning or shear-thickening. Yet a third difficulty is that the subsurface fracture flow often involves much higher velocities than in the intergranular case, and the common simplification of low-Reynolds number linear flow is inapplicable.

The first ingredient in this study of transport in fractured materials is the characterization of flow heterogeneities in a single fracture with rough walls [44]. In this case the local aperture varies spatially, so that the velocity field occurring when the fracture is saturated with fluid is not uniform, and the nature and spatial correlation of the velocity distribution strongly depend on both the shape of the fractured surface and the relative displacement of the two fracture faces[26][28]. Once the velocity field is understood, one can proceed to analyze the dependence of dispersion on the geometrical parameters of the fractures. The importance of passive-tracer dispersion as a diagnostic tool is that it is a particularly sensitive technique to analyze heterogeneities[27], since measurable transit time distributions obtained with these techniques depend on the integral of the flow velocity deviations along the full path of each individual particle. Moreover, understanding this case is a necessary preliminary to the study of particle suspension and deposition (or active dispersion processes), where for example advected particles change the flow field as they transport. The latter case, which is of great importance in practice, will be considered later.

Numerous experiments and calculations have been conducted to elucidate the combined effects of geometrical complexity, non-Newtonian rheology and finite inertia in fluid flow through a single Hele-Shaw cell, fracture channel or porous medium. Previous authors have considered subsets of these complications, but not all three simultaneously. The flow of Newtonian fluids in self-affine fractures at both low [26][28] and finite [38] Re has an extensive literature. Some controlled experiments on shear-thinning fluids in self-affine fractures at low Re have been reported [9]. Lastly, experiments and phenomenological models for non-linear fluid motion in intergranular porous media at various Re are available [21]. We anticipate that flow in a fracture can be characterized in a manner similar to the latter problem, since in both cases the key effect is that the random solid boundary of the flow domain causes streamlines to wind around, roughly following the boundary. One simplification which we *can* exploit, however, is to focus on two-dimensional flows. It is well known that the flow of a single fluid in a straight channel differs only in detail between two and three-dimensional cases, and furthermore, in porous media flow in the analogous intergranular case, one sees the same flow laws for both two and three dimensional geometries.

The approach taken in the research follows the lines of previous studies of permeability [26] and transport [28] in self-affine fractures based on the lattice-Boltzmann method, along with a procedure for incorporating power-law viscosity variation similar to that developed previously [34]. The discussion of inertial effects is influenced by previous studies for the case of a Newtonian fluid in intergranular porous media [38]. The fracture surface is generated numerically by a Fourier transform algorithm and discretized on the regular lattice used in the flow problem. The upper and lower fracture surfaces bound the allowed nodes in the flow domain, a bounce-back condition enforces the no-slip boundary condition, and constant forcing provides a pressure-driven flow. For power-law fluids, the lattice-Boltzmann relaxation time is adjusted locally in space and time to provide the desired relation between stress and strain. The relation between imposed pressure drop and total fluid flux provides the permeability, and the local flow fields are analyzed to determine the velocity, pressure and shear stress variations. Some background on the flow geometry and calculational method is presented in Chapter 3.

1.3 Microscopic analysis of pair particle interaction at finite Reynolds number

The finite Reynolds number interaction between particles in confined shear flows is a basic if largely unexplored problem, and a fundamental ingredient in the dynamics of multi-particle suspensions. A key issue in suspension mechanics is to develop an understanding of the role of particle-scale forces in determining macroscopic behavior, and the principal difficulty is their long-ranged nature: $\sim 1/r$ for forced and $\sim 1/r^2$ for force-free particles in unbounded three dimensional flow. In unbounded two dimensional Stokes flow, the unforced particle generates a flow which scales as $1/r$ while a body generating a force results in a flow which scales as $\ln r$ and thus does not exist (Whitehead's paradox). Aside from the dilute limit, the motion is therefore intrinsically a difficult many-body problem which numerical calculations have begun to explore. Most of the available results concern the creeping flow limit, but finite Reynolds number inertial effects are present in many applications, and are known to dramatically affect flow behavior even at the single particle level. In this article, we investigate the pair interactions between two solid particles in an otherwise simple linear shear flow. For reasons of computational practicality, we focus on cylindrical particles in flows with only a two-dimensional variation, but also present some results for spherical particles in three dimensions.

The study of hydrodynamically-interacting systems has largely focused on low-Reynolds-number flows, meaning vanishing values of $Re_p = Ua/\nu$, the particle-scale Reynolds number defined in terms of the particle size, a (*e.g.*, radius if spherical), a relevant microscale velocity, U, and ν, the kinematic velocity of the fluid. This limit allows one to consider the fluid mechanics as governed by the linear and quasistatic steady Stokes equations; some, but considerably less, investigation of conditions for which the unsteady Stokes equations apply has been reported for suspensions.

If inertia is neglected entirely, it is well-known that the motion of the system of particles (and macroscopic boundaries if these are considered) is entirely dependent on the configuration and the applied forces at the instant considered. That means there is no history dependence except in setting the configuration, and viewed as a dynamical system, the suspension has no momentum degrees of freedom.

While the vast majority of suspension mechanical studies have addressed inertia-less conditions, there are several studies at finite Re_p which we will discuss. Before turning to these, we note that studies have been made of the role of finite particle inertia for conditions where the fluid inertia is negligible, conditions which may be approximately achieved in a particle laden-gas at $Re_p \ll 1$ if the Stokes number $St_p = (\rho_p/\rho_f)Re_p = O(1)$. This requires the ratio of particle to gas density be large and appears difficult to replicate experimentally in a uniformly dispersed system in normal gravity. However, it is interesting to note that Subramanian & Brady [84] analyzed such a system in an unbounded simple shear flow and found that the weak inertia associated with the particles results in very basic changes in the relative motion of particle pairs, with the closed pair trajectories present in the $St_p = Re_p = 0$ limit (Batchelor & Green [4]) lost at finite inertia, and appearance of new attractor states.

This study of simple shear flow of a pair of particles at finite St_p raises the question of what is the pair trajectory in unbounded shear flow of two neutrally-buoyant particles at finite $Re_p = \dot{\gamma}a^2/\nu$ (where $\dot{\gamma}$ is the shear rate)? In fact, the answer is not known for unbounded flow and only a very unsatisfactory partial answer may be given for wall-bounded shear flows. While methods have been developed for simulation of the motion of interacting particles at finite inertia, these have yet to address this basic question. Finite-element methods have been applied to inertial effects for sedimenting particles (with $Re_p = Ua/\nu$, U a characteristic settling speed), with examinations showing the now well-known drafting-kissing-tumbling sequence [30].

Larger numbers of particles sedimenting at finite inertia have also been considered by Patankar & Hu [68]. Lattice-Boltzmann techniques have also been applied to interacting particles in sedimentation at finite Re_p by Aidun & Ding [2] and Qi [76].

Shear flow studies of suspended particles at finite Re_p are relatively sparse, but for isolated particles date to the analytical study of Lin, Peery & Schowalter [51] which examined by matched asymptotics the Newtonian fluid flow around a sphere. This work showed that the symmetry-breaking by inertia results in a particle contribution to the stress which is non-Newtonian, and includes normal stress differences of $O(Re_p)$, a result which was shown for larger Re_p by numerical approaches applied to a cylinder [69] and sphere [59]. Numerical [46][23] and experimental [71] studies of shear flow around isolated freely-rotating (torque-free) circular cylinders revealed that the streamlines undergo a marked change with introduction of inertia, as the closed streamline region of Stokes flow collapses and a reverse flow zone appears, as discussed in detail by Mikulencak & Morris [59] for both cylinder and sphere. The reversal is such that a streamline approaching the particle, taken as centered at the origin, from the quadrant $x < 0, y > 0$ in the shear flow $U_x = \dot{\gamma} y$ crosses $y = 0$ as it approaches the particle, and recedes into the quadrant $x < 0, y < 0$, rather than passing "over" the particle and receding into $x < 0, y > 0$ as one would observe for Stokes flow. A recent study by Subramanian and Koch[85] showed that the closed streamlines around a freely-rotating sphere in Stokes flow give way at *any* finite Re_p to spiraling streamlines; in the shear plane, these streamlines spiral out away from the body, and there is an accompanying spiraling in-flow along the vorticity axis. Considering a second particle rather than fluid moving relative to the particle at the origin, these flow structures have implications for particle interactions, as noted below in discussion of recent experiments on tube flow of inertial suspensions. In fact, in a separate study of three-dimensional pair-sphere trajectories by Kulkarni and Morris, reversing and spiraling trajectories of one sphere relative to the other are seen as well.

Poiseuille flows of many suspended particles at finite Re_p have been considered numerically by Huang and Joseph [41] and Lin *et al.* [52] using finite-element methods, but the issue of pair trajectories remains unresolved. Simulated Couette flow of pairs of particles by the lattice-Boltzmann technique in wall-bounded channels by Poesio *et al.* [72] shows symmetry breaking but is limited in the range of initial relative positions and Re_p considered. We seek to advance the state of understanding of the hydrodynamic interaction of pairs of particles at finite shear-flow Re_p here, also considering a wall-bounded Couette flow. We note that shear flow with $Re_p = O(1)$ and without boundary effects – *i.e.* such that it is effectively unbounded – is not readily physically realized: as the distance to the walls increases the bulk Reynolds number as the square of l/d where l is the channel (or tube) dimension across the flow in the experiment and $d = 2a$ is the particle diameter, so that one is limited in l/d values one may consider while maintaining stability (Bottin *et al.* [10] give the stability of the channel flow as $\dot{\gamma} l^2/\nu \approx 1500$). However, $l/d = O(10)$ is accessible for $Re_p = O(1)$, although particles alter the stability threshold [56].

It is well-known that inertia influences individual particles in pressure-driven flows by driving cross-stream migration as shown by Segré & Silberberg [82] and explored for higher inertia by Matas, Morris and Guazzelli [43]. Particles take up a preferred radial position with center at approximately $r/R = 0.6$ for $Re_c \ll 1$ and moving progressively outward as Re_c increases (Re_c is the channel or tube scale Re). Some experimental evidence for hydrodynamic interactions among neutrally-buoyant particles in these pressure-driven flows is seen in the formation of "trains" of particles near the wall of the pressure-driven flow, even at conditions of less than 1% solids by volume. These long-lived linear structures consist of many (up to about 50 having been observed in a single train), uniformly-spaced particles which move together for large axial distances [42]. The particle separation is found to decrease with Re_p in a manner which suggests that the train formation is related to the flow induced by one particle in finite-inertia shear, as a particle causes the noted reversal of streamline direction, but a second particle following such a streamline is cut off from receding by the wall – we note that the train formation is observed under conditions where inertial migration has driven the preferred radial position quite near the wall. The axial separation of particles within a train having a dependence on Re_p can thus be argued to result from the collapse of the spiraling region around a particle, which scales roughly as ${Re_p}^{-1/2}$ up to $Re_p = O(1)$. Chun and Ladd [22] have used lattice-Boltzmann techniques to explore this phenomenon and find certain similar behavior, albeit in a square duct rather than a circular tube. The evidence for hydrodynamic interactions with clear inertial influence impacting upon the microstructure at small particle loadings provides the motivation to explore the pair interaction in inertial shear flow. In the present work, we focus on particles interacting within a planar Couette flow, where inertia drives an individual particle to migrate to the centerline of the flow [31].

To attack this problem, the lattice Boltzmann method has been utilized to calculate pair particle interaction in a simple shear flow with finite fluid inertia. We will give the analysis of pair particle trajectories and their dynamics in Chapter 5.

1.4 Particulate transport and deposition

Fluids flowing through geological media are rarely clean, and often contain solid particles whose size ranges from colloidal upwards. If these solids remained in the fluid, one might hope to model transport processes adequately by using effective suspension properties, but in fact there is substantial particulate exchange between the fluids and the rock surfaces which bound them. Planar smooth surfaces often develop roughness or wave-like structures as particle are entrained and deposited, while surface roughness could be either smoothed or enhanced, depending on the relative strengths of adhesion and shear forces, and the effects of collisions. Here we will focus on the microscopic analysis of the particle suspension and deposition in a Newtonian fluid media, and also investigate macroscopic properties such as permeability and evolution of the fractures, asking whether they tend to become more or less rough, and quantitatively determine the way in which they change shape as particle-laden fluid flows past them. In the particular case of the self-affine rock surfaces emphasized here, the fractal correlations originate during the fracture process itself, and it is natural to study if and how these surface characteristics evolve.

There are two distinct domains to consider, with different experimental and theoretical procedures for each, depending on the suspended particle size. Very small(colloidal) particles in suspension might perhaps be regarded as making up an effective fluid mixture or slurry, and modeled accordingly, and the complementary experiments would focus on average properties of the fracture surface and the flow network as deposition occurs. Large particles, in contrast, would be modeled as discrete units present in a flowing fluid, and in experiments one would wish to observe their individual motions as well. We expect that colloidal particles adhere to the surface locally due to microscopic interaction such as van der Waals force, whereas larger ones are controlled by geometrical constraints involving the shape of the surface and the particle size, as affected by gravity and hydrodynamic shear forces and other long range forces. Most existing work in this area takes a continuum approach, using reaction terms in an advection-diffusion equation to account for surface evolution, but we will use a more microscopic, particle-level description. Similar to some simplified treatment for porous media, we could use connected Hele-Shaw cells to simulate a porous media or network of fracture channels, so it is interesting in itself and valuable in modeling to investigate the particle suspension and deposition processes in a single Hele-Shaw cell firstly. Much effort has been put into this problem, for colloidal and non-colloidal particle transport in a Newtonian fluid.

For colloidal particles, we would treat the fluid as an effective continuum with non-Newtonian properties, as in the study of tracer dispersion in shear-thinning fluid described above, where the properties of the fluid are related to the local particle concentration. The new feature here is that there is effectively an *active* tracer—as the particle deposit on the fracture surface, their concentration changes, and the fluid properties change in tandem. The mechanism for particle attachment originates in short-ranged (van der Waals) and longer-ranged (electrostatic) interparticle forces, and given the small size of the particles, would not have high sensitivity to the details of the flow field. The modeling assumption controlling surface evolution in this case would then be that of a constant attachment probability for particles adjacent to the wall[39].

In the case of larger, non-colloidal, suspended particles, there is no longer a sharp contrast between the particle size and the length scale associated with the surface roughness. The continuum approximation may not suffice in narrow fractures, and furthermore hydrodynamic forces can vary significantly with the local shape of the fracture surface. It is then more appropriate to compute the detailed flow field around a particle near the surface, from which realistic hydrodynamic forces may be obtained. The variation of the local behavior with the detailed shape of the surface and the position of a nearby particle is then built into the calculation, as required here. In this situation, we are considering particles large enough that hydrodynamic and gravity forces are dominant, and furthermore it is known that surface roughness effects play a significant role in their degree of contact with the fracture walls. In the numerical calculations, some degree of surface roughness arises from the presence of a lattice[79], but it is not clear how well realistic physical effects are captured in this way. Fortunately, experimental studies of the effects of realistic surface roughness on particle dynamics in a viscous fluid are available in the literature, so it is possible to test our numerical procedure and, if they are found to be inadequate, add appropriate additional force and torque contributions.

The limited computational ability of numerical computations to capture the deposition process in a complete fracture with self-affine roughness over decades of surface lengths remains to be seen. Aside from the memory requirements associated with a large-scale high resolution calculation, the physical time required for thin liquid films to drain from the gap between approaching solids can be large. An alternative procedure is to follow the way of investigating the sphere pack filtration work. We would first perform local calculations at the level of a manageable small number of roughness elements. These results would provide local trapping rules to be inserted into a network simulation of the type described above, which could address the evolution of the change in the shape of the fracture wall, as a function of time, over length scales approaching the continuum regime.

A lot of efforts have been put into viscous suspension flow falling in the Stokes regime, where the fluid inertia effect is negligible, for Brownian and non-Brownian particles suspended in low Reynolds number fluid flows. At low Reynolds number, particles migrate due to the shear distribution in the flow field. Gadala-Maria and Acrivos(1980)[35] and Leighton and Acrivos(1987)[50] have shown that the particles migrate from high shear to low shear regions in a simple shear flow geometry. After their study, shear induced particle migration has been further investigated for different flow configurations. Lyon and Leal(1997)[53] have described some experiments on mono-disperse and bi-disperse neutrally buoyant particle suspension in low Reynolds number flow between two flat plates using modified laser-Doppler velocimetry (LDV). Their measurements show that for systems with channel width to particle diameter between 11 to 24 and bulk particle fraction between 0.3 to 0.5, particles migrate to the center of the channel,and the migration effect is more apparent for high bulk particle concentration. And in their systems, for bi-disperse suspension, they found that particles segregate and more larger particles in the center of the channel, especially at lower bulk concentration. Hampton et al(1997)[37] also used nuclear magnetic resonance imaging(NMRI) to measure flow velocity field and concentration profiles of a pressure driven pipe flow, for different bulk particle concentration and ratio of particle diameter to pipe diameter. They observed that for large concentrations, particles migrate to the center of the pipe, and the concentration profile becomes blunter with increasing bulk concentration. Butler and Bonnecaze[14] also show that neutrally-buoyant particles in a pressure driven tube flow migrate to the low shear center of the tube through electrical impedance tomography(EIT) in a non-invasive manner.

Apart from these experimental investigations, theoretical and computational studies have also been set up for particulate pressure driven flow at low Reynolds number. Stokesian dynamics(SD) has been used to simulate suspension pressure driven flow by Nott and Brady[12]. They showed that for multiple particle suspension flow, the particle migration is irreversible even without surface roughness. They also proposed a suspension balance model for pressure driven suspension flow based on insights from their Stokesian dynamics simulations. Leighton and Acrivos(1987)[50] also proposed a diffusion flux model, which describes particle migration as a hydrodynamic diffusion process, while the suspension balance model is based on particle migration due to normal particle stress. In diffusive model, two mechanisms count for the particle redistribution, one is particle concentration gradient, and the other is shear induced particle migration. In suspension balance model, Nott & Brady[12] and Boulay & Morris[61] set up mass and momentum balance for bulk material and particle phase, with proposed rheological properties for particle suspensions. They found good agreement between the results from the model and the Stokesian dynamics simulations for monodisperse neutrally buoyant particle suspension. Miller and Morris[60] developed this suspension balance model for concentrated suspension pressure driven flow for axial development in a tube.

Recently, neutrally-buoyant particle suspensions in finite Reynolds number flow with fluid inertia have attracted a lot of attention. For particle suspensions in a pressure driven tube flow at finite Reynolds number, Matas, Morris and Guazzelli[43] have investigated particle migration and pattern formation, finding that with inertia particles migrate to somewhere between the center of the tube and the wall. With higher particle Reynolds number, or larger fluid inertia, they found [43] that the peak particle concentration position drifts closer to the wall away from the centerline of the tube. They also found [42] that at finite Reynolds number, particles could form a train along the main flow stream. The train formation process was simulated by Chun and Ladd [22] for a pressure-driven particle suspension in a rectangular prism channel, who found that particle chains form either along the centerline of the channel, close to the wall surface, or at the corner of two walls, and also observed that for different channel Reynolds numbers a single particle has different stable and unstable equilibrium positions. Yan, Morris and Koplik[92] have tried to explain this particle train formation by investigating pair particle interaction at finite Reynolds number in a simple shear flow. They found that different pair particle trajectory patterns form for different particle Reynolds number and different initial particle configurations. On the other hand, non-colloidal particles heavier than the continuous fluid phase tend to sediment out of the suspension and to deposit onto the lower bounding surface. When particles in a pressure-driven suspension flow settle, those particles are subject to gravity and interact with each other through hydrodynamic forces. The hydrodynamic force is long-range, decaying asymptotically as the inverse of the distance between particles, and drives large fluctuations in the particle velocity and concentration distribution,s and the gravitational force suppresses this fluctuation.

Other groups have focused on transport phenomena in non-neutrally buoyant particle suspensions under different operating conditions, subject to these same two competing factors. Morris and Brady[62] have investigated pressure-driven flow of a suspension with buoyancy effects in low Reynolds number flow, for different buoyancy numbers and different flow geometries. Norman, Nayak and Bonnecaze[65] used electrical impedance tomography to study migration of buoyant particles in a low Reynolds number pressure driven tube flow. They explained the particle distribution along the fluid tube in a manner consistent with the experimental measurements. Charru et al[17] investigated erosion and deposition of particles on a particle bed sheared by a viscous linear shear flow. In their experiments, they found that there is a critical shear rate and hence a critical Shields number (the ratio between the viscous lift force and gravitational force) needed for particles to be resuspended from the particle bed. The number of moving particles transported along the particle bed surface depends linearly on the shear rate. Charru and Hinch[15, 16] also studied ripple formation on a particle bed sheared by steady simple shear and by oscillating flows using an erosion-deposition model based on the experimentally displayed relation between the particle transport rate and local shear rate.

Chapter 2

Introduction to lattice Boltzmann method

In the last twenty years or so, the lattice Boltzmann method(LBM) has been developed as a and promising numerical technique for flows and other transport phenomena in fluids, providing an alternative to traditional computational fluid dynamics(CFD) methods. Unlike conventional numerical methods based on macroscopic continuum equations, the lattice Boltzmann method is developed from microscopic models and mesoscopic kinetic equations[19][91][77].

2.1 Basic idea

The fact that different microscopic interactions can lead to the same form of macroscopic equations is the starting point for the development of lattice gas cellular automata(LGCA) or LBM. In addition to real gases or real liquids, one may consider artificial micro-worlds of particles "living" on lattices that conserve mass and momentum. The microdynamics of these particles should contain enough but not too much information to get the macroscopic equations, in this case, the Navier-

Stokes equations. Furthermore, it should be very simple to run efficiently on a computer. Consider, for example, a square lattice with four cells at each node such that one cell is associated with each link to the next neighbor node. These cells may be empty or occupied by at most one particle with unit mass $m = 1$. Thus each cell has only two possible states, this is called a *cellular automata.* Velocities and thereby also momentum can be assigned to each particle by the vector connecting the node to its next neighbor node along the link where the particle is located. These velocities are called lattice velocities. The microscopic interaction is strictly confined to local region in that it involves only particles at a single node or several neighbor nodes. The particles exchange momentum while conserving the mass and momentum summed up over every node. After this collision each particle propagates along its associated link to its next neighbor node. The microdynamics consists of a repetition of collision and propagation steps. Macroscopic values of mass and momentum density are calculated by *coarse graining* (calculation of mean values over large spatial regions with hundreds to thousands of nodes).

Instead of individual particles (that is to say, a Boolean variable associated with a given velocity at a given time and lattice node) in LGCA, an LBM deals with continuous distribution functions which interact locally (only distributions at a single node are involved) and which propagate or stream after collision to the next neighbor node[18]. in this way, the statistical noise in the LBM can be eliminated. Another important simplification of the LBM over the LGCA, introduced by Higuera and Jiménez(1989), is the linearization of the collision operator using a single relaxation time(BGK scheme), assuming that the distribution is close to the local equilibrium state[19]. This gives much more flexibility to LBMs, leads to Galilei invariant macroscopic equations without scaling of time, and allows the tuning of viscosity.

2.2 Lattice Boltzmann models

2.2.1 Lattice Boltzmann equations

There are several ways to obtain the lattice Boltzmann equation(LBE) from either discrete velocity models or the Boltzmann kinetic equation and also several ways to derive Navier-Stokes equations from the LBE[19][91]. Here we start with the LBGK equation which is most commonly used in this literature:

$$f_{\sigma i}(\mathbf{x}+\mathbf{e}_{\sigma i}\triangle t, t+\triangle t) - f_{\sigma i}(\mathbf{x},t) = -\frac{1}{\tau}\left[f_{\sigma i}(\mathbf{x},t) - f_{\sigma i}^{eq}(\mathbf{x},t)\right], \tag{2.1}$$

For simplicity, we will let $\triangle x = \mathbf{e}_{\sigma i}\triangle t$,$\triangle t = 1$ be the spacing and time step. f_i is the particle velocity distribution function along the ith direction, $\mathbf{x}$ is the coordinates of the virtual particle residing on the lattice nodes,and $\mathbf{e}_{\sigma i}$ are the particle velocities in different lattice directions

The density $\rho(\mathbf{x})$ and momentum density $\rho\mathbf{u}(\mathbf{x})$ at node $\mathbf{x}$ are defined as particle velocity moments of the distribution function, f_i,

$$\rho = \sum_i f_i, \qquad \rho\mathbf{u} = \sum_i f_i e_i, \tag{2.2}$$

where $\sum_i \equiv \sum_{i=1}^{M}$.

If only the physics in the long wave length and low frequency limit are of interest, the lattice spacing $\triangle x$ and the time increment $\triangle t$ can be regarded as small parameters of the same order ε(Knudsen number). Performing a Taylor expansion in time and space, using a Chapman-Enskog expansion technique as done in solving Boltzmann equation[19][40]:

$$\left[\frac{\partial}{\partial t} = \varepsilon\frac{\partial}{\partial t_1} + \varepsilon^2\frac{\partial}{\partial t_2}, \qquad \frac{\partial}{\partial x} = \varepsilon\frac{\partial}{\partial x_1}.\right]$$

and expanding the local equilibrium distribution function f_i^{eq} as

$$f_i = f_i^{eq} + \varepsilon f_i^{neq} = f_i^{eq} + \varepsilon(f_i^{(1)} + \varepsilon f_i^{(2)}) + O(\varepsilon^3). \tag{2.3}$$

with the constraints:

$$\sum_i f_i^{eq} = \rho \qquad \sum_i f_i^{eq}\mathbf{e}_i = \rho\mathbf{u}. \tag{2.4}$$

$$\sum_i f_i^k = 0 \qquad \sum_i f_i^k\mathbf{e}_i = 0. \tag{2.5}$$

for both $k = 1$ and $k = 2$. we obtain the following mass and momentum equations:

$$\frac{\partial\rho}{\partial t} + \nabla\cdot\rho\mathbf{u} = 0, \tag{2.6}$$

$$\frac{\partial\rho\mathbf{u}}{\partial t} + \nabla\cdot\Pi = 0, \tag{2.7}$$

which are accurate to second order in ε for eqn.(2.1). Here the momentum flux tensor Π has the form:

$$\Pi_{\alpha\beta} = \sum_i (\mathbf{e}_i)_\alpha(\mathbf{e}_i)_\beta\left[f_i^{eq} + \left(1 - \frac{1}{2\tau}\right)f_i^{(1)}\right], \tag{2.8}$$

and $(\mathbf{e}_i)_\alpha$ is the component of the velocity vector $\mathbf{e}_i$ in the α-coordinate direction.

To specify the detailed form of $\Pi_{\alpha\beta}$ to get the right Navier-Stokes equations, the lattice structure and the corresponding equilibrium distribution have to be specified. Generally, we assume a polynomial form to $f_{\sigma i}^{eq}(\mathbf{x}, t)$[1]:

$$f_{\sigma i}^{eq}(\mathbf{x}, t) = \rho(\mathbf{x})[A_\sigma + B_\sigma(\mathbf{e}_{\sigma i}\cdot\mathbf{u}) + C_\sigma(\mathbf{e}_{\sigma i}\cdot\mathbf{u})^2 + D_\sigma u^2], \tag{2.9}$$

In two dimensions, we will use the *D2Q9* lattice, and the *D3Q19* lattice for

---

[1] This expression is valid only for small Mach number

three-dimensions. Figure 2.1 shows the lattice structure in two-dimensions.

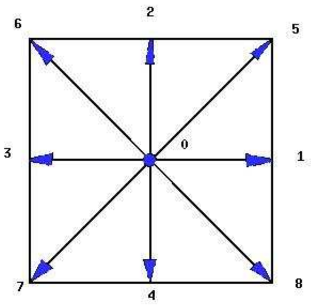

Figure 2.1: d2q9 LBM particle velocities

The lattice velocities in *D2Q9* are defined as

$$\begin{aligned}
\mathbf{e}_{01} &= (0,0), \\
\mathbf{e}_{1i} &= \left(\cos(\tfrac{i-1}{2}\pi), \sin(\tfrac{i-1}{2}\pi)\right), && \text{for } i = 1, \cdots, 4 \\
\mathbf{e}_{2i} &= \sqrt{2}\left(\cos(\tfrac{i-1}{2}\pi + \pi/4), \sin(\tfrac{i-1}{2}\pi + \pi/4)\right), && \text{for } i = 1, \cdots, 4
\end{aligned}$$

while for *D3Q19*[3]:

Table 2.1: List of 19 velocities of D3Q19 LBM

k	σ	i	$\mathbf{e}_{\sigma i}$	$\lvert\mathbf{e}_{\sigma i}\rvert$	k	σ	i	$\mathbf{e}_{\sigma i}$	$\lvert\mathbf{e}_{\sigma i}\rvert$
0	0	1	(0,0,0)	0					
1	1	1	(1,0,0)	1	10	2	4	(1,-1,0)	$\sqrt{2}$
2	1	2	(0,1,0)	1	11	2	5	(0,1,1)	$\sqrt{2}$
3	1	3	(0,0,1)	1	12	2	6	(0,-1,-1)	$\sqrt{2}$
4	1	4	(-1,0,0)	1	13	2	7	(0,1,-1)	$\sqrt{2}$
5	1	5	(0,-1,0)	1	14	2	8	(0,-1,1)	$\sqrt{2}$
6	1	6	(0,0,-1)	1	15	2	9	(1,0,1)	$\sqrt{2}$
7	2	1	(1,1,0)	$\sqrt{2}$	16	2	10	(-1,0,-1)	$\sqrt{2}$
8	2	2	(-1,-1,0)	$\sqrt{2}$	17	2	11	(1,0,-1)	$\sqrt{2}$
9	2	3	(-1,1,0)	$\sqrt{2}$	18	2	12	(-1,0,1)	$\sqrt{2}$

Given the constraints for $f^{eq}_{\sigma i}(\mathbf{x},t)$ in Eqn.(2.4) needed to have the correct stress tensor, the coefficients in $f^{eq}_{\sigma i}(\mathbf{x},t)$ may be determined. For the *D2Q9* lattice structure, we have[25]:

$$\begin{cases} A_0 = \frac{4}{9}, & B_0 = 0, \quad C_0 = 0, \quad D_0 = -\frac{2}{3} \\ A_1 = \frac{1}{9}, & B_1 = \frac{1}{3}, \quad C_1 = \frac{1}{2}, \quad D_1 = -\frac{1}{6}, \\ A_2 = -\frac{1}{36}, & B_2 = \frac{1}{12}, \quad C_2 = \frac{1}{8}, \quad D_2 = -\frac{1}{24}. \end{cases}$$

and for *D3Q19*:

$$\begin{cases} A_0 = \frac{1}{3}, & B_0 = 0, \quad C_0 = 0, \quad D_0 = -\frac{1}{2} \\ A_1 = \frac{1}{18}, & B_1 = \frac{1}{6}, \quad C_1 = \frac{1}{4}, \quad D_1 = -\frac{1}{12}, \\ A_2 = -\frac{1}{36}, & B_2 = \frac{1}{12}, \quad C_2 = \frac{1}{8}, \quad D_2 = -\frac{1}{24}. \end{cases}$$

We can recover the Navier-Stokes equations from the LBGK equation with, in both cases, $C_s^2 = 1/3, P = \rho C_s^2, \nu = (2\tau - 1)/6$. Here, C_s is the speed of sound, P is the pressure on the lattice node, ν is the kinematic viscosity of fluid.

2.3 Lattice Boltzmann model for Particulate systems

The particle-fluid interaction problem has widely varying applications in the fields of chemical, aerospace and environmental engineering as well as in geological and biological sciences. Applications are from geological systems to biological systems like blood flows in vessels, in all scales.

To model particulate suspension and sedimentation in an incompressible fluids, with a complicated geometry with moving boundaries, we have two basic formulations here due to Ladd (1994) [47, 48][64][63], and Aidun et al.(1998)[3][25]. The key is to accurately account for the momentum transfer across the solid-fluid boundary while keeping mass conservation. In the first approach, the fluid occupies the entire computational domain with the solid particles occupied with "interior" fluid, eliminating the solid-fluid interface as far as mass conservation is concerned. This approach gives accurate results as long as the time scale based on the kinematic viscosity of the interior fluid is sufficiently small and the contribution of the inertia of the interior fluid is accounted for when computing the inertia of the particle. This formulation can be used only when the solid density is larger then the fluid density. To extend the formulation to the full range of density ratios between the solid and fluid, the second approach considers the solid particle without the interior fluid and, therefore, applies to any density ratio. This LBE based simulations of suspended particles gives results in good agreement with the finite element solutions of the Navier-Stokes equations for low to moderate particle Reynolds number[73][75][76][74] [66]. It is also shown that this method, when applied with care, can produce very accurate particle trajectories over very long time periods, making it possible to investigate the dynamics and stability of particle motion, even near bifurcation. By analysis of the appropriate phase-space trajectories near transition points, the LBE based method has been useful in revealing the type of bifurcation and the scaling laws governing the particle motion.

The basic idea in both approaches is the same: treat particle motions in fluid as a moving boundary problem. For particle dynamics, compute forces and torques on the particles and then use Newtonian dynamics to find the trajectories of particles. Here we reformulate the LBM using an operator presentation to simplify the expression of this method. And for particulate suspension and sedimentation, we mainly use the bulk model by Aidun et al.[3][25] without fluid in the solid particle region.

For the collision procedure, we can write the post-collision distribution function at $(\mathbf{x}, t)$ as:

$$f_{\sigma i}(\mathbf{x}, t_+) = \mathbf{C} f_{\sigma i}(\mathbf{x}, t) = f_{\sigma i}(\mathbf{x}, t) - \frac{1}{\tau}\left[f_{\sigma i}(\mathbf{x}, t) - f_{\sigma i}^{eq}(\mathbf{x}, t)\right], \tag{2.10}$$

where $\delta x = 1$ and $\delta t = 1$ corresponding to the former formulation, and t_+ is the time immediately after the collision,or $t - t_+ \ll 1$. The operator $\mathbf{C}$ is called the "collision" operator. We denote the propagation step as:

$$f_{\sigma i}(\mathbf{x}, t_+) = \mathbf{P}_0 f_{\sigma i}(\mathbf{x}, t_+) = f_{\sigma i}\left(\mathbf{x} + \mathbf{e}_{\sigma i'}, t_+\right). \tag{2.11}$$

where as before, $\sigma i'$ is always the link with direction opposite to that of link σi,that is,$\mathbf{e}_{\sigma i'} = -\mathbf{e}_{\sigma i}$, and $\mathbf{P}_0$ is the propagation operator. we could rewrite the Eqn.(2.1) as:

$$f_{\sigma i}(\mathbf{x}, t+1) = \mathbf{P}_0 \mathbf{C} f_{\sigma i}(\mathbf{x}, t). \tag{2.12}$$

and the equilibrium distribution function takes the form:

$$f_{\sigma i}^{eq}(\mathbf{x}, t) = \rho(\mathbf{x})\left[A_\sigma + B_\sigma(\mathbf{e}_{\sigma i} \cdot \mathbf{u}) + C_\sigma(\mathbf{e}_{\sigma i} \cdot \mathbf{u})^2 + D_\sigma u^2\right]. \tag{2.13}$$

with the same constraints on different moments of $f_{\sigma i}^{eq}$:

$$\sum_\sigma \sum_i f_{\sigma i}^{eq} = \rho, \tag{2.14}$$

$$\sum_\sigma \sum_i f_{\sigma i}^{eq} \mathbf{e}_{\sigma i} = \rho \mathbf{u}, \tag{2.15}$$

$$\sum_\sigma \sum_i f_{\sigma i}^{eq} \mathbf{e}_{\sigma i} \mathbf{e}_{\sigma i} = \rho C_s^2 \mathbf{I} + \rho \mathbf{u}\mathbf{u}. \tag{2.16}$$

Here the C_s is the speed of sound and $\mathbf{I}$ donates the unit tensor. Then we get the same equilibrium distribution function as before, for two-dimensional and three-dimensional systems, respectively.

Now let us direct attention to the more difficult topic of boundary interaction between fluid and a moving solid particle. Obviously, this is harder than to deal with the boundary between fluid and a stationary wall, for the solid particle can move by translation and also rotation. The boundary condition imposed at the solid-fluid interface is the no-slip condition, that is, the fluid adjacent to the solid surface moves at the same velocity as the solid surface. Here, following Aidun et al. we introduce the same technique for the moving boundaries, but without fluid filled in the particle volume. So far, the nodes inside the solid boundary are solid nodes, containing no fluid, and consequently the transfer of momentum is only between the solid boundary and the adjacent fluid.

The calculation of the boundary node distribution function in the LBM consists of three operations:

1. collision at the lattice node $\mathbf{x}$:

$$f_{\sigma i}(\mathbf{x}, t_+) = \mathbf{C} f_{\sigma i}(\mathbf{x}, t) \tag{2.17}$$

2. no-slip rule at the fluid-particle boundary with zero velocity:

$$\widetilde{f}_{\sigma i}(\mathbf{x}, t+1) = \mathbf{P}_{n-s}(0) f_{\sigma i}(\mathbf{x}, t_+) = \begin{cases} f_{\sigma i'}(\mathbf{x}, t_+), & \text{if}(\sigma i') \in \text{BL}, \\ f_{\sigma i'}(\mathbf{x} + \mathbf{e}_{\sigma i'}, t_+), & \text{otherwise.} \end{cases} \tag{2.18}$$

3. modification of the boundary nodes' distribution function components to maintain the no-slip condition at the fluid-particle boundary:

$$f_{\sigma i}(\mathbf{x}, t{+}1) = \mathbf{P}_{n-s}(\mathbf{u}_b) f_{\sigma i}(\mathbf{x}, t_+) = \begin{cases} \widetilde{f}_{\sigma i'}(\mathbf{x}, t_+) + 2\rho B_\sigma \mathbf{u}_b \cdot \mathbf{e}_{\sigma i}, & \text{if}(\sigma i') \in \text{BL}, \\ \widetilde{f}_{\sigma i'}(\mathbf{x} + \mathbf{e}_{\sigma i'}, t_+), & \text{otherwise.} \end{cases} \tag{2.19}$$

where $\mathbf{P}_{n-s}(\mathbf{u}_b)$ is propagation operator at a moving boundary with a velocity of $\mathbf{u}_b$), when $\mathbf{u}_b) = 0$, then it realize a no-slip condition for a stationary boundary. $\mathbf{u}_b$ is the velocity of the moving boundary, B_σ is from the equilibrium distribution function of the model. And it is applied with the following algorithm. First, $\mathbf{u}_b$ is obtained from the position vector of the center of mass, $\mathbf{X}(t)$, the translational velocity, $\mathbf{U}(t)$, and the angular velocity, $\boldsymbol{\Omega}(t)$, of the solid particle, that is:

$$\mathbf{u}_b = \mathbf{U}(t) + \boldsymbol{\Omega}(t) \times [\mathbf{x} + \tfrac{1}{2}\mathbf{e}_{\sigma i'} - \mathbf{X}(t)]. \tag{2.20}$$

Secondly, the density at node $\mathbf{x}$ in this case could change:

$$\rho(\mathbf{x}, t+1) = \frac{\widetilde{\rho}(\mathbf{x}, t+1)}{1 - 2\sum_{(\sigma i') \in BL} B_\sigma \mathbf{u}_b \cdot \mathbf{e}_{\sigma i}} \tag{2.21}$$

Simply, we can express the above algorithm as:

$$f_{\sigma i}(\mathbf{x}, t+1) = \mathbf{P}_{n-s}(\mathbf{u}_b)\mathbf{C} f_{\sigma i}(\mathbf{x}, t_+) \tag{2.22}$$

So the impulse force exerted on the particle for any boundary link, or said in another way, the inverse force produced by the momentum increment at the fluid-particle boundary, is given by:

$$\mathbf{F}^{(b)}_{\sigma i}(\mathbf{x} + \tfrac{1}{2}\mathbf{e}_{\sigma i'}, t + \tfrac{1}{2}) = 2\mathbf{e}_{\sigma i'}[f_{\sigma i}(\mathbf{x}, t+1) + \rho(\mathbf{x}, t+1) B_\sigma \mathbf{u}_b \cdot \mathbf{e}_{\sigma i'}], \qquad \text{if } (\sigma i^{'}) \in \text{BL}, \tag{2.23}$$

and the torque, $\mathbf{T}^{(b)}_{\sigma i}$, with respect to the center of mass $\mathbf{X}$, is given by:

$$\mathbf{T}^{(b)}_{\sigma i}(\mathbf{x} + \tfrac{1}{2}\mathbf{e}_{\sigma i'}, t + \tfrac{1}{2}) = [\mathbf{x} + \tfrac{1}{2}\mathbf{e}_{\sigma i'} - \mathbf{X}(t)] \times \mathbf{F}^{(b)}_{\sigma i}(\mathbf{x} + \tfrac{1}{2}\mathbf{e}_{\sigma i'}, t + \tfrac{1}{2}). \tag{2.24}$$

Now we move to dynamics of particles in fluids. As mentioned above, we calculate the forces and torque on the particle by fluid, add any external forces and torques applied to the particles, and then use Newtonian dynamics to capture their trajectories. When the particle moves, it will cover and uncover some fluid nodes. If a particle covers some fluid nodes it will assume the momentum of the fluid nodes, and then an impulse force is applied to the solid particle over a unit time interval from $t_0 - 1$ to t_0, which is given by:

$$\mathbf{F}^{(c)}(\mathbf{x}, t_0 + \tfrac{1}{2}) = \textstyle\sum_{\sigma i} f_{\sigma i}(\mathbf{x}, t_0)\mathbf{e}_{\sigma i}, = \rho(\mathbf{x}, t_0)\mathbf{u}(\mathbf{x}, t_0), \tag{2.25}$$

and the torque on the solid particle is given by:

$$\mathbf{T}^{(c)}(\mathbf{x}, t_0 + \tfrac{1}{2}) = [\mathbf{x} - \mathbf{X}(t_0)] \times \mathbf{F}^{(c)}(\mathbf{x}, t_0 + \tfrac{1}{2}) \tag{2.26}$$

If a particle uncovers some fluid nodes while moving, we need to give values to the macroscopic quantities such as velocities and density on these new generated nodes, as well as the distribution function on these nodes. In this case, we first obtain the fluid density at the new node through the average fluid density of its neighboring nodes:

$$\rho(\mathbf{x}, t_0) = \frac{1}{N_b} \sum_{N_b} \rho(\mathbf{x} + \mathbf{e}_{\sigma i'}, t_0) \tag{2.27}$$

and the velocity of the new fluid node is equal to the solid boundary node at the time when it is uncovered, that is,

$$\mathbf{u}(\mathbf{x}, t_0) = \mathbf{U}(t_0) + \mathbf{\Omega}(\mathbf{t_0}) \times [\mathbf{x} - \mathbf{X}(t_0)]. \tag{2.28}$$

and with this velocity and density, we assign the equilibrium distribution to the new fluid nodes as their new distribution. In this procedure, the solid particle will lose momentum to the new generated nodes, and hence the force and torque will be given, respectively, by

$$\begin{aligned}\mathbf{F}^{(u)}(\mathbf{x}, t_0 + \tfrac{1}{2}) &= -\rho(\mathbf{x}, t_0)\mathbf{u}(\mathbf{x}, t_0), && (2.29)\\ \mathbf{T}^{(u)}(\mathbf{x}, t_0 + \tfrac{1}{2}) &= [\mathbf{x} - \mathbf{X}(t_0)] \times \mathbf{F}^{(u)}(\mathbf{x}, t_0 + \tfrac{1}{2}), && (2.30)\end{aligned}$$

The total hydrodynamic force and torque on the solid particle arises from three parts: fluid-particle boundary, particle coverage of fluid nodes, and particle uncoverage of fluid nodes. We have

$$\mathbf{F}(t_0 + \tfrac{1}{2}) = \sum_{FBN} \sum_{\sigma i} \mathbf{F}^{(b)}_{\sigma i}(\mathbf{x} + \tfrac{1}{2}\mathbf{e}_{\sigma i'}, t_0 + \tfrac{1}{2}) + \sum_{CN} \mathbf{F}^{(c)}(\mathbf{x}, t_0 + \tfrac{1}{2}) + \sum_{UN} \mathbf{F}^{(u)}(\mathbf{x}, t_0 + \tfrac{1}{2}), \tag{2.31}$$

$$\mathbf{T}(t_0 + \tfrac{1}{2}) = \sum_{FBN} \sum_{\sigma i} \mathbf{T}^{(b)}_{\sigma i}(\mathbf{x} + \tfrac{1}{2}\mathbf{e}_{\sigma i'}, t_0 + \tfrac{1}{2}) + \sum_{CN} \mathbf{T}^{(c)}(\mathbf{x}, t_0 + \tfrac{1}{2}) + \sum_{UN} \mathbf{T}^{(u)}(\mathbf{x}, t_0 + \tfrac{1}{2}), \tag{2.32}$$

where FBN stands for the fluid-particle boundary nodes, CN for the covered fluid nodes, and UN for uncovered fluid nodes. The total force and torque at time t_0 are averaged over those at time $t_0 - 1/2$ and $t_0 + 1/2$:

$$\begin{aligned}\mathbf{F}(t_0) &= [\mathbf{F}(t_0 - \tfrac{1}{2}) + \mathbf{F}(t_0 + \tfrac{1}{2})]/2, && (2.33)\\ \mathbf{F}(t_0) &= [\mathbf{T}(t_0 - \tfrac{1}{2}) + \mathbf{T}(t_0 + \tfrac{1}{2})]/2, && (2.34)\end{aligned}$$

With the net force and torque from the above equations, plus the external force contribution, the motion of the solid particle from t_0 to $t_0 + 1$ is determined by solving Newton's equations:

$$\begin{aligned}M\frac{d\mathbf{U}(t)}{dt} &= \mathbf{F}(t_0), && (2.35)\\ \mathbf{I} \cdot \frac{d\mathbf{\Omega}(t)}{dt} &+ \mathbf{\Omega} \times [\mathbf{I} \cdot \mathbf{\Omega}] = \mathbf{F}(t_0) && (2.36)\end{aligned}$$

where M is the mass of particle, $\mathbf{I}$ is the inertial tensor, and $\boldsymbol{\Omega}$ is the angular velocity.

As a further refinement of Ladd's method, Qi(1999)[73] also uses a shell model for the solid particles with fluid in the interior nodes, but uses a technique very similar to that of Aidun et al. which can remove the limitation on the density ratio between solid particles and fluids. All of these methods use the same collision and propagation rules proposed by Ladd(1994a), but Ladd's original method only considers the forces from the interaction between fluid and particles, while in Qi's method the forces originate from the coverage and uncoverage of fluid nodes by moving particles. These parts are essentially the same as those suggested in Aidun et al.(1998), the difference being that the fluid in the particle region can evolve according to the corresponding collision and propagation rules, so we do not need to generate new values on the uncovered new nodes since of these nodes are fluid nodes in this method.

There are good reason to allow fluid to enter the solid region as Ladd did. First, the total mass of fluid in the simulation domain is strictly conserved at each time step. This restriction guarantees recovery of the Navier-Stokes equations from the LBM. Second, in this shell method, with fluid in solid region, we can ensure that the Navier-Stokes equations are obeyed in the fluid region.

2.4 Boundary conditions and forcing in lattice Boltzmann method

2.4.1 Boundary conditions

The boundary conditions are an important ingredient in any numerical computation of phenomena governed by partial differential equations. There are various types of boundary conditions[20] that one may impose on a flow domain. Typically, one may have solid walls (moving with a specific velocity or at rest), flow inlet and outlet conditions, or free slip conditions on rigid surfaces. Here in our cases, we mainly treat no-slip boundary conditions on stationary surfaces. As mentioned, in LBM for a no-slip stationary boundary, we mainly use the bounce-back rule which assumes that the boundary is located at the mid-point between fluid nodes and boundary nodes. This bounce-back no-slip boundary condition is easy and convenient to apply in the LBM, which is a major advantage over other methods when dealing with flow problems with complicated geometry. The two-dimensional case of Fig.(2.2) illustrates how the bounce-back rule is implemented: the virtual fluid particle with its distribution just bounces back along its incoming directions.

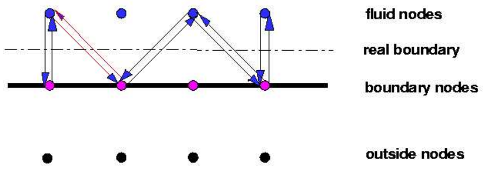

Figure 2.2: Bounce-Back boundary condition rules

Other kinds of boundary conditions such as velocity boundary and/or pressure boundary at the inlet and outlet of flow domain may be needed [54][57][95]. As for the velocity boundary condition, we use the momentum conservation equation in eqn.(2.14) to give the unknown distribution in some directions while evolving. For a pressure boundary, the same methods is used, except that we should take account of the relation between pressure and density $p = \rho C_s^2$ in the lattice Boltzmann model. Alternatively, some workers introduce non-equilibrium extrapolation techniques for both kinds of boundary conditions. One last point to note is that Ladd's method for dealing with velocity boundary conditions is another alternative choice.

2.4.2 Forcing the flow

External forces, such as gravity, may be represented by adding a fixed amount of momentum at each node. The general idea is add a specific amount to the distribution function in evolution, and this will increase the momentum, but not increase the mass of the fluid nodes, for the added part will produce a net zero mass increment when summing them up in all directions. For a force **f**, the modified equation is[13][77]:

$$f_{\sigma i}(\mathbf{x}+\mathbf{e}_{\sigma i}, t+1) = f_{\sigma i}(\mathbf{x}, t) - \frac{1}{\tau}\left[f_{\sigma i}(\mathbf{x}, t) - f_{\sigma i}^{eq}(\mathbf{x}, t)\right] + \frac{\tau D}{b_m e_{\sigma i}^2}\mathbf{f}\cdot\mathbf{e}_{\sigma i}. \tag{2.37}$$

Then, for instance, taking $\mathbf{f} = -g\mathbf{E}_z$, with g the gravity acceleration, we could obtain the usual Navier-Stokes equations in a gravity field if follow the same procedure described above. An applied pressure gradient may also be represented by a constant forcing. Indeed, adding a constant force in x-direction is equivalent to changing the pressure difference in this direction by some amount, and this is done in our simulations with a pressure gradient.

2.5 Validation of lattice Boltzmann calculations

In this section, we discuss the simulation of certain flow and particle sedimentation and shear suspension processes, as a validation of our serial and parallel 2D/3D lattice Boltzmann codes. This will be the basis for the subsequent research for non-trivial flow and particle suspension problems by this method.

2.5.1 Test problems and validation for pure fluid flow

As a validation of our numerical codes, we use the simplest two-dimensional shear and Poiseuille flows between two flat plates. Here we compare results with analytic solutions.

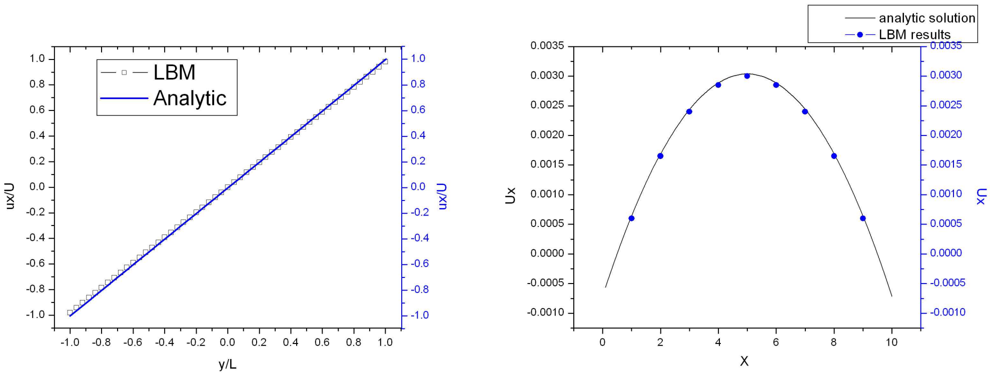

Figure 2.3: 2-D shear and Poiseuille flows between two flat plates

For shear flow, we use the moving boundary condition scheme proposed by Ladd[47][48] to deal with moving boundary in fluid. In fig.(2.3a), we notice that both the numerical results and analytic results match very well except at the nodes close to the boundary. The small discrepancy arises because in this scheme, we actually assume that the boundary is located half way between a computational boundary node and its neighboring fluid node[6][40][54]. However, this kind of bounce-back boundary condition is very convenient in a complicated geometry, and we will use it in particulate flow in fractures.

In fig.(2.3b), the numerical results match the analytic results very well. Also we see that since the real boundary is located at the mid-point between the actual solid boundary (set at 0 and 10 in our computations) and its neighboring fluid node, the fluid velocity goes to 0 at 0.5 and 9.5 respectively. This "problem" could be ameliorated by introducing other schemes (such as non-equilibrium extrapolation techniques) to deal with boundary conditions.

2.5.2 Single particle motion in a linear shear flow

To validate the particle component of the numerical code we consider the motion of a single particle in shear flow, a problem with an extensive history and a number of previous results on rotation speed and migration dynamics for comparison.

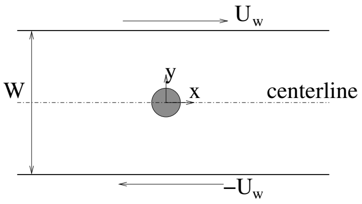

Figure 2.4: A particle rotating in the zero-velocity plane in simple shear flow.

At vanishing Reynolds number, the angular velocity of a freely rotating circular cylinder in a linear shear flow is readily calculated to be $\omega = \dot{\gamma}/2$. As the particle Reynolds number increases, a variety of numerical and approximate analytical calculations [46, 24, 59] and experiments [94] find that the normalized angular velocity $\Omega_p = \omega/\dot{\gamma}$ systematically decreases from 1/2, as shown in Fig. 2.5. This trend holds for both open and confined shear flows, although the precise numerical value is sensitive to boundary confinement. We have evaluated the angular velocity of a cylinder lying on the centerline of a channel for two values of channel width relative to cylinder radius, $W/a = 4$ and 8. The simulation box in the two dimensional calculations ranges in size from $40a \rightarrow 80a) \times (4a \rightarrow 8a)$, and in three dimensions the dimensions are $20a \times 12a \times 8a$. As seen in Fig. 2.5, the results are generally quite compatible with earlier calculations, and in particular are in good agreement with those of Ding and Aidun[24] who used the lattice Boltzmann method at somewhat higher resolution.

The distinction between a cylinder and a sphere in this flow appears more clearly in the streamline patterns shown in Fig. 2.6. (In the case of a sphere, the streamlines are those in a plane through the sphere's center, perpendicular to the vorticity

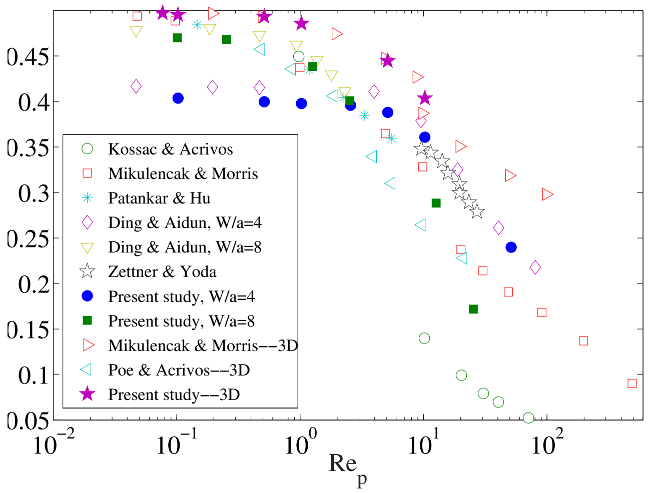

Figure 2.5: Comparison of simulation results for the angular velocity of a circular cylinder and a sphere in shear flow with previous experimental (Zettner and Yoda) and numerical results.

axis.) In general there are three types of streamlines present: closed recirculating streamlines around the cylinder or sphere, streamlines close to the wall which traverse the whole domain, and reversing streamlines which approach the particle and then reverse direction. In the subsequent discussion of two-particle systems, these distinct regions will play a critical role in trajectory bifurcation. The variation of streamline pattern with Re_p is rather weak over the range of values considered here.

The detailed geometry of these three flow regions are of course controlled by many factors including the Reynolds number and the size ratio. The perturbation to linear shear due to the presence of the cylinder or sphere decays away in the upstream and downstream directions, and we find that after a distance of 3 or 4 particle diameters in either direction, the velocity field nearly reverts to a linear profile. In practice, in the two-particle calculations below, we use a somewhat larger distance, $6d$, to separate the initial positions along the longitudinal direction to study interactions. As shown in Fig. 2.7, at this distance the perturbation in the linear velocity profile due to the presence of the particle has decayed to the 10^{-4} level

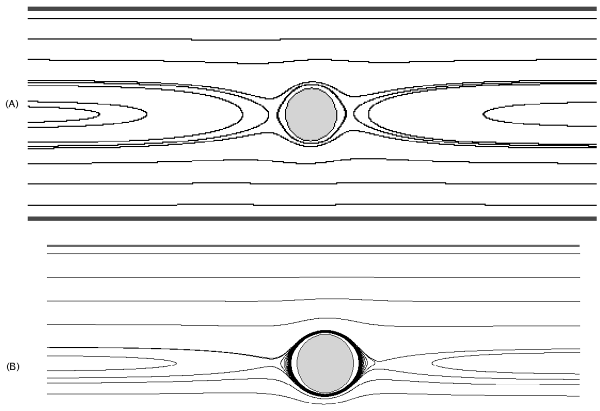

Figure 2.6: Streamlines for a freely rotating particle in linear shear flow. (A) circular cylinder at $Re_p = 1.5$; (B) sphere, in the plane through the sphere's center perpendicular to the vorticity axis at $Re_p = 1.0$).

(the small asymmetry in the difference is due to particle meshing on the lattice).

2.5.3 Particle sedimentation between two flat plates

As a second test of the lattice Boltzmann code, we have simulated lateral particle migration in shear flow at $Re_p = 0.625$, the same value used by Feng *et al*[31] in a finite element calculation. A neutrally buoyant particle is initially placed off the channel axis at $y = W/4$ or $y = 3W/4$, and allowed to move to its equilibrium position at the center of the channel. For a particle of diameter $d = 20$, the trajectories are shown in Fig. 2.8 and compared to the finite element results of [31]. The agreement is excellent.

In this test, a relatively coarse grid of 20 lattice spacings for the diameter of particles was sufficient, although in the new results presented below a finer resolution is used. The initial velocity of the cylinder was chosen as the linear shear velocity at the cylinder center, and the initial angular velocity was zero. However, we observe

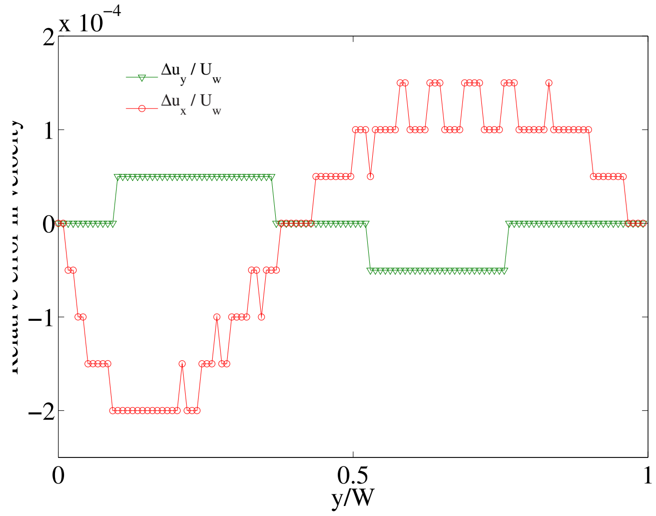

Figure 2.7: Deviation of the velocity from linear shear at a distance $6d$ from the particle center. Red and green points are $\Delta u_x/U_w$ and $\Delta u_y/U_w$, respectively.

very little difference in the trajectories if other initial velocity choices (corresponding to an initial velocity slip) are used. The same insensitivity to initial conditions is also found in the two-particle interaction calculations below, and some further discussion of this issue is given in the Appendix.

2.6 Conclusion

In this chapter, we discussed the lattice Boltzmann method for fluid flow and particle transport, particularly for flow and suspension problems with a complicated geometry. More generally, extensive validation tests have been performed in the course of the research to check our lattice Boltzmann codes in both serial and parallel computing environments.

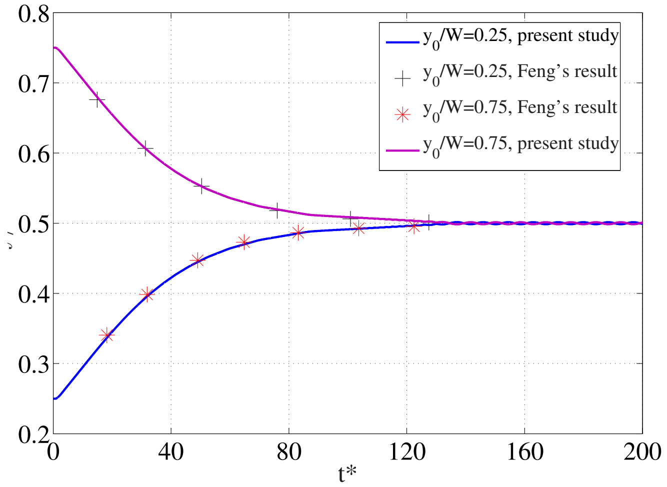

Figure 2.8: Migration of a cylinder to the centerline of the channel for two initial positions; present results (curves) compared to Feng *et al.* [31] (points).

Chapter 3

Power-law fluid flow in fracture channels

The two-dimensional pressure driven flow of non-Newtonian power-law fluids in self-affine fracture channels at finite Reynolds number is calculated. The channels have constant mean aperture and two values ζ=0.5 and 0.8 of the Hurst exponent are considered. The calculation is based on the lattice-Boltzmann method, using a novel method to obtain a power-law variation in viscosity, and the behavior of shear-thinning, Newtonian and shear-thickening liquids is compared. Local aspects of the flow fields, such as maximum velocity and pressure fluctuations, were studied, and the non-Newtonian fluids were compared to the (previously-studied) Newtonian case. The permeability results may be collapsed into a master curve of friction factor vs. Reynolds number using a scaling similar to that employed for porous media flow, and exhibits a transition from a linear regime to a more rapid variation at Re increases.

3.1 Surface morphology and self-affinity

3.1.1 Self-affine roughness

In this subsection we review the characterization of self-affine fractures and their numerical implementation. We consider a fracture surface without overhangs, *i.e.*, the surface height $h(x, y)$ is a single-valued function of the two coordinates $\mathbf{r} = (x, y)$ lying in the mean plane of the surface. A *self-affine* fractal surface is one which displays different scaling along the different spatial directions[29], a statistical self-similarity under the transformation

$$x \to \lambda x \text{ and } y \to \lambda y \Rightarrow h(\mathbf{r}) \to \lambda^{\zeta} h(\mathbf{r}) \tag{3.1}$$

where ζ is the Hurst or roughness exponent. Observations of a variety of naturally fractured rock surfaces in different fracture modes yield just two common values of ζ, approximately 0.5 and 0.8. We further assume that the surface has spatial isotropy in its mean plane. The surface is further characterized by the amplitude of the roughness, or equivalently the prefactor C_0 in the height-height correlation function,

$$\langle [h(\mathbf{r} + \mathbf{\Delta}) - h(\mathbf{r})]^2 \rangle = C_0 (|\mathbf{\Delta}|/\ell)^{2\zeta} \tag{3.2}$$

where the intrinsic length scale ℓ might be the grain size in experiment or the lattice spacing in a calculation. In practice we generate self-affine surfaces using the Fourier synthesis method [89] as in [26].

A self-affine fracture channel is made of two complementary self-affine surfaces separated by a gap, and in some cases the surfaces are shifted relative to each other parallel to the mean plane. The statistical properties of the fracture are specified by the Hurst exponent, the mean aperture between two surfaces, the shift distance, if any, and by the amplitude of the roughness. The height fluctuations of a single self-affine surface increase with its lateral extent L, so that the difference between the maximum and minimum heights scales as $(L/\ell)^{\zeta}$, and we consider the limit $H \ll R < L$, as shown for a typical fracture in Fig. 3.1, and we will use this self-affine fracture channel realization for microscopic local flow analysis in the first part for non-Newtonian fluid flow along the fracture channel, for averaged and statistical properties, we will use more numerical realizations by the method in the next subsection.

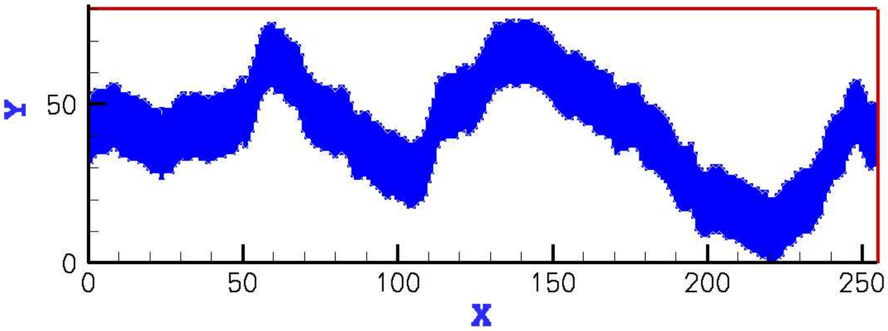

Figure 3.1: Geometry of a typical self-affine fracture composed of two complementary self-affine surfaces with ζ=0.8.

Note that the effective flow diameter of the fracture varies along its length and can be much smaller than the mean aperture, due to the tortuosity of the channel. When a lateral shift is present, the aperture varies locally as well, and furthermore if H is too small the sides of the fracture may overlap.

3.1.2 Numerical methods to generate self-affine surfaces

Our aim is to study various aspects of flow regimes and particulate suspensions in fractures which are sensitive to the fracture roughness. The method used for generation of fracture surface to describe irregularities and correlations consist of digital filtering of arrays of independent random numbers[90]. Power law filtering introduces correlations over a wide range of scales. Changing the power law will change the spatial correlation, that is, fractal dimension actually. Here we use the same techniques. The first ingredient is the height function $z(x, y)$, the surface is generated by a Fourier synthesis method, based on power-law filtering of arrays of independent random numbers. The random numbers are generated using a Gaussian distribution, and then modulated by an appropriate power law. If $\widetilde{Z}(k)$ is the Fourier transform of the initial Gaussian random array, then the Fourier transform of the surface elevation is chosen to be

$$Z(k) = k^{-\zeta-\phi}\widetilde{Z}(k). \tag{3.3}$$

here $\phi = 1/2$ is appropriate for the self-affine *curve*, and $\phi = 1$ appropriate for real rock surface. In our realization of this procedure, with this power law, we keep the statistically self-affine surface with periodic boundary conditions. This periodicity is not a physically essential ingredient here, but has some computing advantages in alleviating finite size effects. For example, to generate a real rock two-dimensional surface, initially, we generate a $L \times L$ matrix of independent random numbers with Gaussian distribution. Then the Fourier transform of this initial matrix is modulated by a power law with high wave-numbers filter that introduces height-to-height correlations. Finally, the whole surface is rescaled in order to get the desired characteristic length ℓ. This numerical method generates homogeneous and isotropic surfaces, and is preferable instead of other numerical methods such as the random addition algorithm. The following are some illustrations of the self-affine curve and surface generated by this method.

In our simulation, we shall model fractures as the gap between a self-affine surface or curve and its replica, which is translated by a fixed distance h in the direction normal to the mean plane of the surface or curve[28]. Furthermore, during the fracturing process, the opposite matching surfaces or curves might experience a

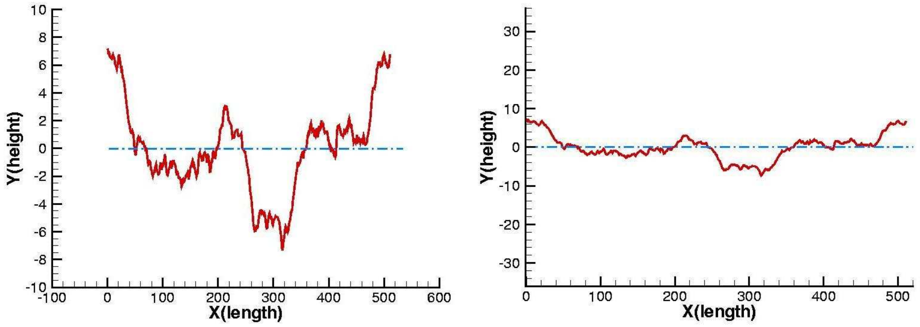

Figure 3.2: self-affine curve with Hurst exponent $\zeta = 0.8$ and $\sigma = 6.0$

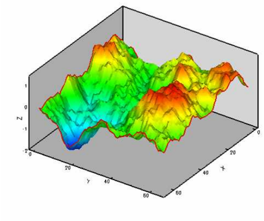

Figure 3.3: self-affine surface with Hurst exponent $\zeta = 0.8$ and $\sigma = 1.0$ by normalization

lateral shift, in addition to the vertical displacement over the mean plane.

3.2 The lattice-Boltzmann method for non-Newtonian fluid

In addition to the introduction of lattice Boltzmann method in the previous chapter, the basic idea in extending the lattice Boltzmann method to power-law fluids was presented by Aharonov and Rothman [78], and consists of adjusting the relaxation time τ *locally* so as to achieve the desired ratio of stress to strain rate. Here we consider power-law fluids using a generalized Newtonian model, as in [34], where the relation between the stress tensor $\sigma_{\alpha\beta}$ and the strain rate tensor $D_{\alpha\beta} = 1/2((\partial_\beta u_\alpha + \partial_\alpha u_\beta)$ is similar to that for Newtonian fluids, $\sigma_{\alpha\beta} = 2\mu D_{\alpha\beta}$, but the local viscosity μ is a function of the invariants of the strain rate tensor. We consider power-law fluids, $\mu = m\dot{\gamma}^{n-1}$, where the case $0 < n < 1$ corresponds to shear-thinning, $n > 1$ corresponds to shear-thickening, and $n = 1$ recovers linear Newtonian fluids, where the local shear rate $\dot{\gamma}$ is related to the second invariant of D_{ij} via $\dot{\gamma} = (2\mathbf{D} : \mathbf{D})^{1/2}$. The procedure in [34] was to obtain the strain rate tensor by numerical differentiation of the previously calculated velocity field, then determine the appropriate local viscosity and thence the local relaxation time. Here we adopt a different procedure: in the lattice Boltzmann method the strain rate tensor is directly related to the velocity distribution function by [19]

$$D_{\alpha\beta} = -\frac{3}{2\rho\tau} \sum_i (f_i - f_i^{eq}) \mathbf{e}_{i\alpha} \mathbf{e}_{i\beta}; \tag{3.4}$$

which should in turn equal $\sigma_{\alpha\beta}/2\mu$, there is a constraint on the f_i which is solved by iteration. From this strain rate tensor, we could get the stress tensor as,

$$\boldsymbol{\sigma} = -\rho c_s^2 \mathbf{I} - (1 - \frac{1}{2\tau}) \sum_i (f_i - f_i^{eq}) \mathbf{e}_i \mathbf{e}_i. \tag{3.5}$$

To validate the formulation of power-law fluids given above, we calculate the velocity profile for pressure-driven flow in a smooth-walled channel of constant aperture (a Hele-Shaw cell), which may be compared to an analytic solution of the Navier-Stokes equation. Applying a pressure gradient $\Delta P/L = -G$ in the x-direction, the velocity for a power-law fluid with rheological parameters $m, n > 0$ as above in a channel of width H is

$$u_x(y) = \frac{n}{n+1} \left(\frac{G}{m}\right)^{1/n} \left(\left|\frac{H}{2}\right|^{(n+1)/n} - \left|\frac{H}{2} - y\right|^{(n+1)/n} \right), \tag{3.6}$$

We also record the mean velocity $\overline{u}$ and the fluid flux Q (per unit length in the passive third direction), which will be useful below:

$$Q = H\overline{u} = \int_0^H dy\, u_x(y) = \frac{n}{2n+1}\left(\frac{H^2}{2}\right)\left(\frac{GH}{2m}\right)^{1/n} \tag{3.7}$$

In the simulation, we begin with zero velocity and integrate the lattice Boltzmann equation in the previous chapter to steady state, using the convergence criterion

$$\epsilon = \sum_x \frac{\|u(\mathbf{x},t) - u(\mathbf{x},t-1)\|}{\|u(\mathbf{x},t)\|} < 1.0 \times 10^{-6}, \tag{3.8}$$

For power-law indices n=0.75, 1.0 and 1.25, m=0.01, and pressure gradient $G = 1 \times 10^{-6}$ we obtain the profiles shown in Fig. 3.4, which agree with theory. In practice, as with any numerical method, computational instabilities may occur for substantially different values of the pressure gradient and fluid index, but the algorithm could be extended there using techniques such as multi-time step relaxation for the local shear viscosity [87].

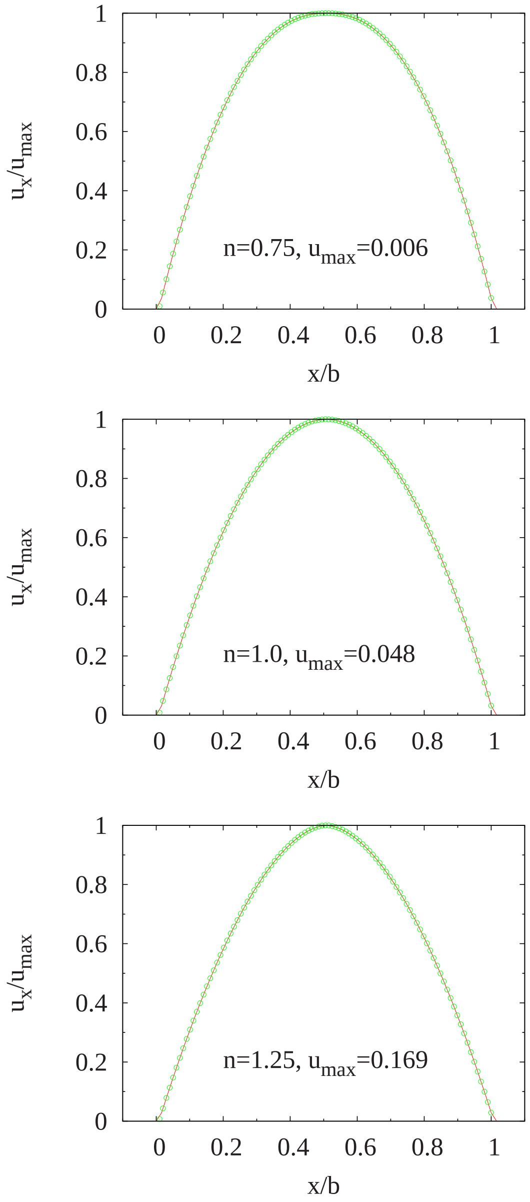

Figure 3.4: Velocity profiles of power-law fluids with $m = 0.01, n = 0.75, 1.0, 1.25$ in a Hele-Shaw cell with pressure gradient $G = 1 \times 10^{-6}$. The points are simulation results while the solid lines are the analytical solution in eq.(3.6). The maximum velocities for the three fluids are $u_{max} = 0.006, 0.048, 0.169$, respectively.

3.3 Local analysis of the flow field

We wish to examine how the local flow behavior varies with the rheology of the fluid, at different geometrical features of a self-affine channel. We focus on a single realization of the fracture, shown in Fig. 3.1, and vary the power law index n and the pressure gradient G. The complete simulation box has length $L = 256$ in the flow direction and width $W = 80$, in terms of the (unit) lattice spacing, and the (constant) vertical aperture is $H = 20$. A uniform pressure gradient is applied everywhere along the channel, and periodic boundary conditions are applied in the flow direction. The uniform gradient is imposed by a gravity-like constant body force applied as in Section 2.4.2, but because of the tortuosity of the flow channel the actual pressure will fluctuate about the nominal value as discussed below. Local minima in the effective width (normal to the average flow) occur around x=55, 110, and 240 where mass conservation implies the velocity magnitude will be a maximum, irrespective of the rheology of the fluid. In Fig. 3.5, we show velocity fields and streamlines for the three fluids along a segment of the fracture channel $20 \lesssim x \lesssim 100$ in Fig. 3.1 which includes a constriction, for applied pressure gradient $G = 1 \times 10^{-6}$. As we see, the streamlines are tortuous and very roughly follow the channel walls, although recirculating eddies (closed vortices) *may* occur where the channel exhibits side branches or dead-end regions. Indeed, at the present flow rate an eddy appears in the shear-thickening case but not the others, presumably because the velocities are higher in that case.

3.3.1 Velocity field

First we examine the variation of maximum absolute velocity along the channel, in order to show how the fluid rheology influences the earlier results of Skjetne *et al.* [38] for the Newtonian case. More precisely, for each x along the channel we compute the maximum over y of $|\mathbf{u}(x, y)|$, although we would have reached the same qualitative conclusions had we considered the maximum over y of $u_x(x, y)$. Calculations were performed for three values of the pressure gradient, $G = 1 \times 10^{-6}$, 5×10^{-5} and 2×10^{-4}, which correspond to Reynolds numbers $Re = 0.95$, 37.0 and 92.7, respectively, for the Newtonian fluid. Since the viscosity varies within the channel for the shear thinning and thickening fluids, there is no unique definition of Re in those cases, although a convenient choice will be introduced in Section 3.4 for scaling purposes.

The resulting plots of maximum velocity are shown in Fig. 3.6, where each velocity is normalized by the average streamwise flow velocity $\overline{u_x}$ (referred to as the interstitial velocity u^* in [38]), which equals the flux divided by the channel width. Obvious peaks appear at the positions of the visible constrictions in the channel near $x = 55$, 110 and 240, reflecting the narrowed aperture there. The normalized peak heights are fairly insensitive to the Reynolds number, although away from the peaks the trend is for maximum velocity to increase with Re. Note that for a flat channel, the normalized maximum absolute velocity would equal 1.5, so the values of 5 or more seen here are a substantial enhancement. The peaks are not *all* closely correlated with channel constrictions, however: near $x = 70$ and 130 maximum velocity peaks occur, but at these locations the channel is expanding just downstram of a constriction. It is also possible to calculate a “maximum velocity trajectory”, following [38], as the set of (x, y) gridpoints which at each x has the y-value corresponding to the position where the maximum velocity occurs. For the most part our observations concerning the behavior of these trajectories is similar to that reported in this reference, but we do not observe the line-length of this trajectory decreasing monotonically with Re.

Comparing the other fluids to the Newtonian case, we see in Fig. 3.6 that the global maximum absolute velocity always occurs at the narrowest constriction near

$x = 110$ and the other primary peaks always occur at the same positions, $x = 55$ and 240, as well. Furthermore, each peak has roughly the same (normalized) velocity value. In the shear-thinning case, both the variation in x away from the peaks/constrictions and the variation with pressure gradient are weaker than in the other cases, which may be attributed to the fact that typical velocities in the fracture are smaller in this case, and inertial effects play a weaker role. In the shear-thickening case, where typical velocities are larger, the maximum velocity values are larger off the peaks values, and furthermore exhibits rather more variation with x and Re than the other fluids.

The probablity distribution of velocity magnitudes is also of interest [38], since the presence of low and high velocity components strongly influences mixing processes and transport of passive tracers and suspended particles [36]. Histograms of the observed absolute value of the velocity for the three fluids at various pressure gradients are shown in Fig. 3.7. In all cases there is a peak near the origin, which reflects the numerous low-velocity zones in the crevasses at the fracture walls, along with a higher-velocity peak resulting from the rapid flow in the channel constrictions. The latter moves out to higher values as the pressure gradient increases (note the normalization by $\overline{u_x}$ in the figure) Once again, the shear-thickening case behaves somewhat differently than the other two fluids, showing a less prominent and broader "constriction peak," and more variation with G.

3.3.2 Pressure and stress field

The distribution of pressure and stress in the fluid are important for non-Newtonian rheology, and in considering possible erosive processes on the fracture walls. To contrast the behavior of the different fluids, Fig. 3.8 shows the pressure "fluctuations" along the channel for the three power-law fluids $n = 0.75$, 1.0 and 1.25. The fluctuation p' is the deviation in pressure from the imposed linear gradient, which would vanish identically in a Hele Shaw geometry. In the figure, the fluctuation has been normalized by the imposed pressure difference, $\Delta p = GL$, and averaged over the channel width. For all three fluids, the pressure fluctuations are most significant in the vicinity of the main constrictions in the channel where the fluid accelerates, rising just before each constriction's location and dropping rapidly as it is traversed. Some additional structure arises at positions x of bends in the flow path, another source of fluid acceleration. Again, the shear-thinning and Newtonian fluids behave somewhat similarly, while the variation is strongest in the shear-thickening case.

The variation in fluctuation with imposed gradient is shown in Fig. 3.9, and indicates the expected general increase in magnitude with G along the channel.

To assess the effects of the flow on the fracture wall, we first calculate the average force exerted by the fluid on the wall,

$$\mathbf{F} = \frac{1}{L} \int d\ell \, \hat{\boldsymbol{n}} \cdot \boldsymbol{\sigma} \tag{3.9}$$

where the integral runs over the fracture surface (a curve in this two-dimensional calculation), and $\hat{\mathbf{n}}$ is the local normal to the wall. The force is then decomposed into x and y components, representing the average drag and thrust on the wall, respectively, and then normalized by a typical inertial pressure $\rho\overline{u}^2/2$ times the nominal surface area $L \times 1$, to give drag and thrust coefficients

$$d = \frac{F_x}{L\rho\overline{u}^2/2}, \qquad t = \frac{F_y}{L\rho\overline{u}^2/2}. \tag{3.10}$$

Note that aside from the (reasonable) use of the inertial pressure, the remainder of the normalization is somewhat arbitrary but a fixed constant for each fracture, and mainly serves to provide dimensionless drag and thrust coefficients. The drag and thrust forces for the lower and upper walls of the channel are similar but not identical because of the asymmetry of the fluid-solid boundary, and for definiteness we present only the forces on the lower wall.

The results of calculating the drag and thrust coefficients is shown in Figs. 3.10 and 3.11 for the three fluids with exponents $n = 0.75, 1.0, 1.25$. In all cases, the coefficients exhibit simple power-law behavior, provided G is not too large, and the transition to a different behavior at larger G may be associated with the onset of inertial effects (see the following section). This form of scaling behavior result is consistent with the experimental results reported in [21], and the values of the slopes found in the log-log plots in the low-G range, -1.67, -1.02, -0.62 for $n = 0.75$, 1.0 and 1.25, respectively, for *both* drag and thrust, may be understood from the following argument.

If inertial effects are absent, one expects the scaling behavior in a rough channel to be the same as in a straight channel. In that case, from Eq.(3.6) one has $u \sim G^{1/n}$, and therefore $\nabla u \sim G^{1/n}$ as well, so that $\mu \sim |\nabla u|^{n-1} \sim G^{(n-1)/n}$. The drag and thrust forces are proportional to the stress, $\sigma \sim \mu \nabla u \sim G^{(n-1)/n+1/n} \sim G^1$. The drag and thrust *coefficients* are then $d, t \sim F_{x,y}/\overline{u}^2 \sim \sigma/u^2 \sim G^{1-2/n}$, giving exponents -5/3, -1 and -3/5, respectively, for the three fluids.

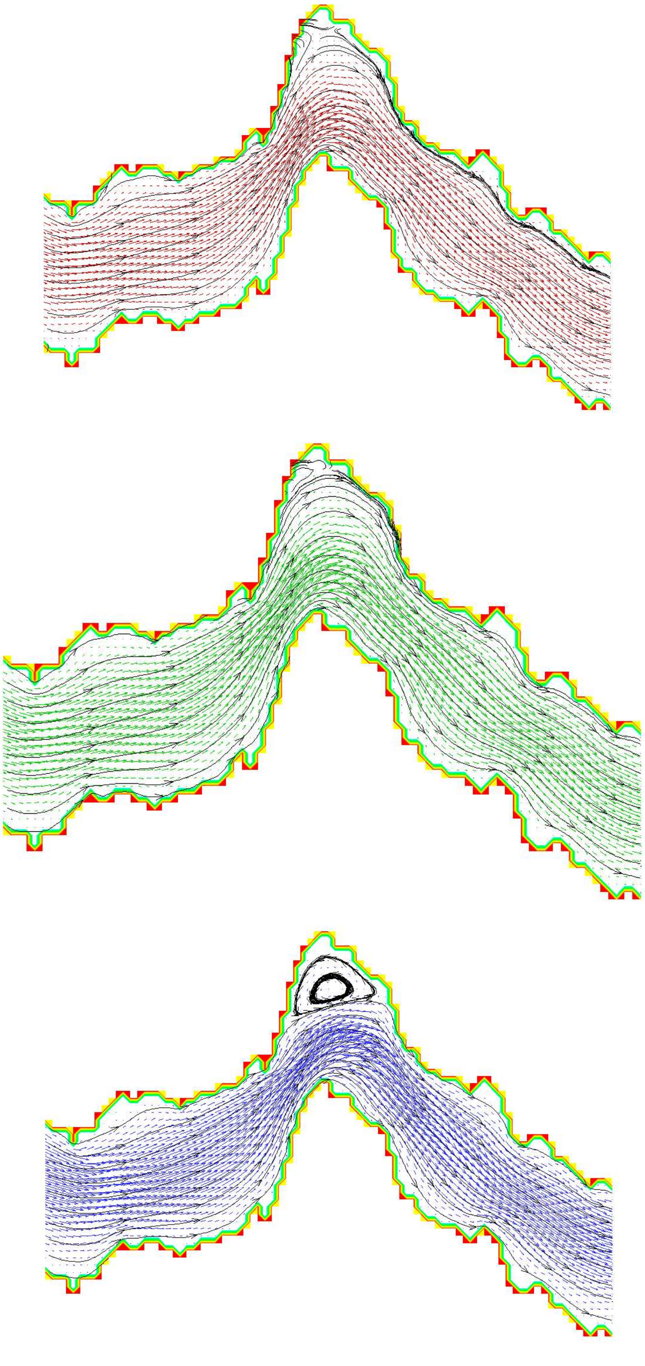

Figure 3.5: Segment of velocity vector field with streamlines of the flow for power-law fluid with $m = 0.01, n = 0.75(top), 1.0(middle), 1.25(bottom)$ and the pressure gradient applied is $G = 1 \times 10^{-6}$. The segment extends from $x = 20$ to $x = 100$.

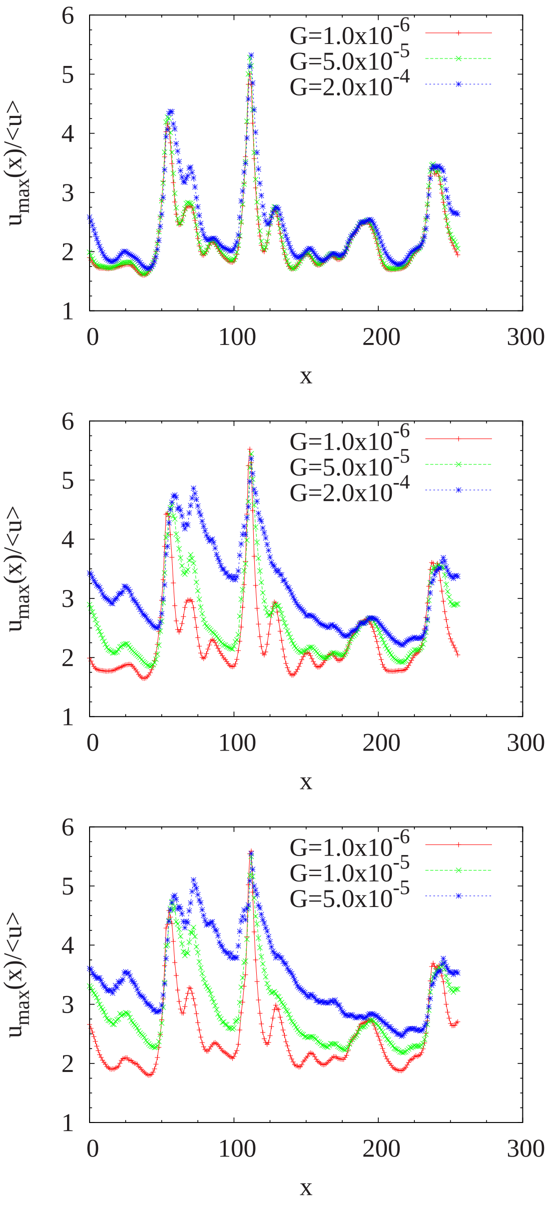

Figure 3.6: Maximum absolute velocity along the fracture channel for shear-thinning(*top*, n=0.75),Newtonian(*middle*, $n = 1.0$), and shear- thickening(*bottom*, n=1.25) fluids for various applied pressure gradient G. Each maximum velocity curve is normalized by the corresponding $\overline{u_x}$, the average flow velocity in the x-direction.

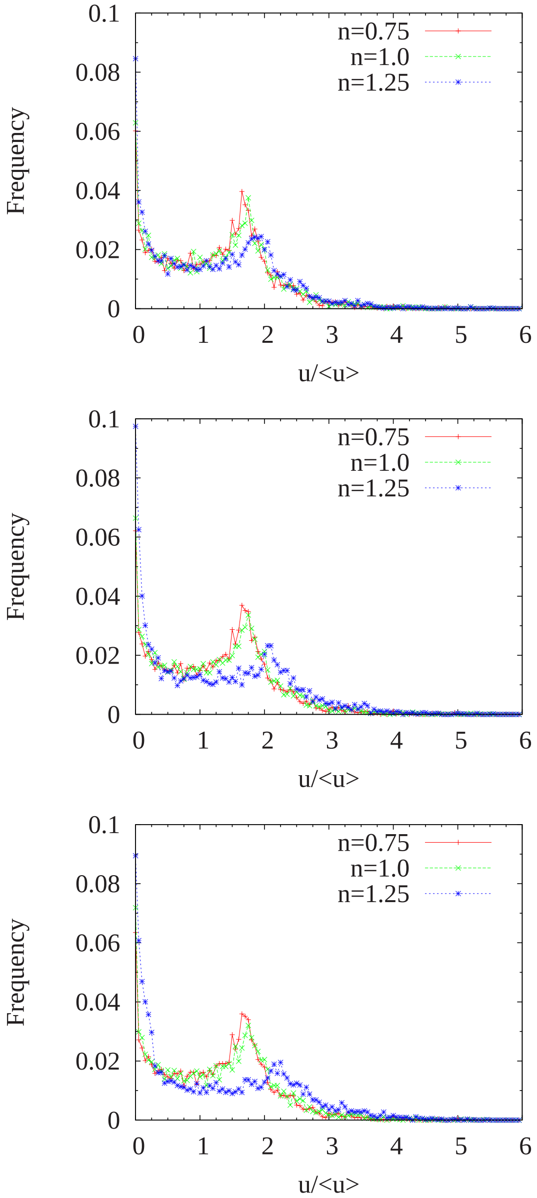

Figure 3.7: Distribution of normalized absolute velocity in the whole self-affine fracture flow domain for different power-law fluids with pressure gradients $G = 1.0e-6$, $5.0e-6$ and $1.0e-5$ (top to bottom).

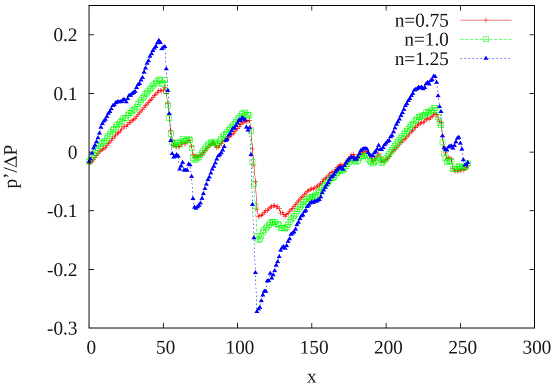

Figure 3.8: Normalized pressure fluctuation along the channel for different power-law fluids, at pressure gradient $G = 1.0e - 5$.

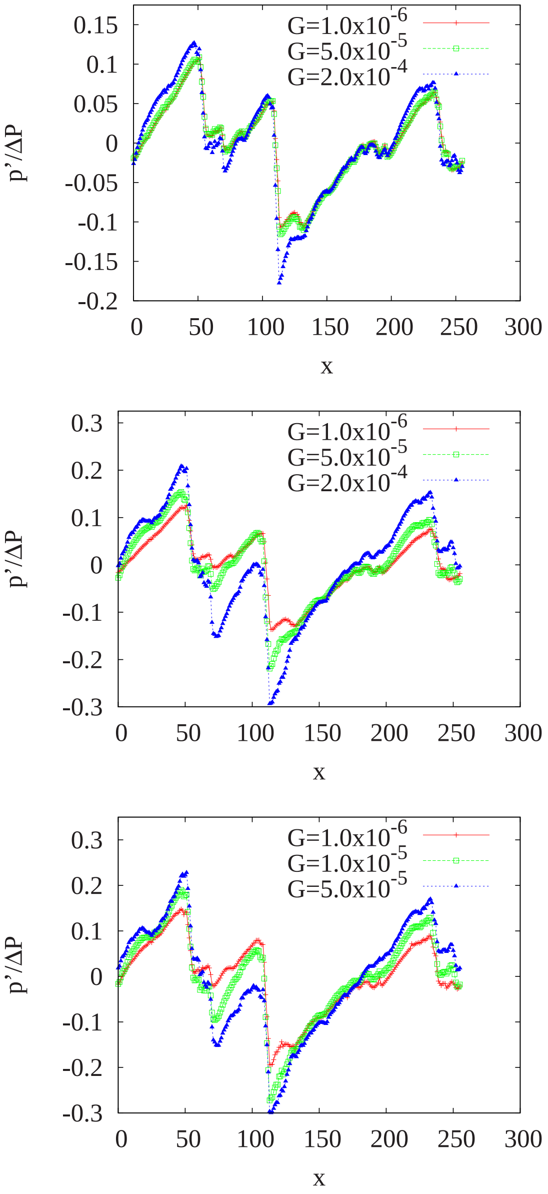

Figure 3.9: Pressure fluctuations of different fluids with power $n = 0.75, 1.0, 1.25$ and $m = 0.01$ along a self-affine fracture channel under different applied pressure gradients.

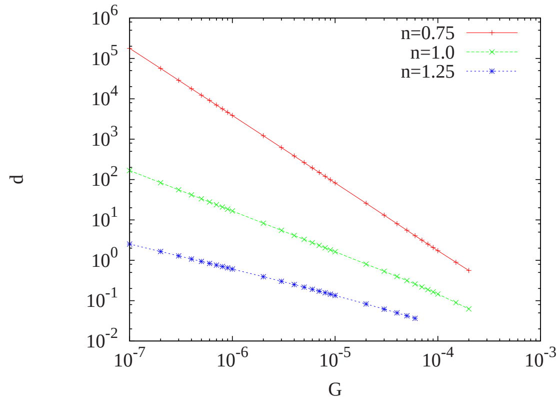

Figure 3.10: Drag factor d for power-law fluids in a self-affine fracture channel as a function of applied pressure gradient.

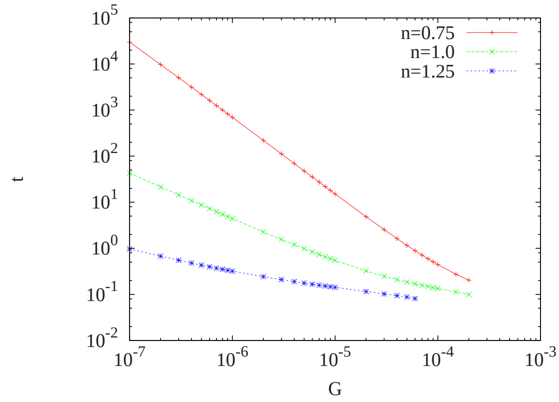

Figure 3.11: Thrust factor t for power-law fluids in a self-affine fracture channel as a function of applied pressure gradient.

3.4 Permeability

Next we consider global behavior – the permeability of a self-affine fracture channel. Our discussion is colored by analogies to flow in intergranular porous media, so we first recall the situation in that system [5]. For Newtonian fluids in the low Reynolds number limit, the definition of intergranular permeability is given by Darcy's law, $\langle \mathbf{u} \rangle = -(k/\mu)\nabla p$, where $\langle \mathbf{u} \rangle$ is the average flow velocity and p the average pressure. The average in question could be a volume average or an ensemble average, and for a flow which is macrosopically unidirectional, an operational definition of permeability is $k = \mu QL/A\Delta p$ where Q is the flux through a sample of cross-sectional area A and length L. In a two-dimensional situation, the area is replaced by the width W, and Q is the flow per unit length in the third direction. A definition identical to the latter case may be used for the permeability of low Reynolds number Newtonian flow in a fracture. Both finite Reynolds number flow and non-Newtonian fluid rheology modify this description. We first consider the effects of inertia, and then examine how permeability relates to the fracture morphology.

3.4.1 Inertial effects

At higher flow rates when inertial effects appear, the relation between pressure difference and average velocity or flux becomes nonlinear and one may write

$$\Delta p = \alpha Q + [\,\beta Q^2 \text{ or } \gamma Q^3] \tag{3.11}$$

where α incorporates the Darcy permeability, and the term in brackets is the inertial correction, with $\alpha, \beta > 0$. At high Q the quadratic or "Forchheimer" term applies, but in the transitional region where the Reynolds number is small but finite, a cubic dependence is found. This picture is supported by experiments, analytic calculations, and numerical simulations [45].

The flow of a Newtonian fluid in a self-affine fracture can be described in identical terms, as shown by the numerical simulations of Skjetne *et al.* [38] which exhibit the same transitions between flow regimes indicated in Eq. (3.11). In extending the discussion to power-law fluids, the first issue is to choose the appropriate power of Q. The exact solutions for Hele-Shaw flow given in Eq. (3.7) have the scaling behavior $G \sim Q^n$ where G is the applied pressure gradient (the relevant pressure for macroscopic behavior) and n the power-law index. In a rough fracture, one would naturally expect an identical relation, albeit with a modified coefficient, at low G, and then at larger G inertial effects would be expected to produce (positive) terms involving higher powers of Q. To test this idea, note that we are concerned here with the statistical behavior of self-affine fractures, rather than the details of flow in one particular geometry which was relevant in the previous section, so an ensemble average over six realizations of the fracture surface is used. The simulation results are shown in Fig. 3.12 and indeed show a $G \sim Q^n$ scaling behavior at low G. The Newtonian n=1 plot shows this behavior clearly since G/Q^n is constant at low Q, whereas in the other cases, the expected behavior is present at sufficently small Q as indicated in the alternative plots in the insets of G *vs.* Q. The need for different plotting variables arises because in the non-Newtonian cases, the flow rate fluctuates substantially at low G and division by Q^n is numerically unstable. Beyond the quasi-linear regime, the Newtonian case shows the expected transition to a Forchheimer flow regime $G \sim Q^2$ at larger forcing, and the shear-thickening fluid shows a somewhat analogous behavior $G \sim Q^{2n}$. The shear-thinning fluid is not described by a simple power law at large G, and we are not aware of any theoretical treatment of this problem, so we simply report the numerical results.

To understand the numerical coefficient in the flow results, the fracture-modified

fluid index	k_0	k
$n = 0.75$	2.99	0.373
$n = 1.0$	33.2	4.73
$n = 1.25$	142	20.6

Table 3.1: Effect of roughness and tortuosity on the low Reynolds number permeabilty: k_0 and k are the permeabilities (defined in Eq. (3.12) for a Hele-Shaw cell and a self-affine fracture of the same mean aperture, respectively.

Darcy permeability, we again refer to the Hele Shaw case and define

$$k = \frac{m^{1/n}\overline{u}}{G^{1/n}}. \tag{3.12}$$

Since the roughness and tortuosity of the fracture cause the streamlines to bend and viscous dissipation to increase, the permeability should be reduced compared to a smooth and flat Hele Shaw geometry of the same aperture. In Table I, the various permeabilities are compared, and a reduction by a factor 6-7 is found.

So far, we have expressed the pressure gradient G in terms of the flux Q, because these quantities are well defined in the present simulations. However, for general purposes, it is preferable to use a dimensionless quantity such as the Reynolds number as the independent variable, but the definition of Re for power-law fluids is not entirely obvious for power-law fluids because the the viscosity varies over the flow domain. One way to combine the results for different fluids is based on an analogy to the friction factor scaling laws for flow in pipes originally due to Nikaradze [81], which can be extended to non-Newtonian fluids as shown by Metzner [58]. Recall that for unidirectional flow of a Newtonian fluid of viscosity μ in a pipe of diameter D, the mean velocity is $\overline{u} = GD^2/32\mu$ and the shear stress at the wall is $\tau_w = GD/4$, so if one defines the conventional friction factor as $f = \tau_w/\frac{1}{2}\rho\overline{u}^2$, then one finds $f = 16/Re$ where $Re = \rho\overline{u}D/\mu$. Experiments follow this scaling law up to a value of Re that depends on the roughness of the pipe, and at larger values of Re, f levels off. An analogous calculation for Hele Shaw flow using the aperture H instead of the diameter D gives $\tau_w = GH/2$ and $f = 12/Re$. The power-law generalization is to use the latter form for τ_w, along with Eq. (3.7) to express the pressure gradient in terms of the mean velocity, and yields

$$f = \frac{12}{Re} \qquad \text{if} \quad Re \equiv 6\rho\overline{u}^{2-n}H^n/m', \tag{3.13}$$

where $m' = m(2(2n+1)/n)^n$. This choice of variables is not the last word, because in the analogous interganular porous medium case where a similar approach has been taken [21], extra constant factors such as functions of the porosity or the "dynamic specific surface area" are introduced into the friction factor and Reynolds number definitions to promote data collapse. It is not clear how such ad hoc factors might be interjected here, so instead we collapse the data using a simple constant factor which varies from fluid to fluid, and the result is shown in Fig. 3.13. Two different values of the Hurst exponent are shown, and in both cases we see an $f \sim 1/Re$ scaling at low Re, a transition at $Re \sim 1 - 10$ and perhaps a constant friction factor at larger Re. Unfortunately, the calculations cannot be extended into the latter regime using the present method (a particular implementation of the lattice Bolzmann technique) because numerical instabilities arise.

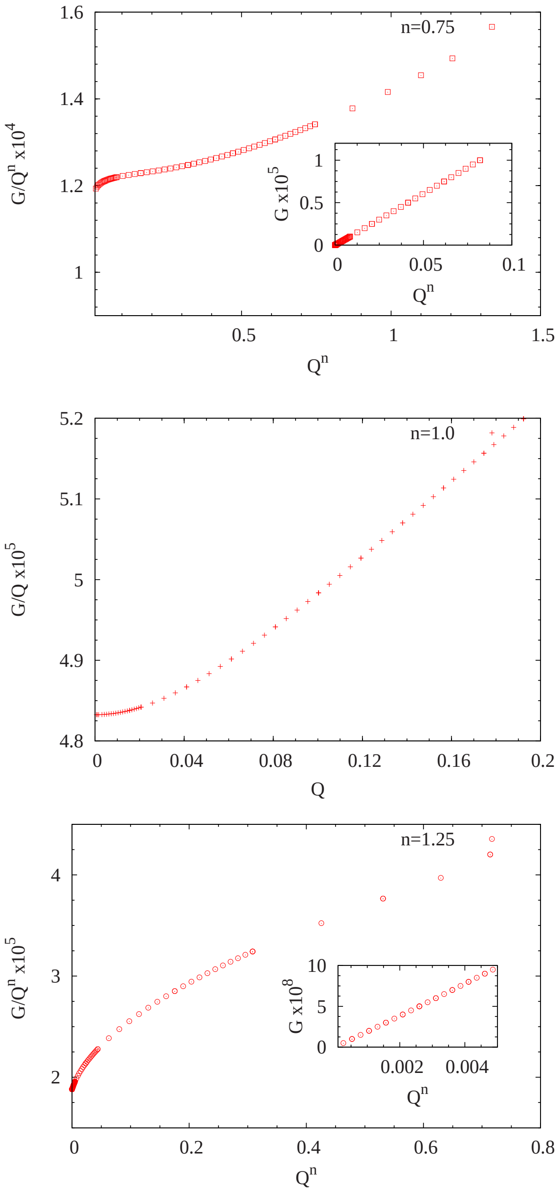

Figure 3.12: Relation between imposed pressure gradient and fluid flux for power law fluids: $n = 0.75$, 1.0 and 1.25 (top to bottom).

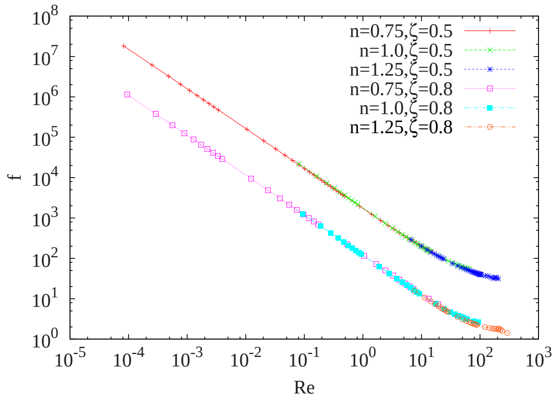

Figure 3.13: Friction factor of self-affine fracture channels of Hurst exponent $\zeta = 0.5$ and 0.8 as a function of Reynolds number defined as in eq.3.13 for power-law fluids with $n = 0.75, 1.0, 1.25$.

3.4.2 Morphology effects

We now consider how the geometry of the fracture effects the (low-Reynolds number) permeability for the various fluids considered. First we investigate the effect of the Hurst exponent ζ on the permeability, and to simplify the analysis we consider a fracture channel with one self-affine wall and one flat wall, as in [26]. For a fixed presure gradient G, we compute the flux as a function of the channel length L for the three fluids, and in Fig. 3.14, we first show the flow rate depletion $(Q_0 - Q)/Q_0$ *vs.* L for a fracture with $\zeta = 0.8$. Here Q_0 is the flux through a flat-walled channel fo the same mean aperture. Increasing the length allows for more fluctuation in the channel width (see Eq. (3.2) which increases the tortuosity and tends to decrease the flux. If the Hurst exponent of the channel's rough wall is instead $\zeta = 0.5$, the three fluids again behave quite similarly, so it suffices to compare the behavior of different Hurst exponents for a single case, and in the lower panel of the figure we plot the flux depletions for the two exponents for the shear-thinning case. The fact that the flux depletion is greater for the $\zeta = 0.8$ channel may be explained by noting that this exponent value corresponds to more fluctuation as a function of L than the 0.5 case, and therefore to a more tortuous channel.

To relate the flux to the channel aperture, we imagine dividing the channel into a sequence of nearly-straight sections, each of length ℓ_i, and writing the total pressure difference as the sum of the pressure drops in each section, using Eq. 3.7 for each. This reasoning yields

$$\Delta P = \sum_i \Delta P_i = \sum_i \left[Q \cdot \frac{2n+1}{n} \cdot b_i^{-\frac{2n+1}{n}} \right]^n \cdot m \cdot 2^{n+1} \cdot l_i, \tag{3.14}$$

where the summation is over the sections, and b_i is the effective aperture and l_i is the length along the local flow direction in section i, and we have noted that Q is a the same in all sections. If θ_i is the angle between the orientation of channel section

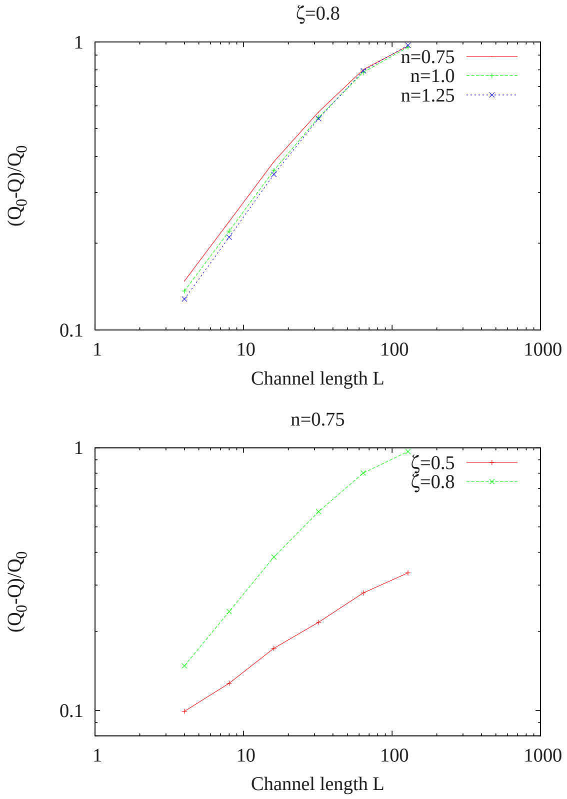

Figure 3.14: Flux variation with length in a channel with one self-affine and one flat wall for different fluids and Hurst exponents. The maximum aperture of the channel is $H_{\max} = 64$, and the applied pressure gradient is $G = 1.0 \times 10^{-6}$. Top: flux depletion for different fluids confined in a channel with $\zeta = 0.8$. Right: flux depletion for a shear-thinning fluid in channels of different ζ.

i and the mean flow direction, then $b_i = H \cos\theta_i$ and $l_i = l_i^{\|}/\cos\theta_i$, where H is the aperture and $l^{\|}$ is the projected length of section i in the mean flow direction, assumed to be the same for all sections. Using these relations in Eq.3.14 we have

$$\Delta P = 2mQ\, l^{\|} \left[2\frac{2n+1}{n} H^{-\frac{2n+1}{n}} \right]^n \sum_i (\cos\theta_i)^{-(2n+2)}. \tag{3.15}$$

This result generalizes Eq. 26 in [26] to power-law fluids, and if we proceed as in that reference to evaluate the average over angles θ_i we obtain

$$Q - Q_0 \sim H^{(2\zeta-2)/\zeta+(2n+1)/n} \tag{3.16}$$

where again Q_0 is the flux in a flat channel of the same aperture H.

To test the relation 3.16, we calculate the flow for fracture channels of length $L = 256$ with varying apertures $H = 8, 12, 16, 20, 24$, for fluid with $m = 0.01$, n=0.75, 1.0 and 1.25, all at a pressure gradient $\Delta P/L = 1.0e-6$. Figure 3.15 shows the flux depletion $(Q_0 - Q)$ as a function of aperture. The points are the numerical results and the solid lines are fitted curves, based on the expected power-law exponents obtained from Eq.3.16, which are 2.83, 2.5, and 2.3 for the three fluids. We see that the theoretical analysis is in excellent agreement with the data for the shear-thinning and Newtonian fluids (n=0.75 and 1.0), but the agreement is less satisfactory for the shear-thickening fluid, whose numerical exponent is closer to 2.5. A possible interpretation is that in the shear-thickening case, for the same pressure gradient the average velocity is larger than that for the other fluids, so that fluid inertia comes into play.

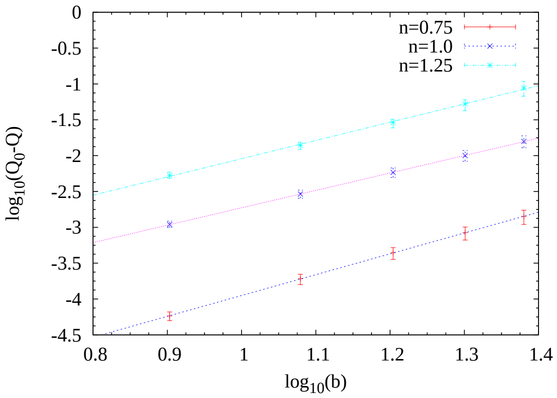

Figure 3.15: Log-log plot of flow rate variations versus the aperture of self-affine channel for different fluids with power $n = 0.75, 1.0$ and 1.25.

Finally, we consider an additional effect, a lateral shift between the two sides of a fracture, which might arise in practice due to geological processes. We begin with a fracture channel with complementary sides and constant initial aperture H, and then shift one side along the mean plane by a distance d. The fracture aperture is now a function of position, $H_d(x)$, and effectively a spatial random function. We again compute the flux depletion relative to a flat channel having the same initial aperture, using six realizations of a self-affine fracture wall with Hurst exponent $\zeta = 0.8$. As shown in Fig. 3.16 the flux decreases somewhat faster than linearly with shift, by producing narrow gaps when proturbances on the two sides are brought closer to one another. The shear-thinning and Newtonian fluids have a fairly similar behavior, while the reduction is twice as large in the shear-thickening case, perhaps again as a result of inertial effects. As in the previous discussion, using a different value $\zeta = 0.5$ for the Hurst exponent gives the same trends.

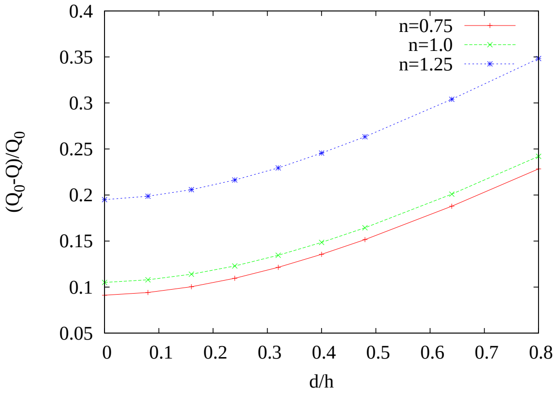

Figure 3.16: Flow rate reduction due to lateral shift along the mean plane of fracture channel for different fluids with power $n = 0.75, 1.0$ and 1.25, and the Hurst exponent used here is $\zeta = 0.8$.

3.5 Conclusion

Using a new implementation of the lattice Boltzmann method for power-law fluids, we have investigated their flow in two-dimensional self-affine fracture channels as a function of applied pressure gradient. Generally, fluids with different power-law index behave in a similar manner when their flow parameters are properly scaled, using standard results for flow in constant-thickness channels. Many previous results for Newtonian fluids in self-affince fractures are found to generalize in a straightforward manner. However, shear-thickening fluids, which have higher velocities for the same pressure gradient than Newtonian or shear-thinning counterparts, are more susceptible to inertial effects.

With regard to the local flow fields, we first considered the maximum absolute velocity as a function of distance along the mean flow direction, which was found to fluctuate along the fracture channel due to its tortuosity and the variable effective aperture along the channel. The local maxima of this maximum absolute velocity occur at points of narrowing or minimal effective aperture, and the range of maximum absolute velocity relative to the global mean velocity ranges from about 1.5 to 5.5. With increasing inertia, this normalized maximum absolute velocity increases for all power-law fluids to different degrees, with shear-thickening fluids having the largest effect and shear-thinning the least. As the pressure gradient increases, the normalized maximum velocities near the constrictions are relatively constant but outside these points velocities tend to increase. The variation in velocity is greatest for a shear-thickening fluid and least for shear-thinning. Pressure fluctuations along the channel increase with forcing for all fluids, and for a given pressure gradient increase with the power-law index n.

The relationship between pressure gradient and flux is found to have the same functional form as for flow in a flat channel, $\Delta p \sim Q^n$, when inertial effects are absent. At higher Δp, Newtonian fluids behave in the same way as in intergranular porous media, and shear-thinning fluids behave analogously, but the shear-thickening case does not show simple power-law behavior. It is possible to collapse all of the data on flux *vs.* pressure gradient into a universal friction factor curve. The variation of flux with system length was shown to scale with system length with an exponent algebraically related to the Hurst exponent, in a manner which generalizes the Newtonian case.

The most interesting question raised by these results is the form of the flux-pressure gradient relationship in the regime of strong inertia in the non-Newtonian case. In this work, we were limited in the range of accessible pressure gradients by numerical instabilities, and it is desirable to improve the algorithm so as to consider higher pressure gradients and further explore the dynamics of the inertial regime. An extension of these considerations to viscoelastic fluids is likewise highly desirable, but new ideas beyond the methods used here are needed.

Chapter 4

Suspension and Deposition in Pressure-driven Flow

The purpose of this chapter is to investigate the flow of a particle suspension flow in a channel, either Hele-Shaw cell with two flat plates or a self-affine fracture, as driven by pressure gradient. The particles are non-neutrally buoyant in general, so gravity plays an important role here in particle transport by causing deposition processes. In Sec.4.1, we introduce the problem we investigate in this chapter, and also give a brief introduction to the lattice Boltzmann method we use to simulate particle suspension flow. Then we analyze our results for bulk flow of particle and fluid phases, both macroscopically and microscopically in Sec.4.2. After these analysis, we conclude with our results and give suggestions on future studies in Sec.4.4.

4.1 Problem description and numerical method

The problem we investigate here is pressure-driven particle suspension flow with deposition process in a Hele-Shaw cell. Because most of mineral particles formed in the subsurface channels are heavier than the fluid media, here we mainly investigate the neutrally buoyant or heavier particle sedimentation process under the pressure driven flow in the channel. And the continuous fluid media is Newtonia. Initially, the particles are uniformly distributed across the whole Hele-Shaw cell except for near wall region because of the wall effect. The suspension is confined by two flat plates. Fig.4.1 and fig.4.2 demonstrate the particle evolution of the suspension flow driven by pressure difference with sedimentation process. An initial homogeneous system evolves to three regions in the field: sedimentation region, suspension region and clear region.

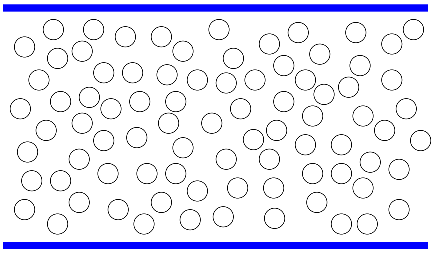

Figure 4.1: Demonstration of initial particle distribution in a Hele-Shaw cell of pressure driven suspension flow with sedimentation.

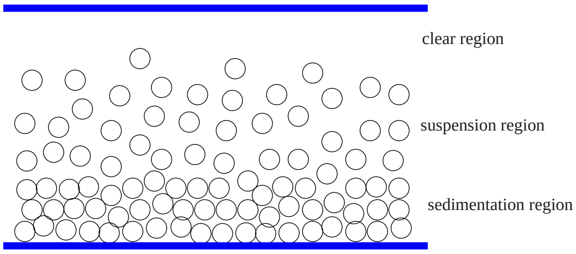

Figure 4.2: Demonstration of evolution of pressure driven suspension flow with sedimentation in a Hele-Shaw cell.

As we could see from these three different regions, the whole fluid and particle transport process is controlled by three non-dimensionalized parameters: particle Reynolds number, buoyancy number and particle concentration. The particle Reynolds number, which describes the flow strength to carry individual particles with the fluid itself locally, and varies through applied pressure difference. The buoyancy number is directly related to the Shields number used in other literature.

The geometry of the Hele-Shaw cell is suspension flow confined by two flat plates, with dimensions in three directions are $L_x \times L_y \times L_z$ with x is the main flow direction, y is the vorticity direction and z is the velocity gradient direction. The dimensions are fixed for this Hele-Shaw cell, and we introduce different numbers of particles into the flow domain to control the bulk particle concentration ϕ_b. The particles in our flow suspension system are monodisperse, and diameter of these particles d are one tenth of the width or L_z of this Hele-Shaw cell, that is $d = L_z/10$. We use periodic boundary conditions along the main flow direction and also along the vorticity direction. The pressure difference applied along the main flow direction is represented by a constant body force in our modeling and simulation. The three dimensionless parameters investigated in our simulation particle Reynolds number, buoyancy number and particle concentration are varied by different pressure gradient applied, different density ratio between solid particles and fluid, and also the particle number in the suspension. Particles are distributed uniformly in the whole Hele-Shaw fluid cell. The time scales in our flow system are the diffusion time on particle scale, that is $t_s = d^2/\nu$, or the sedimentation time $t_g = L_z/U_s$ where U_s is the average or single particle sedimenting velocity, or the convection time scale as $t_c = L_z/U$ where U is the averaged bulk velocity in the mean flow direction. For particle suspension and transport such as deposition, the main time scale is mainly the particle diffusion time for particle migration due to particle fluid hydrodynamic interaction. So here in this system, the diffusion time t_s is used as the unit time scale for time evolution of the particle suspension and deposition process.

To calculate this particle suspension flow, lattice Boltzmann method is utilized for the fluid flow and particle-fluid interaction, and Newtonian dynamics for particle motion. Fluid dynamics is calculated totally from the lattice BGK model, and particle dynamics is updated through Newtonian dynamics. The coupling between the fluid phase and solid particle phase is through the boundary. We update the distribution function in the lattice BGK model to match the no slip boundary condition at the solid fluid interface, and hence the force and torque are calculated through definite rules. Through these rules, the fluid field is modified to accommodate the local boundary conditions imposed by solid fluid interface. The suspension flow is driven by different pressure gradient or more specifically in lattice Boltzmann simulation, by a constant forcing. So the particle Reynolds number and buoyancy number are functions of this applied pressure gradient. For more details, please refer to Ladd[88].

Before analysis of the numerical results, it is necessary here to give exact definitions of two of these three dimensionless parameters: particle Reynolds number and buoyancy number, based on which we will analyze our results further. The buoyancy number measures the relative significance of gravitational force on particles and hydrodynamic viscous force, which, in some sense, determines partially the particle translation along the main flow stream and deposition to wall surfaces. We have two alternative choices, one to define the buoyancy number based on the balance of Stokes drag and gravitational force, which gives,

$$N_b = \frac{(\rho_p - \rho_f) g d^2}{18 \eta U}, \tag{4.1}$$

where ρ_p and ρ_f are solid particle and fluid density respectively, g is the acceleration of gravity, d and U are respectively the particle diameter and the average bulk velocity in main flow direction as in the above definition for particle Reynolds number. Since the flow is driven by applying different pressure gradients in all our numerical calculations, the buoyancy number could therefore be defined based on pressure gradient alternatively, as $N_b = (\rho_p - \rho_f)g/G$, G is the pressure gradient applied, as in Norman et al[65]. This definition is convenient in that it is directly related to our calculation data, but in most literature for particle suspension and transport, the first definition in eq.4.1 is used, so here we follow the convention to use the first definition. The particle buoyancy number is mainly controlled by density difference between solid particles and fluid media. On the other hand, Reynolds number is used to describe the flow strength and its effect on the motion of particles. Similar to the buoyancy number definition, according to different length scales and velocity, several Reynolds number definitions could be proposed. Because particle transport process is incorporated and is related to particle motion induced by hydrodynamic forces on it, particle Reynolds number, based on the particle dimension and average bulk velocity is appropriate in this situation. So this particle Reynolds number is defined as the following,

$$Re_p = \frac{\rho U d}{\eta}, \tag{4.2}$$

where ρ is fluid density, U is the average bulk velocity in main flow direction, d is particle diameter and η is the fluid viscosity. Moreover, in all our calculations to control particle Reynolds number, we change the pressure gradient applied to drive the suspension. But similar to buoyancy number, the particle Reynolds number Re_p is not only determined by the the applied pressure gradient G, but by other factors such as bulk concentration ϕ_b and density ratio between solid particles and fluid. We will give more details on this in later sections.

4.2 Results and discussion

In this section, we discuss the effect of particle Reynolds number Re_p, the buoyancy number N_b, and concentration ϕ on the suspension flow along a channel composed of two flat plates or a Hele-Shaw cell in fully three dimension. Particle Reynolds number and buoyancy number are both defined in the previous problem specification section. As in all our calculations, we can only control the pressure difference we applied at two ends or the pressure gradient in x-direction, with a specific Newtonian fluid media, so the particle Reynolds number and buoyancy number is indirectly controlled by this applied pressure gradient as G in our presentation with the density ratio and fluid viscosity. The calculation results are analyzed for bulk flow properties under different flow conditions and also for particle dynamics in the suspension flow on a microscopic level.

4.2.1 macroscopic fluid flow and particle transport

Macroscopically, with particle suspended in fluid, the fluid flow field will be modified by the existence of those particles. As a whole, the bulk flow of particle and fluid mixture will be different from the pure fluid flow. In this section, we want to investigate the effects under different dimensionless parameters, *i.e.*, particle Reynolds number, buoyancy number and particle concentration, on the macroscopic flow properties such as the bulk flux, fluid flux and particle flux.

Bulk flow and velocity

As in different industrial processes, it is important to check the flow of overall particulate materials as a bulk under various flow conditions. The results in this section will focus on the bulk flow properties across the flow channel,under different particle Reynolds number, buoyancy number and different particle concentration.

In all cases of our calculations of the particle suspension with neutrally buoyant particles, three groups of pressure gradient are applied along the flow channel, for bulk particle concentration 0.13, 0.26, and 0.34. According to the above definitions of particle Reynolds number, these will give us three groups of particle Reynolds number corresponding to zero buoyancy number for particle suspension at these bulk particle concentrations. As in Table.4.2.1, we calculate the particle Reynolds number according to the bulk mean velocity in the mean flow direction for three groups of particle concentration. As shown in fig.4.3,with the same applied pressure gradients, for neutrally-buoyant particle suspension with different concentration, the bulk mean velocity in the pressure gradient direction decreases with concentration, for with higher concentration, the dissipation is larger for the flow. And with larger applied pressure gradient, the bulk velocity is larger.

Cases	G	U	Q	Re_p	$Re_{channel}$
			ϕ=0.13		
1	1×10^{-6}	0.0050	15.37	0.50	5.0
2	5×10^{-6}	0.0247	75.76	2.47	24.7
3	1×10^{-5}	0.0504	154.8	5.04	50.4
			ϕ=0.26		
1	1×10^{-6}	0.0030	9.15	0.30	3.0
2	5×10^{-6}	0.0147	44.95	1.47	14.7
3	1×10^{-5}	0.0288	88.43	2.88	28.8
			ϕ=0.34		
1	1×10^{-6}	0.0014	4.29	0.14	1.4
2	5×10^{-6}	0.0085	26.17	0.85	8.5
3	1×10^{-5}	0.0178	54.74	1.78	17.8

Table 4.1: Particle Reynolds number at different applied pressure gradient for particle suspension with neutrally-buoyant particles for three groups of particle concentrations.

We have also investigated the bulk velocity field for neutrally-buoyant particle suspension flow with different particle Reynolds number and particle concentration. Figure4.4 shows the normalized bulk velocity profile across the flow channel for

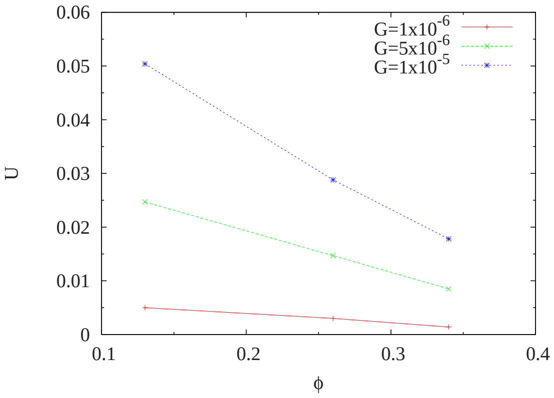

Figure 4.3: Mean bulk velocity of neutrally-buoyant particle suspension flow with different applied pressure gradients and particle concentrations.

bulk concentration $\phi_b = 0.13$ with different applied pressure gradients G. The normalization is based on the maximum fluid velocity under the same pressure gradient for pure fluid flow with the same flow geometry. The normalized velocity profile is almost the same everywhere except the center region. On the center, the normalized bulk velocity is a little higher for low pressure gradient applied and lower for higher gradients applied. This same observation is also true for the velocity profile with bulk concentration $\phi_b = 0.26$ and 0.34. In fig.4.5, the normalized bulk velocity profiles are shown for different bulk particle concentrations under the same applied pressure gradient $G = 5 \times 10^{-6}$. The maximum velocity is on the center plane of flow channel for each bulk particle concentration ϕ_b, and as ϕ_b increases, the maximum velocity decreases and the velocity profile becomes more blunt at the center region, which is also true for concentrated neutrally-buoyant particle suspensions in low-Reynolds number flow, as shown in experiments [53]. This is partially true because at high bulk concentration, the particles at the center region of the flow channel diffuse towards the wall, transfering momentum to the high shear region and flattening the velocity profile.

With zero buoyancy number, particles are distributed across the full flow domain, but if the particles are heavier they will settle in the gravitational direction and

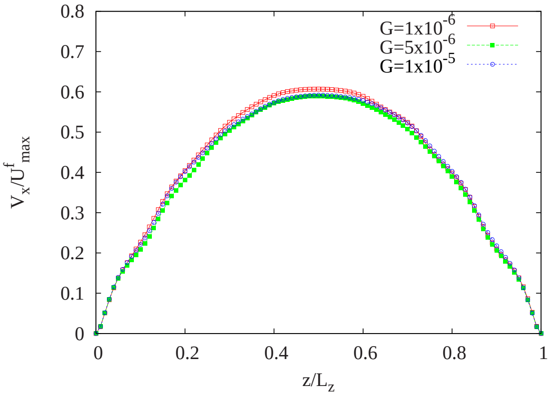

Figure 4.4: Normalized bulk velocity in flow direction for neutrally buoyant particle suspension at $\phi_b = 0.13$ with different applied pressure gradients.

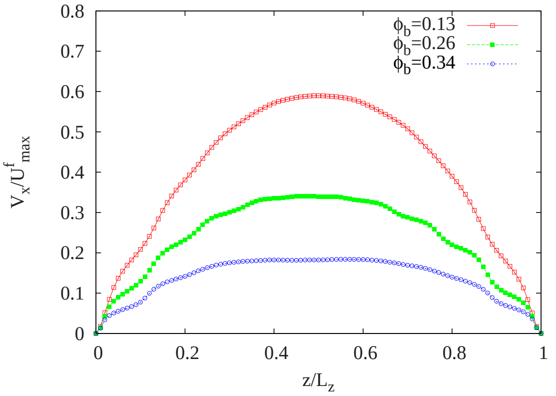

Figure 4.5: Bulk velocity in flow direction normalized by the maximum fluid velocity.

hence to that surface of the wall. These will also change the flow rate of fluid and particle in the main flow direction, and also these will introduce the mechanism to form the deposition bed with dynamical structure, especially on the surface of these deposition layers. Figs.4.6,4.7,4.8 shows the bulk velocity across the flow domain for particle suspensions with different buoyancy number, for suspension with particle bulk concentration $\phi_b = 0.13, 0.26$ and 0.34. As we can see in these figures, at zero buoyancy number, the velocity profile is close to parabolic. For intermediate buoyancy number, three regions are formed across the flow channel. Regions close to the deposition wall, for we do not include any force to stick particles with each other, and to conform the no-slip boundary at the deposition wall, there is a shear layer for particles to move along the deposition wall, with a length of about one diameter of particles. Close to the other wall, there is a clear fluid region with a parabolic velocity in that region. Between these two regions, there is a particle suspension region, bulk velocity increases to the velocity in the fluid region, due to the shear stress exerted by the fluid region on the surface of this layer. For still higher buoyancy number, the fluid shear stress can no longer entrain particles along the channel, and the bulk velocity near the deposition wall becomes negligible due to the particle contact force. For some intermediate buoyancy number, it could be seen that some portion of particles are moving with an almost constant velocity in mean flow direction. This is mainly because we do not incorporate any sticking force for particles, and the particle deposition bed moves with a uniform velocity.

From the mean bulk velocity, with the buoyancy number definition above, we calculate the buoyancy number N_b for some of our calculations.

ϕ=0.13

ρ_p/ρ_f	1.000	1.002	1.006	1.01	1.02	1.04	1.05	1.1
				N_b				
$G = 1 \times 10^{-6}$	0.0	0.087	0.279	0.495	1.525	-	-	-
$G = 5 \times 10^{-6}$	0.0	0.018	0.053	0.092	0.199	0.473	0.680	-
$G = 1 \times 10^{-5}$	0.0	0.009	0.026	0.043	0.089	-	0.253	0.675
				Re_p				
$G = 1 \times 10^{-6}$	0.507	0.511	0.477	0.449	0.291	-	-	-
$G = 5 \times 10^{-6}$	2.469	2.465	2.523	2.428	2.231	1.878	1.635	-
$G = 1 \times 10^{-5}$	5.044	5.069	5.131	5.161	5.011	-	4.394	3.294

Table 4.2: Particle Reynolds number and buoyancy number based on the mean bulk velocities at different applied pressure gradients for particle concentration $\phi = 0.13$, for different particle to fluid density ratios.

ϕ=0.26

ρ_p/ρ_f	1.000	1.002	1.006	1.01	1.05	1.1	1.2	1.3
N_b								
$G = 1 \times 10^{-6}$	0.0	0.155	0.581	7.215	74.884	126.464	208.702	-
$G = 5 \times 10^{-6}$	0.0	0.031	0.093	0.152	1.383	3.231	6.930	-
$G = 1 \times 10^{-5}$	0.0	0.015	0.047	0.076	0.491	1.521	-	5.270
Re_p								
$G = 1 \times 10^{-6}$	0.298	0.288	0.230	0.031	0.015	0.018	0.021	-
$G = 5 \times 10^{-6}$	1.465	1.447	1.428	1.459	0.803	0.688	0.641	-
$G = 1 \times 10^{-5}$	2.881	2.988	2.837	2.931	2.263	1.461	-	1.265

Table 4.3: Particle Reynolds number and buoyancy number based on the mean bulk velocities at different applied pressure gradients for particle concentration $\phi = 0.26$, for different particle to fluid density ratios.

ϕ=0.34

ρ_p/ρ_f	1.000	1.002	1.006	1.01	1.05	1.1	1.2
N_b							
$G = 1 \times 10^{-6}$	0.0	0.320	1.135	2.570	65.161	136.463	-
$G = 5 \times 10^{-6}$	0.0	0.050	0.137	0.217	2.450	5.505	-
$G = 1 \times 10^{-5}$	0.0	0.025	0.066	0.111	0.787	2.688	6.010
Re_p							
$G = 1 \times 10^{-6}$	0.140	0.139	0.118	0.086	0.017	0.016	-
$G = 5 \times 10^{-6}$	0.853	0.882	0.975	1.026	0.454	0.404	-
$G = 1 \times 10^{-5}$	1.783	1.771	2.017	1.997	1.412	0.827	0.740

Table 4.4: Particle Reynolds number and buoyancy number based on the mean bulk velocities at different applied pressure gradients for particle concentration $\phi = 0.34$, for different particle to fluid density ratios.

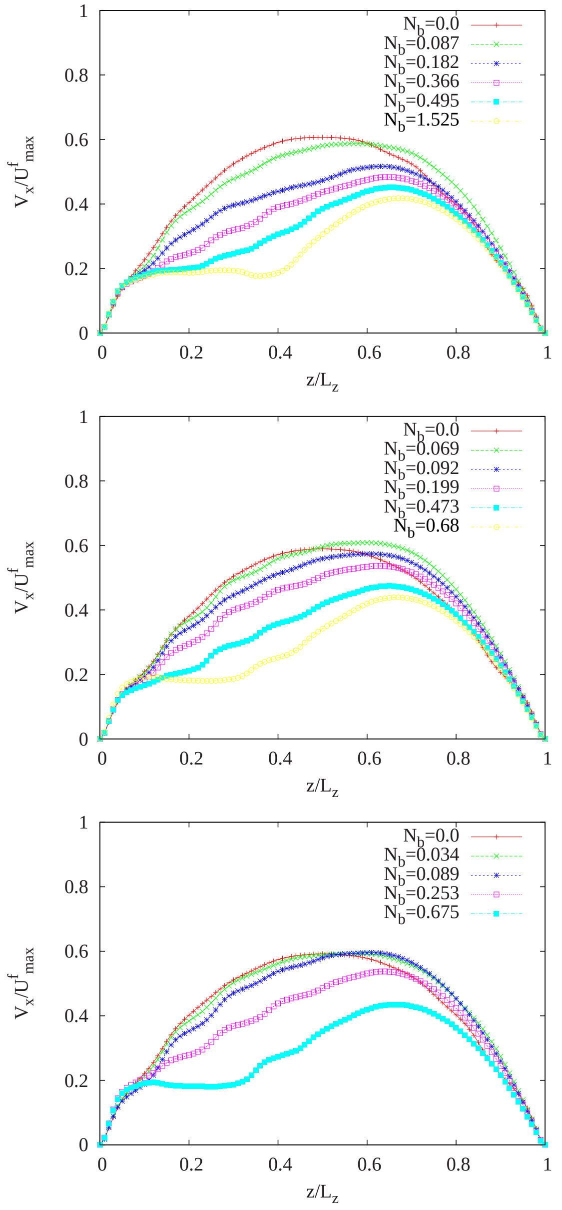

Figure 4.6: Bulk velocity across the flow channel at bulk concentration $\phi_b = 0.13$ and different applied pressure gradients $G = 1 \times 10^{-6}, 5 \times 10^{-6}$ and 1×10^{-5}.

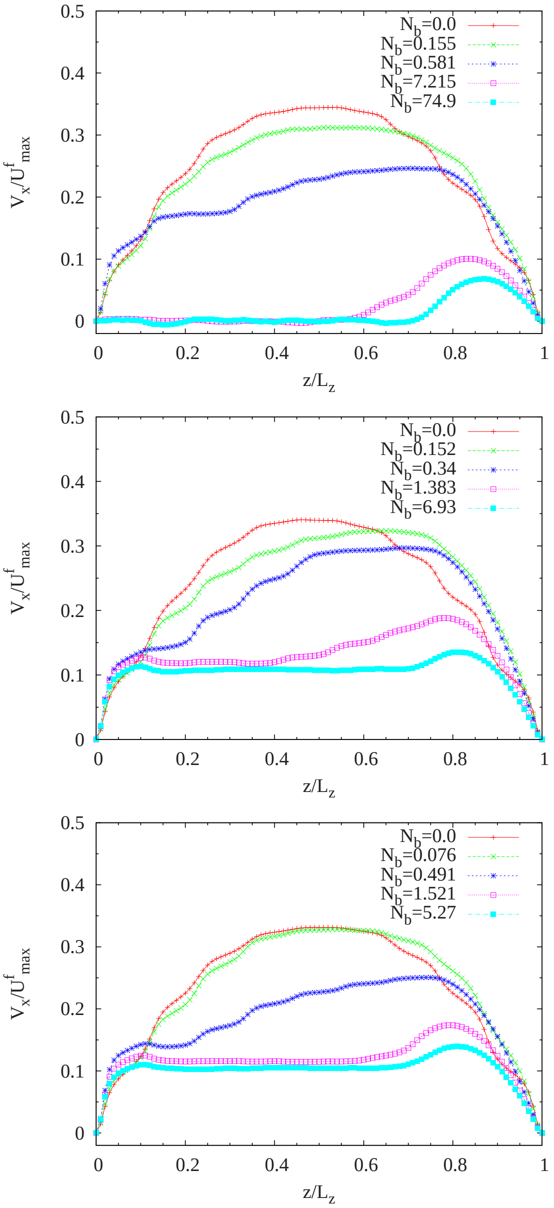

Figure 4.7: Bulk velocity across the flow channel at bulk concentration $\phi_b = 0.26$ and applied pressure gradient $G = 1 \times 10^{-6}$.

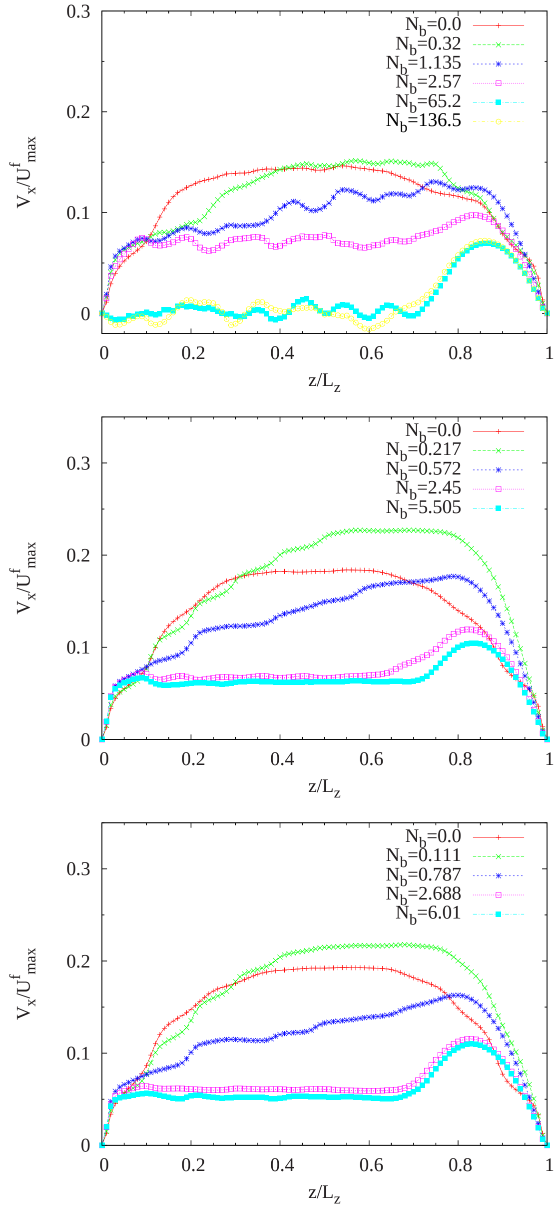

Figure 4.8: Bulk velocity across the flow channel at bulk concentration $\phi_b = 0.34$ and applied pressure gradient $G = 1 \times 10^{-6}$.

Particle concentration distribution

Because of the hydrodynamics and particle diffusion, solid particles will redistribute across the flow domain due to shear stress, particle concentration gradient and so on. Especially, with finite fluid inertia effect, in a pressure driven flow as in our case a single particle will migrate to 0.6 between the center plane and one of the two confining walls, which depends on the initial particle position. As the fluid inertia increases, the equilibrium position for this single particle will displace further to the wall. So this fluid inertia effect will influence the particle distribution, in some way. On the other hand, the gravitational effect will drag the particle bulk toward the wall in the direction of the gravity. This gravitational effect induces large unsymmetrical distribution and suppresses the flow instability induced by flow inertia. This unsymmetrical particle distribution will modify the dissipation of the bulk flow, as we could have seen from the mean bulk velocity in the above section. Because of the finite size of suspended particles in the fluid, the particle concentration fluctuates across the flow channel, as shown in fig.4.9. From this figure, it could be seen that the local particle concentration fluctuates significantly close the wall. The concentration at the center plane is a little higher. Because of these fluctuations

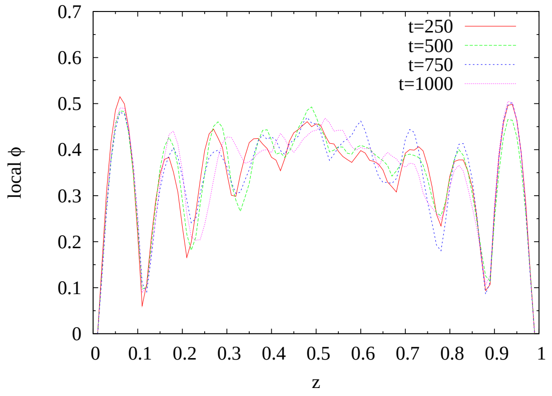

Figure 4.9: Time evolution of local particle concentration across the flow channel for neutrally buoyant($N_b = 0$) particle suspension with bulk concentration $\phi_b = 0.34$ and particle Reynolds number $Re_p = 0.85$.

in particle distribution, it's better to smooth the local particle concentration curves when analyzed. In the following figs.4.11,4.12,4.13, the concentration profiles are all smoothed across the flow domain by averaging over a running window of five bins.

With zero buoyancy number or neutrally buoyant particle suspension, particles are distributed across the full flow domain. As shown in fig.4.10,from the particle concentration profiles in this figure for different bulk concentration ϕ_b at different particle Reynolds number, the peak concentration at the center of the flow channel is much lower with increasing bulk concentration and the particles migrate to the wall away from the centerline. Hence, the profile gets much flatter for higher bulk concentration suspensions. The other interesting thing is that there are some small concentration peaks close the wall, especially for the case $\phi_b = 0.13$ at higher particle Reynolds number or higher applied pressure gradients. The reason for this is that at higher particle Reynolds number, the fluid inertia has a larger effect, which induces larger particle migration across the streamlines. And also because the existence of the wall, particles in that region tend to be caged along the wall to form clusters, which gives higher local concentration.

If the particles get heavier, on the other hand, the bulk of particles will migrate to the gravitational direction and hence to that surface of the wall. This process of deposition is more prominent for higher buoyancy number. These will also change the flow rate of fluid and particle in the main flow direction, and also these will introduce the mechanism to form the deposition bed with dynamical structure, especially on the surface of these deposition layers. Meanwhile, if the pressure gradient applied is increased, particle transport and fluid flow field will be enhanced along with increased fluid inertia. Moreover, particle concentration modifies the structure of the suspension as well, the fluid flux and particle flux also changes along different buoyancy number and particle Reynolds number.

As a result of the interplay of gravitational force and the fluid flow, for non-neutrally buoyant particle, three regions across the flow domain form. As shown in the demonstration figure, these three regions are clear fluid region, suspension region and deposition region. These regions can be seen very clearly from the particle concentration profiles for different bulk concentrations $\phi_b = 0.13, 0.26$ and 0.34, as in figs.4.11,4.12,4.13. For neutrally-buoyant particle suspension, particles fill the whole flow domain. As the buoyancy number increases, particles tend to migrate to the deposition wall, with larger concentration in the half domain close to this deposition wall. For the intermediate buoyancy number, the particle concentration in the center region across the flow domain is still larger than other positions. With buoyancy number increasing further, the particle concentration along the wall gets the largest and then tends to decrease when approaching the center and clear region. At the highest buoyancy numbers, all particles in the flow domain settle down the wall and form a stable deposition structure along the deposition wall. For bulk concentration $\phi_b = 0.13$, the maximum packing is up to about 0.4 of the width of flow channel L_z, which gives a packing number of 0.33. For bulk concentration $\phi_b = 0.26$, the maximum packing is up to about 0.65 of the width of flow channel L_z, which gives a packing number of 0.40. For bulk concentration $\phi_b = 0.34$, the maximum packing is up to about 0.7 of the width of flow channel L_z, which gives a packing number of 0.49. The highest packing concentration along the wall for larger buoyancy numbers are 0.3, 0.4 and 0.5 for bulk particle concentrations $\phi_b = 0.13, 0.26$ and 0.34 respectively.

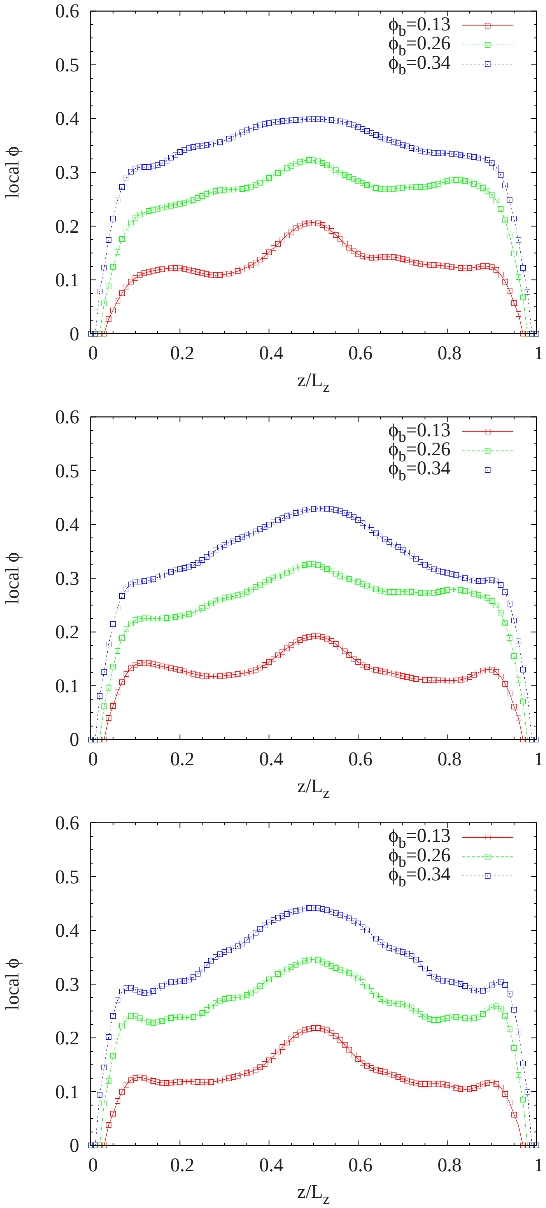

Figure 4.10: Particle concentration across the flow channel for neutrally buoyant particle suspension flow field at different bulk particle concentrations for different applied pressure gradients respectively from top to bottom.

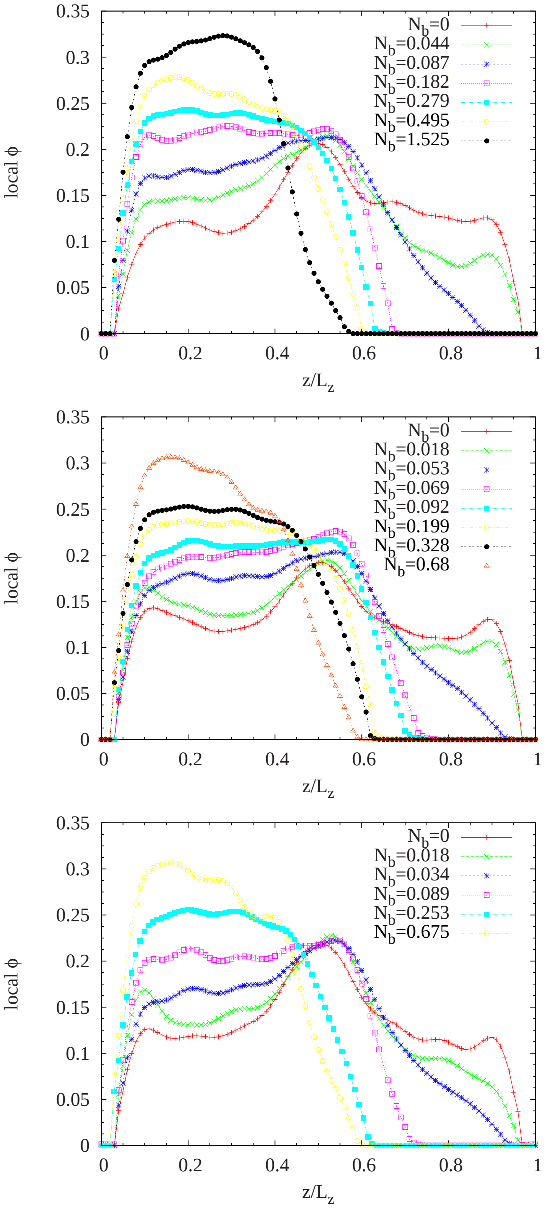

Figure 4.11: Particle concentration across the flow channel for the particle suspension flow field at bulk particle concentration $\phi = 0.13$ for different applied pressure gradients.

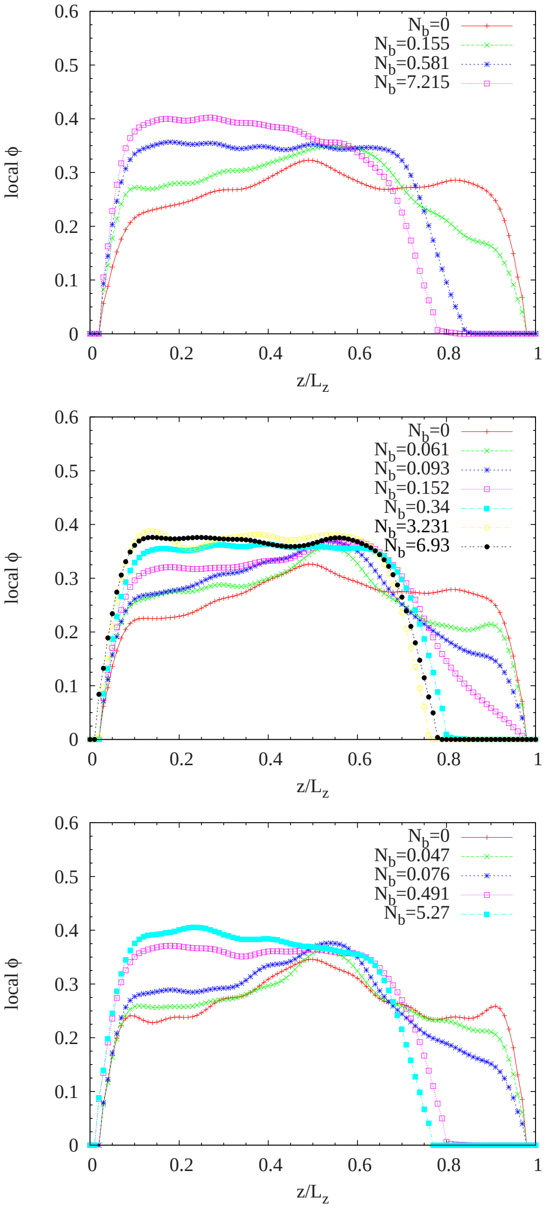

Figure 4.12: Particle concentration across the flow channel for the particle suspension flow field at bulk particle concentration $\phi = 0.26$ for different applied pressure gradients.

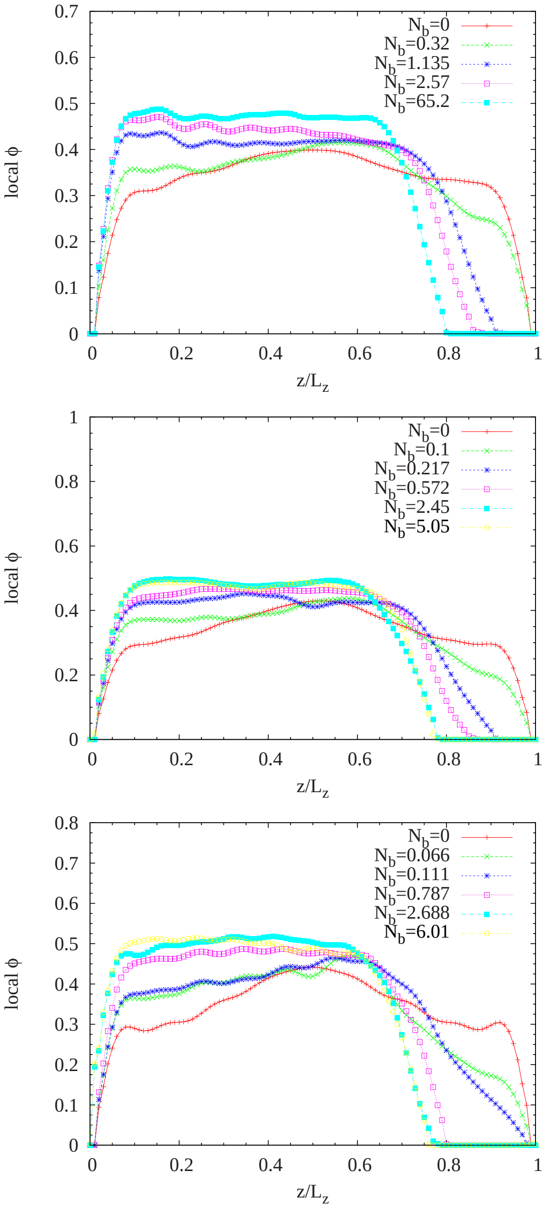

Figure 4.13: Particle concentration across the flow channel for the particle suspension flow field at bulk particle concentration $\phi = 0.34$ for different applied pressure gradients.

Fluid velocity and flux

For particles with a different density from the fluid, the suspension and deposition processes affect the fluid flux and therefore the permeability if we look at it as a dynamic porous media. It is interesting to analyze the effects of flow strength and the particle density relative to the fluid on the fluid flux and velocity. Firstly, due to the existence of the particles, the fluid flow will be distorted, and also because of the dissipation and particle inertia, the fluid velocity will be reduced by dissipation. In fig.4.14, Q_0 is a normalization factor for the fluid flux, it is the effective fluid flux in the flow channel if we compress particles as part of a stationary solid wall, that reads,

$$Q_0 = (1-\phi_b)\frac{\rho G L_z^3 L_y}{12\eta}, \tag{4.3}$$

where G is the applied pressure gradient.

Relative flow rate for particle suspension flow with bulk concentrations $\phi_b = 0.13, 0.26$ and 0.34 are shown in fig.4.14. The relative flow rate for neutrally-buoyant particle suspension at $\phi_b = 0.13$ is about 0.6 for different applied pressure gradients, and about 0.35 and 0.2 for bulk concentration $\phi_b = 0.26$ and 0.34 respectively. At small buoyancy numbers, the relative flow rate goes up a little especially for higher concentration and larger applied pressure gradient G. Then with increasing buoyancy number for all bulk concentrations, the relative flow rate decreases. For $\phi_b = 0.13$, the relative flow rate reaches 0.4, while for $\phi_b = 0.13$ and 0.34, the relative flow rates reach 0.15 and 0.1 respectively. The initial increase of the relative flow rate could be seen from the fluid velocity profile, as in Fig.4.15 for $\phi_b = 0.34$. As the buoyancy number increases, the velocity profile becomes distorted and shifts to the upper wall, and there is somewhat lower concentration or even clear fluid region, and this lower concentration or clear fluid region contributes less dissipation and produce even higher maximum velocity. All these factors contribute to the initial increase of the relative flow rate at small buoyancy number.

Particle velocity and flux

The time averaged particle velocity after the suspension reaches steady state for three bulk concentrations $\phi_b = 0.13, 0.26$ and 0.34, under different applied pressure gradients,s shown in Fig.4.16. As we see, the particle velocity increases with the applied pressure gradient for all bulk concentrations. For a specific bulk concentration, such as $\phi_b = 0.26$, the particle velocity increases first and then decreases with the buoyancy number. The initial increasing trend is more prominent for higher applied pressure gradient G. At larger buoyancy number, the particle velocity goes to a constant level, so that the particle flux is almost a constant in the main flow x-direction. The initial increase in particle velocity along with the buoyancy number has the same mechanism with the similar trend for fluid flux. At the lower end of the buouancy number range, particles migrate to the main flow stream away from one wall, and particles in that region catch up with the local fluid velocity, which is higher away from the wall. And this migration makes the averaged particle velocity gets larger at small buoyancy number.

4.2.2 Microscopic structure of the particle suspension and deposition

In this section we will focus on microscopic structure analysis of the particle transport, and its relation to those macroscopic properties of the fluid and particle transport under different operating parameters.

Clear region formation

At steady state, the shear stress on the interface between the pure fluid region and the deposition bed determines the erosion and sediment balance due to hydrodynamic interaction. This balance also determines the range of three different regions, such as clear region, suspension region and deposition region.

As shown in fig.4.17 for the relative width of the clear region to that of the whole width of the channel increases with particle buoyancy number for all three bulk concentrations $\phi_b = 0.13, 0.26, 0.34$, meaning that the particles fill in a smaller region of the flow domain. With larger buoyancy number, for all suspension flow with three bulk concentrations, the width of clear region goes to a constant, and hence the particle bed to the deposition wall reaches a relatively stable structure. For suspension flow with bulk particle concentration $\phi_b = 0.13$, the particle deposition bed reaches it stable structure at $N_b = 1$ or so. The width of clear region of this case with full deposition is about 0.38. For suspension flow with $\phi_b = 0.26$, the particle deposition reaches stable for buoyancy number at about 4.0 and the width of clear region is about 0.15 for lower applied pressure gradient, and about 0.20 for two other higher applied pressure gradients. For suspension with $\phi_b = 0.34$, at about $N_b = 6$ the deposition bed reaches a stable layering structure, and the widths are 0.16,0.18,0.24 respectively for three different applied pressure gradients. For higher bulk concentrations within the same range of the buoyancy number, the deposition bed has a more closely packed structure as shown with larger clear fluid regions. One explanation for this is that for higher bulk concentration, with higher driving force or pressure gradient, the particles have longer time to flight in main flow stream and then have longer time to relax to a more closely packing structure during their deposition onto the wall surface or layers of deposited particles.

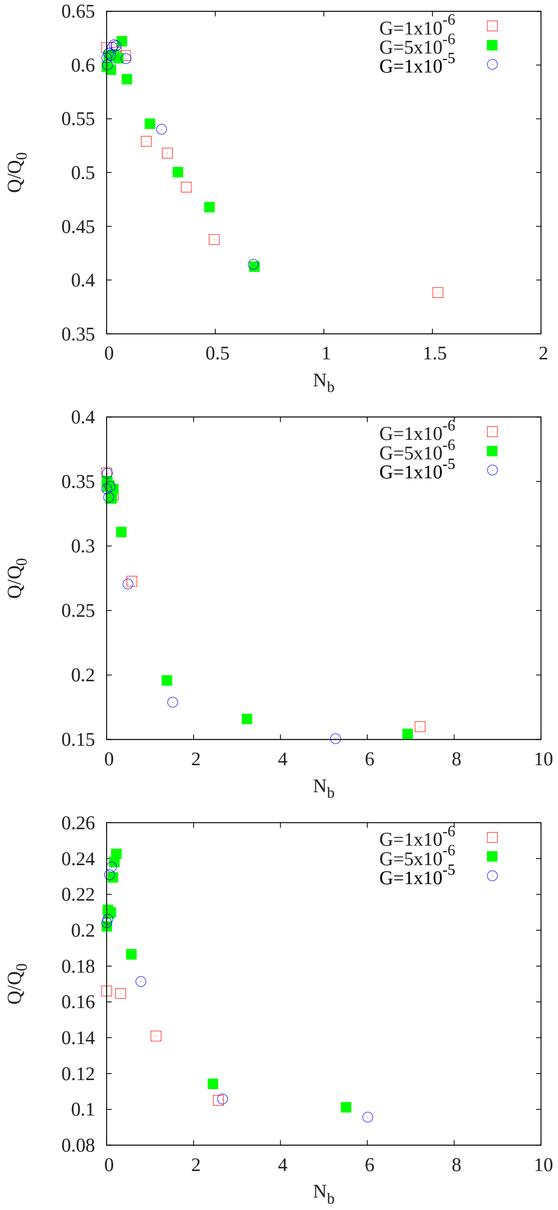

Figure 4.14: Fluid flux along the Hele-Shaw cell for particle suspension flow of different bulk concentrations $\phi_b = 0.13, 0.26$ and 0.34 with different particle Reynolds number or applied pressure gradients.

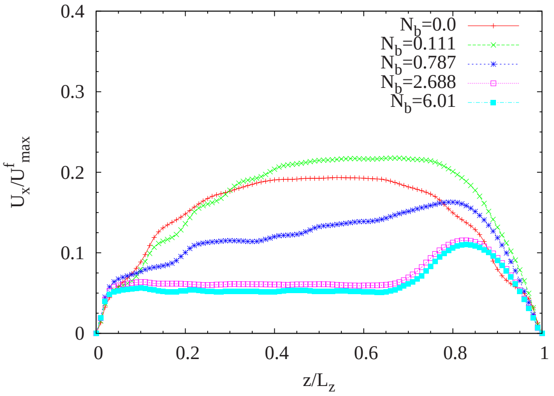

Figure 4.15: Fluid velocity profile across the Hele-Shaw cell for particle suspension flow at different buoyancy number at bulk concentration $\phi_b = 0.34$ and applied pressure gradient $G = 1 \times 10^{-5}$.

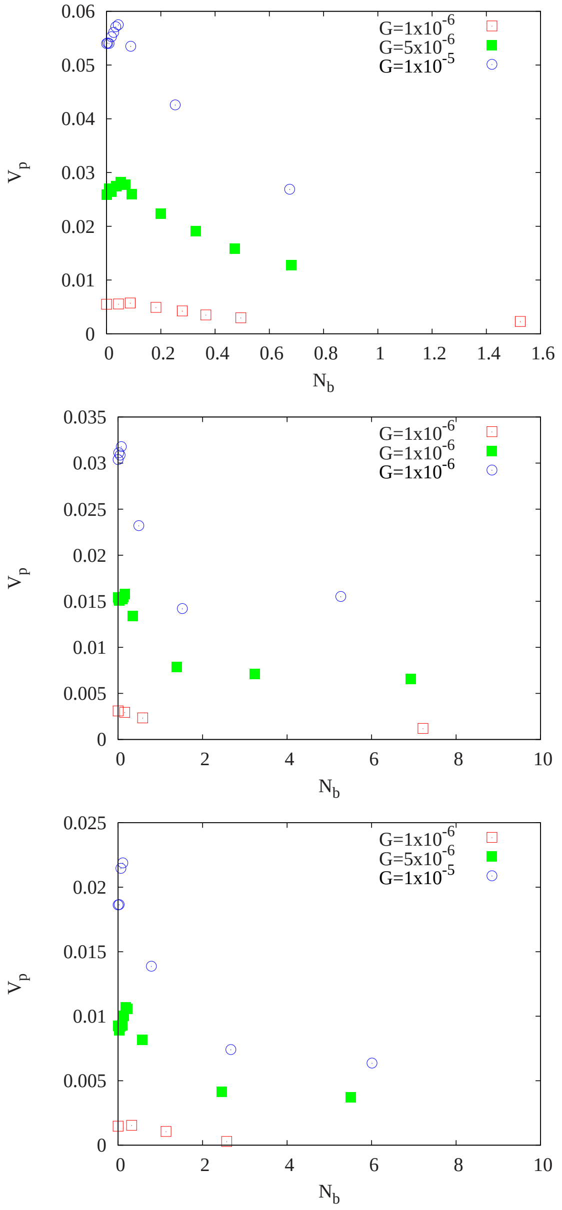

Figure 4.16: Averaged particle velocity along the Hele-Shaw cell for particle suspension flow of different bulk concentrations $\phi_b = 0.13, 0.26$ and 0.34 with different particle Reynolds number or applied pressure gradients.

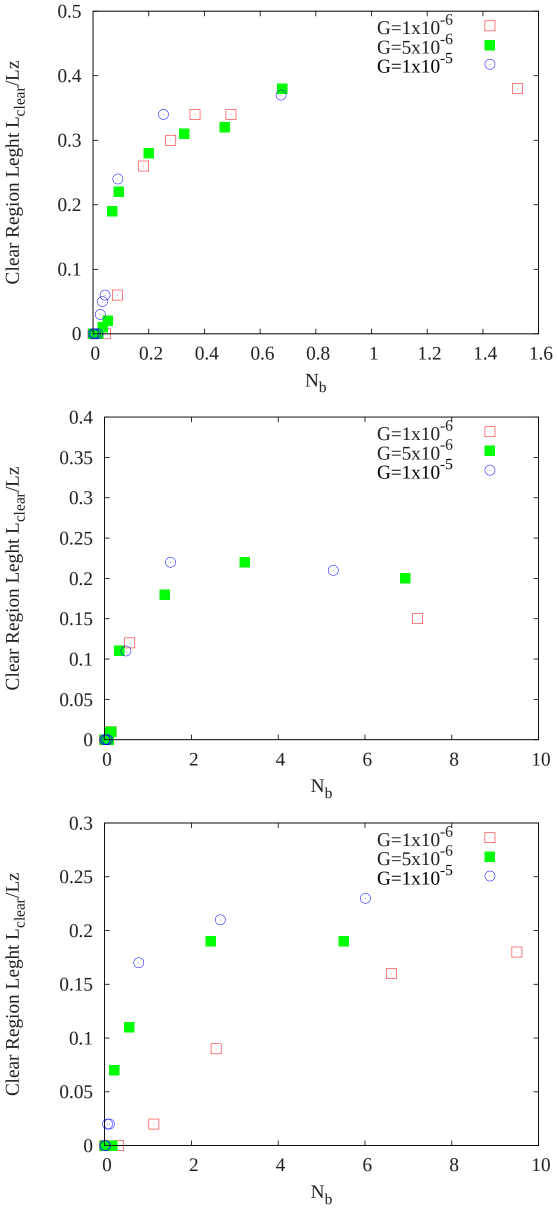

Figure 4.17: The width of clear region for different bulk concentrations $\phi_b = 0.13, 0.26$ and 0.34 from top to bottom with different particle Reynolds number or applied pressure gradients, as demonstrated in fig.4.2.

Particle velocity distribution

For small particle Reynolds number suspension, the particle velocity is almost in accord with the local fluid velocity, especially for colloidal tracer-like particles. So particle velocity shows some information for flow microstructure such as particle distribution. For pure Newtonian fluid flow along the channel, the probability distribution function(PDF) for the fluid velocity is an increasing function defined on [0:1.5] if fluid velocity is normalized by the averaged fluid velocity across the channel, for the exact shape of this PDF function and more details, see Gudmundsson et al[83]. Fig.4.18 shows the particle velocity distribution function for neutrally-buoyant particle suspension with $\phi_b = 0.26$ under different applied pressure gradients or different particle Reynolds numbers. As in this figure and all other figures in this section for particle velocity distribution function, the magnitude of particle velocity is normalized by the maximum magnitude. In Fig.4.18, there are several peaks for the PDF function, which corresponds to high concentration regions with the effect of finite size particles. To the lower end of particle velocity, PDF function has a peak for each case, that means some particles are caged by the wall and the main bulk flow. For other peaks to the higher end of particle velocity, the peaks are compressed to the lower end with increasing particle Reynolds number. At high particle Reynolds number, more particles have larger velocities. Moreover, the peaks of the PDF function follows the trend of the fluid velocity distribution for pure fluid flow along the channel as in Gudmundsson et al[83], especially for higher particle Reynolds number. In fig.4.19, we show the particle velocity pdf for different bulk concentrations, for a neutrally-buoyant particle suspension. Other than the peaks for higher concentrations, the distribution shifts to lower values, with particles dispersing away from the center of the channel. In Fig.4.20, we show a typical pdf for different buoyancy numbers under the same bulk concentration and pressure gradient. We see that, along with increasing buoyancy number, the distribution drifts to lower particle velocity region, and at the highest buoyancy number in the plot the particles all settle to the lower wall with very small velocities due to compaction effects.

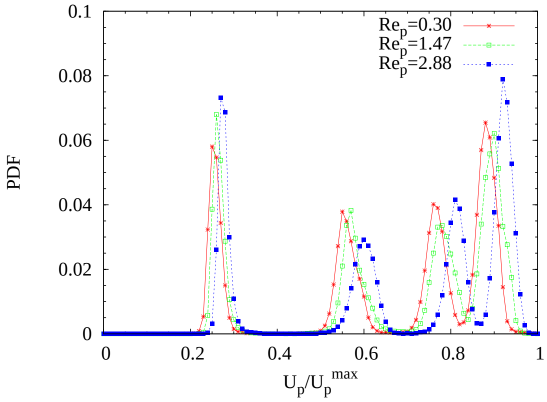

Figure 4.18: Probability distribution of magnitude of particle velocity for neutrally-buoyant particles at bulk concentration $\phi_b = 0.26$, for particle Reynolds number.

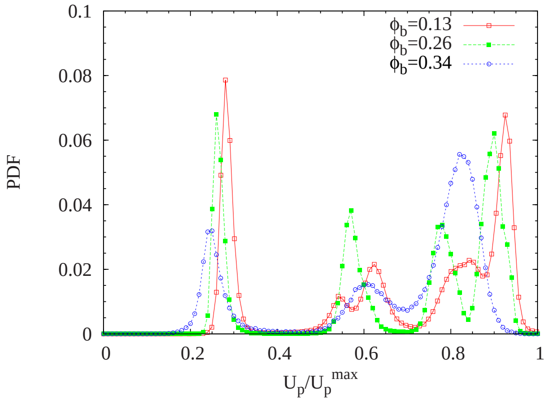

Figure 4.19: Probability distribution of magnitude of particle velocity for neutrally-buoyant particles at different bulk concentrations, under the same applied pressure gradient $G = 5 \times 10^{-6}$.

Particle diffusion process

The particles migrate across the steamlines, and diffuse due to local particle concentration. It is also interesting to check the effect of gravity, particle concentration

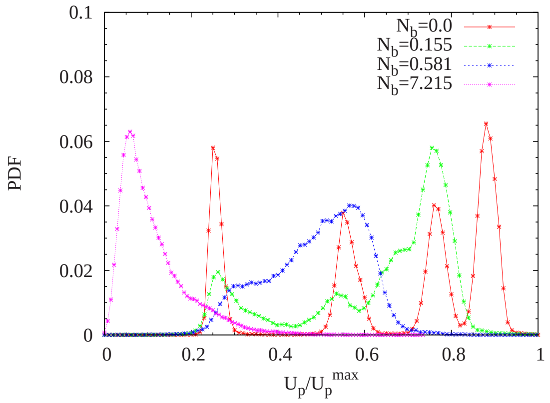

Figure 4.20: Probability distribution of magnitude of particle velocity for neutrally-buoyant particles at bulk concentration $\phi_b = 0.26$, for different buoyancy number under the same applied pressure gradient $G = 1 \times 10^{-6}$.

and Reynolds number on the particle dispersivity in the z-direction. For all plots in this section, the time is measured in the particle diffusion time $t_s = d^2/\nu$, where ν is the kinematic fluid viscosity. Fig.4.21 shows mean square displacement in z- or velocity gradient direction for neutrally buoyant particles at the same bulk concentration for different applied pressure gradient or particle Reynolds number. For a neutrally buoyant particle suspension, the particle dispersivity is larger for higher particle Reynolds number, and this figure displays that for larger flow strength, the particle migration across the streamlines is more prominent due to the effect of fluid inertia. Under the same applied pressure difference, fig.4.22 shows that the particle dispersivity in velocity gradient direction is higher for higher bulk concentration. At higher particle concentration, particle interaction is of much importance for particles in near contact, and this induces the particle migration. In fig.4.23, we show the mean square displacement in z-direction for $\phi_b = 0.26$ for different buoyancy number. As we could see in the figure, the particle dispersivity in z-direction increases with the buoyancy number at the lower end, and then decreases for higher buoyancy number. The reason for the initial dispersivity increase is that some portion of the particles near one wall migrate to lower shear rate region due to the interplay of shear induced migration and higher gravity force. At higher buoyancy numbers, most of the particles deposit to the wall to form an almost immobile particle layer, and that will reduce the particle migration, and hence the particle dispersivity.

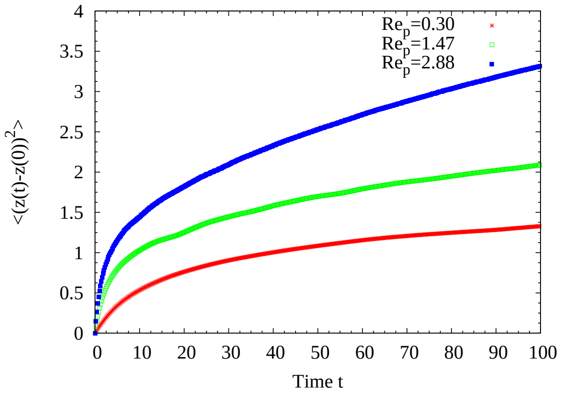

Figure 4.21: Mean square displacement in z-direction for neutrally-buoyant particles at bulk concentration $\phi_b = 0.26$, under different applied pressure gradients.

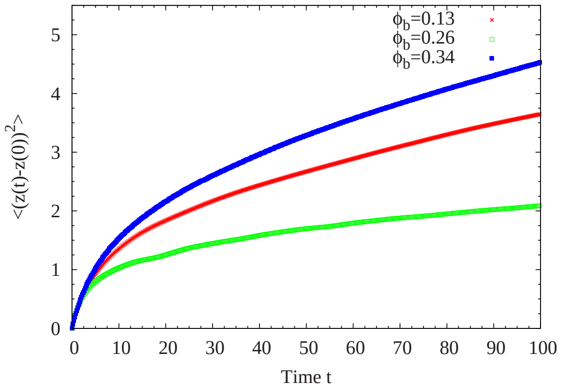

Figure 4.22: Mean square displacement in z-direction for neutrally-buoyant particles at different bulk concentrations $\phi_b = 0.13, 0.26$ and 0.34, under the same applied pressure gradient.

4.3 Surface modification by deposition

The gravitational force has the effect to stabilize the particle deposition and make it flat at large length scales. Based on this observation from our calculations for

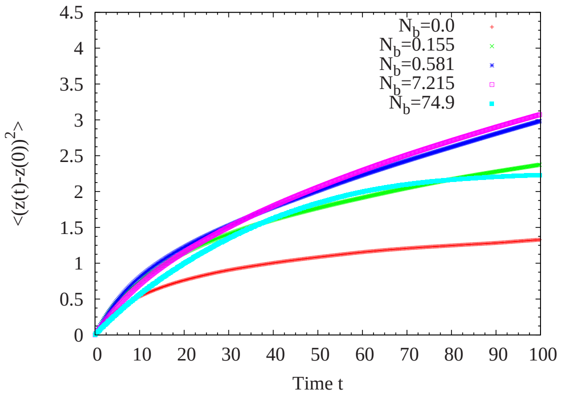

Figure 4.23: Mean square displacement in z-direction for particle suspension at bulk concentration $\phi_b = 0.26$, under same applied pressure gradient $G = 5 \times 10^{-6}$ and different particle buoyancy number.

particle deposition on a planar wall, we are interested in the surface modification due to particle deposition for self-affine surfaces. Fig.4.24 shows the particle deposition layers onto an initial self-affine fracture surface. The self-affine surface is modified to a flatter surface due to deposition under gravity, and in large scale, similar to the surface formation for planar wall, the deposited surface is more or less flat. The height correlation function for this surface is shown in fig.4.25. From this log-log plot, we see that at small length scales up to the order of one particle diameter, the height follows the self-affinity with exponent 0.77, very close to Hurst exponent 0.8 for self-affine surface. At larger length scale, the gravitational effect will modify the particle deposition to a more or less flat surface even for initial rough surfaces. We find the same characterics for other flow conditions.

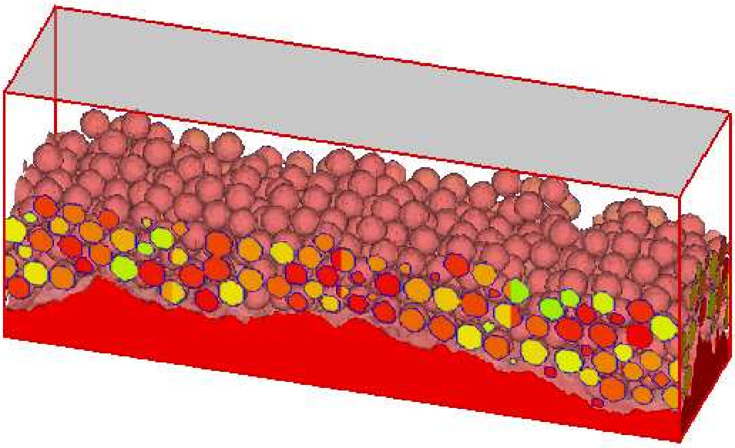

Figure 4.24: The deposition layers onto a self-affine surface in a pressure-driven suspension flow, bulk concentration $\phi_b = 0.20$, pressure gradient applied $G = 5 \times 10^{-6}$ and buoyancy number is $N_b = 7.4$.

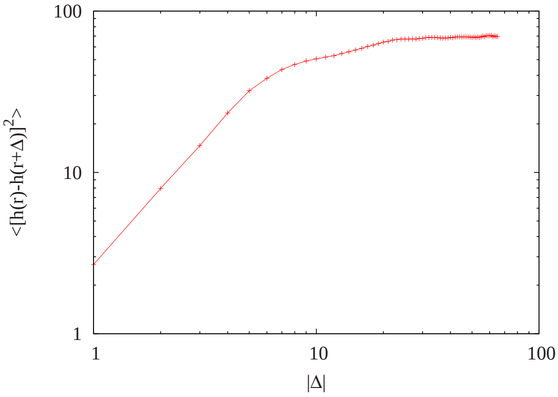

Figure 4.25: Height-height correlation function for the post-deposition surface in fig.4.24.

4.4 Conclusion

In this chapter, we investigate the particle suspension and deposition in different flow conditions and geometry. Macroscopic and microscopic analysis of the suspension flow field for different particle Reynolds number, buoyancy number and bulk concentration. And we also show the surface characterization for deposition bed onto surfaces. All these results could be used in macroscopic modeling and also give us details and physical interpretation of different suspension flow and particle transport.

Chapter 5

Pair particle interaction in shear flow at finite Reynolds number

We discuss the hydrodynamic interactions of two solid bodies placed in linear shear flow between parallel plane walls in a periodic geometry at finite Reynolds number. The computations are based on the lattice Boltzmann method for particulate flow, validated here by comparison to previous results for a single particle. Most of our results pertain to cylinders in two dimensions but some examples are given for spheres in three dimensions. Either one mobile and one fixed particle or else two mobile particles are studied. The motion of a mobile particle is qualitatively similar in both cases at early times, exhibiting either trajectory reversal or bypass, depending upon the initial vector separation of the pair. At longer times, *if* a mobile particle does not approach a periodic image of the second, its trajectory tends to a stable limit point on the symmetry axis. The effect of interactions with periodic images is to produce non-constant asymptotic long-time trajectories. For one free particle interacting with a fixed second particle within the unit cell, the free particle may either move to a fixed point or take up a limit cycle. Pairs of mobile particles starting from symmetric initial conditions are shown to asymptotically reach either fixed points, or mirror image limit cycles within the unit cell, or to bypass one another (and periodic images) indefinitely on a streamwise periodic trajectory. The limit cycle possibility requires finite Reynolds number and arises as a consequence of streamwise periodicity when the system length is sufficiently short.

5.1 Problem formulation and numerical techniques

The calculations in this chapter consider the interaction of two neutrally-buoyant and equal-sized circular cylinders in a two-dimensional linear shear flow between plane walls, or occasionally equal sized spheres in a three-dimensional linear shear flow, with an asymptotic velocity profile $\mathbf{u}^{\infty} = \dot{\gamma} y \hat{\mathbf{x}}$ with shear rate $\dot{\gamma} = 2U_w/W$. A sketch of the system geometry is shown in Fig. 5.1, where the channel width is W, the cylinder or sphere radius is a (we sometimes refer to the diameter $d = 2a$), the wall velocities are $\pm U_w$, the fluid viscosity is μ, and the common density of fluid and particles is ρ. We nondimensionalize length, time, velocity and pressure using scales W, W/U_w, U_w and $\mu U_w/W$, respectively, and the dimensionless form of the continuity and Navier-Stokes equations are

$$\begin{aligned} \nabla \cdot \mathbf{u} &= 0, && (5.1) \\ Re_b \left(\frac{\partial \mathbf{u}}{\partial t} + \mathbf{u} \cdot \nabla \mathbf{u} \right) &= -\nabla p + \nabla^2 \mathbf{u}. && (5.2) \end{aligned}$$

Here the bulk Reynolds number is $Re_b = U_w W/\nu$ ($\nu = \mu/\rho$ is the kinematic viscosity), and the particle Reynolds number based on its radius is $Re_p = \dot{\gamma} a^2/\nu = Re_b \cdot (2a^2/W^2)$. The particle motion is given by Newtonian dynamics:

$$\begin{aligned} M \frac{d\mathbf{U}(t)}{dt} &= \mathbf{F} && (5.3) \\ \mathbf{I} \cdot \frac{d\mathbf{\Omega}(t)}{dt} &+ \mathbf{\Omega} \times [\mathbf{I} \cdot \mathbf{\Omega}(t)], = \mathbf{T} && (5.4) \end{aligned}$$

where M and $\mathbf{I}$ are the mass and moment of inertia tensor of the particle, $\mathbf{U}$ and $\mathbf{\Omega}$ are its linear and angular momentum, and $\mathbf{F}$ and $\mathbf{T}$ are the force and torque acting on it, respectively. The no-slip boundary condition is applied on the surfaces of the particles and walls.

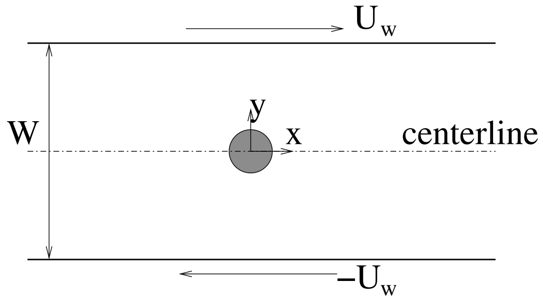

Figure 5.1: A particle rotating in the zero-velocity plane in simple shear flow.

The Navier-Stokes equations for the fluid are solved here by the lattice Boltzmann method [77, 86], from the solution we obtain the force and torque (the linear and angular momentum transferred across the particle-fluid boundary), and then Newton's equations for the particles are integrated. A technical issue arising in the calculations is that all numerical methods are ineffective in resolving hydrodynamic interactions when particles are very close to each other. In grid-based methods in particular, when the gap between particles approaches the grid size there are no fluid nodes in between to provide the lubrication force, and in fact we have difficulties when the gap between particles is less than one to two grid spacings. To avoid particle overlap, we therefore include an artificial short-distance lubrication force. We have explored two methods, due to Nguyen and Ladd [64] and Ding and Aidun [25], and we find essentially equivalent results with both. Further discussion is given in the Appendix.

5.2 Nearby interactions

All of the calculations presented in this chapter use periodic boundary conditions in the streamwise direction, in order to avoid unwanted edge effects. In this section we consider particles which start at relatively small separations where the effects of periodicity should be minimal, and examine larger separations where the effects of periodicity plays a role in Section 5. The precise distinction discriminating between the two cases is actually a non-trivial function of the initial x and y separations, and the Reynolds number as well, and is better represented in a phase diagram. An example is given in Fig. 5.18 below.

5.2.1 Interaction between a fixed and a mobile particle

We first consider the trajectory of a single mobile particle in the presence of a second fixed one. The fixed particle is placed at rest on the centerline (2D) or the zero-velocity plane (3D) of the channel, and the second is released from various initial positions, usually without an initial slip velocity (*i.e.*, a velocity differing from the fluid velocity at that point in the absence of the particle). Both particles have the same diameter d, and we use a channel width $W = 4d$ and length $L = 5W$. Changing these parameters, or allowing for a slip velocity, is observed to alter the details of the trajectories but not the general characteristics of the motion. The calculations use a resolution of $d = 30$ lattice spacings in two dimensions, and $d = 10$ in three. Due to a finite computational budget, most results pertain to two dimensional problems, while three dimensional results are used sparingly for purposes of comparison. For the same reason it is not feasible to examine all possible initial positions for the mobile particle, and we focus on two representative groups, one on the centerline but at variable separation from the fixed particle, and the second at a fixed streamwise separation but with variable lateral (y) position.

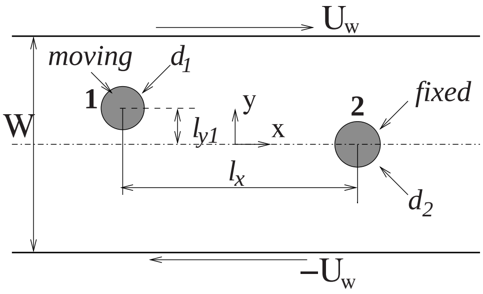

Figure 5.2: Geometry for one fixed and one mobile particle in confined shear flow.

For the case of cylinders originating on the centerline of the channel, the problem geometry is indicated in Fig. 5.2. The centers of the fixed and mobile particle are placed at a distance $\pm l_x/2$ from the origin, respectively, with $l_y = 0$. A representative sample of the resulting trajectories is illustrated in Fig. 5.3, for $Re_p = 0.75$. Although the centerline is a stable point for a single mobile particle, the presence of a nearby fixed particle renders this position unstable. When the mobile particle is placed too close to the fixed one it displaces downwards into the receding part of the flow, and eventually finds a new equilibrium position on the centerline at a larger separation. This behavior is insensitive to small displacements above or below the centerline in the initial position of the mobile particle, and is also not sensitive to whether the particle is released in a fully-developed flow or a fluid at rest, where the wall motion is initiated at the moment of release.

One might be concerned that numerical errors associated with a grid-based method could introduce artifacts, such as a particle subject to a small force failing to move because of numerical fluctuations in the force computation associated with small changes in position. One test of the validity of our results was to vary the initial particle positions by one lattice spacing; this alters the gird-based fluctuations in the force computation but was found to have no effect on the migration dynamics. A second test was to vary the particle size slightly, which again yeilded no significant change in the dynamics.

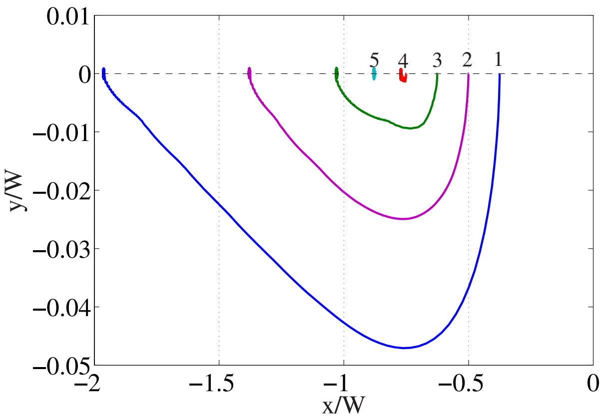

Figure 5.3: Trajectories for a mobile particle released on the centerline in the presence of a fixed particle placed symmetrically with respect to the origin. Cases 1 through 5 refer to initial positions x_0/W = -0.375, ..., -0.875.

The minimum separation between the fixed and mobile particles which separates stable and unstable positions on the centerline varies with Reynolds number, as shown in Fig. 5.4. The closest stable initial separation of the fixed and moving particles, L_c, is found to decrease with Re_p over a finite range, but beyond $Re_p \approx 3.0$ the entire centerline is unstable. At its final position, the mobile particle continues to rotate, with approximately the same angular velocity it would have in isolation. A typical streamline pattern in the stable case is given in Fig. 5.5. There is a substantial recirculation region in the central region between the particles, and some differences in the two streamline patterns around them, reflecting the distinction between a rotating and a fixed particle in shear flow. The fixed particle region has a structure similar to that presented in Mikulencak & Morris [59], which is a consequence of accommodating the no-slip condition on its surface.

In the second group of trajectories we release the moving particle from different lateral positions along a vertical line as indicated in Fig. 5.2 at $l_x = 1.5$ (a value below the critical separation distance in the previous case), while the second particle is fixed on the centerline. As seen in Fig. 5.6, the mobile particle always moves to

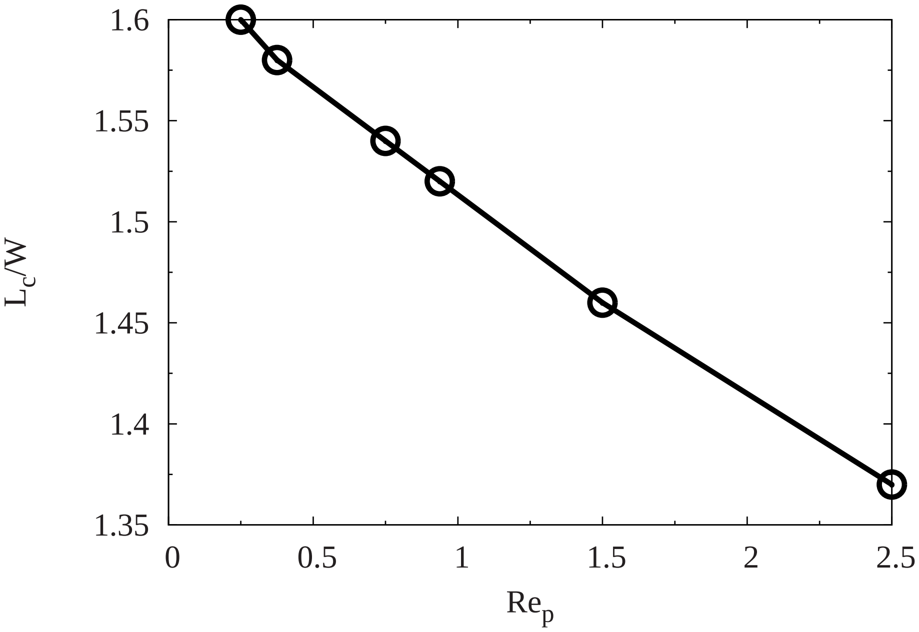

Figure 5.4: Critical separation between stationary and fixed particles for stability on the centerline, as a function of Re_p.

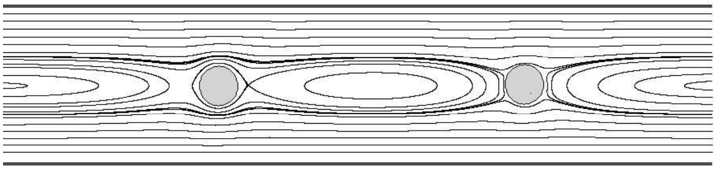

Figure 5.5: Streamlines of a moving particle (left) in the presence of a fixed particle (right) in linear shear flow at $Re_p = 1.5$

the right initially, following the unperturbed linear shear velocity, but subsequently there is a bifurcation in the motion as a function of the initial position. The resulting motion is that suggested by the streamlines around a single particle on the centerline in Fig. 5.5. If the initial displacement relative to the centerline l_y is not too positive, the mobile particle moves downward into the $y < 0$ region of left-moving streamlines, reverses its direction and migrates back to a stable position on the centerline. In the other case, when the initial l_y is large, the particle moves as suggested by the upper streamlines in Fig. 5.5 and bypasses the fixed particle, passing above it while moving to the right. The two trajectories which approach the fixed particle are affected by the lubrication force discussed in Section II, and suffer the largest upward displacement. A calculation at a finer lattice spacing would be needed to verify the detailed behavior, but we do not expect any qualitative modification.

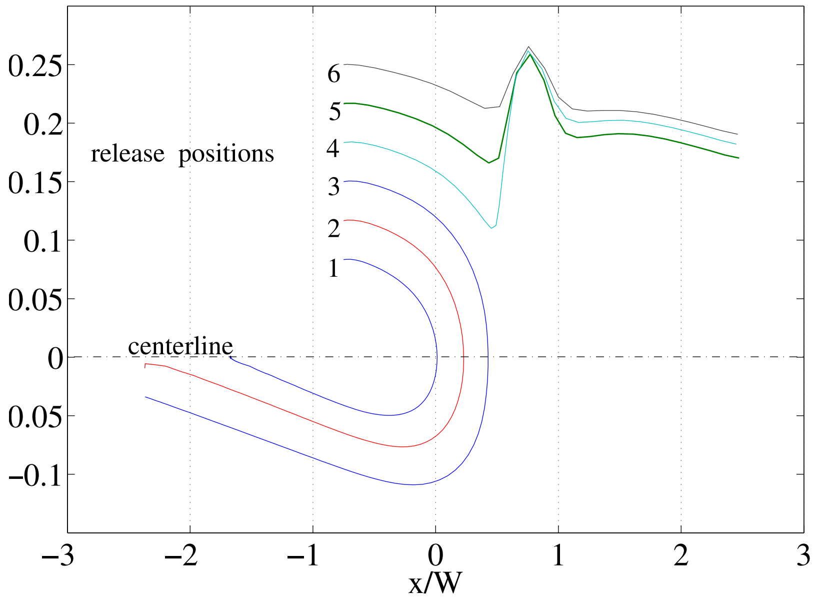

Figure 5.6: Trajectories of a moving particle released at various lateral positions in the presence of another fixed particle in a linear shear flow at $Re_p = 1.5$. The domain length is $L = 5W$, where $W = 4d_1 = 4d_2$, and the fixed particle is at $(0.75W, 0.0)$.

5.2.2 Interaction between two mobile particles

We again consider a two-particle system (of cylinders), but relax the constraints on the second particle and allow it to translate and rotate freely. The geometry of the problem is indicated in Fig. 5.7 and we again focus on two groups of initial conditions.

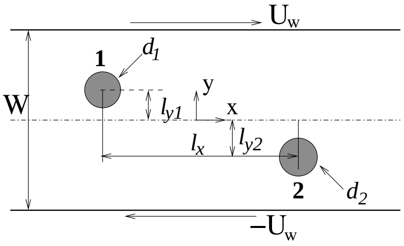

Figure 5.7: Initial geometry for two mobile particles in a linear shear flow; in practice we choose $l_{y1} = l_{y2}$ and $d_1 = d_2 = d$

.

First, we place both particles on the centerline, at variable initial separations l_x, and display some representative particle trajectories in Fig. 5.8. Again, when the particles are placed too close to each other the configuration is unstable, and the particles separate. The leftmost particle moves down and is carried downstream by the lower-region flow, returning to a new stable position on the centerline, while the rightmost particle is displaced up to be transported to the right to its new equilibrium position. The two trajectories are displaced mirror images, as expected, and their shape is quite similar but not identical to that in the case of a single mobile particle. There is again a critical separation beyond which the particles remain in place, rotating on the centerline. As a function of Reynolds number, the critical separation remains at a roughly constant value $6.5d$ up to $Re_p = 3.0$ and $Re_b = 192$, and beyond this value the centerline is no longer a stable position.

Next, we release the particle with a fixed streamwise separation $l_x = 1.5W$ but placed symmetrically off-axis at different values of $l_{y1} = -l_{y2} = l_y$ in the y-direction.

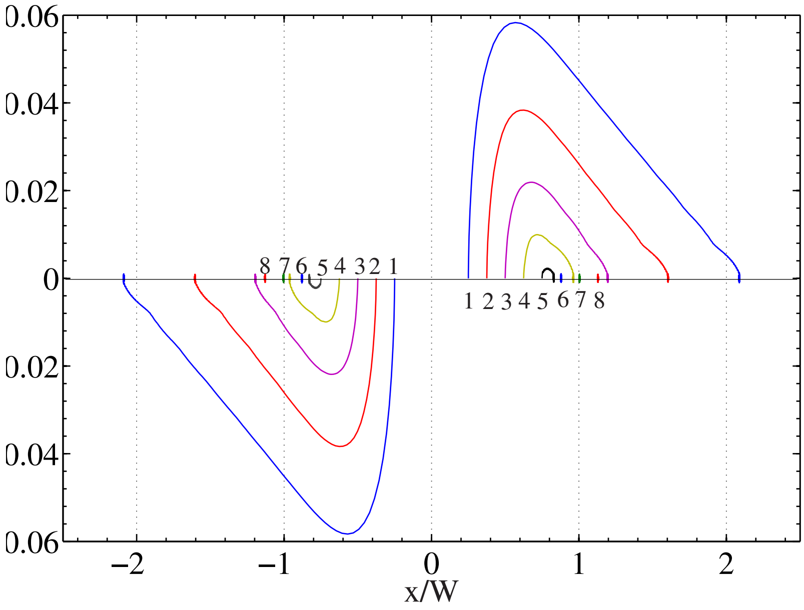

Figure 5.8: Trajectories of two mobile particles initially on the centerline at $(\pm l_x/2, 0)$, $l_x = 0.5W \ldots 2.5W$ for curves 1,...,8, at $Re_p = 0.75$.

As seen in Fig. 5.9, each particle's behavior resembles that of the single mobile particle in the previous section. The symmetry in the trajectories is a consequence of the symmetric shear flow and initial conditions. When the off-axis displacement is small the particles initially move towards each other (carried by the fluid) but subsequently repel and reverse direction, moving downwards across the centerline into fluid moving in the opposite direction, and then move apart before finding new equilibria on the centerline downstream. At larger values of l_y, the initial motion again follows the underlying shear flow but now the particles avoid each other by moving towards the channel walls and then over each other, eventually finding new equilibria in the respective upstream directions. The value $l_y \approx 0.725d$ which distinguishes repelling and bypass trajectories is found to be independent of Reynolds number, over the range studied.

Lastly, an example of the streamline pattern for this flow is given in Fig. 5.10, for the cases of two particle motion on and off the axis. In addition to the recirculating

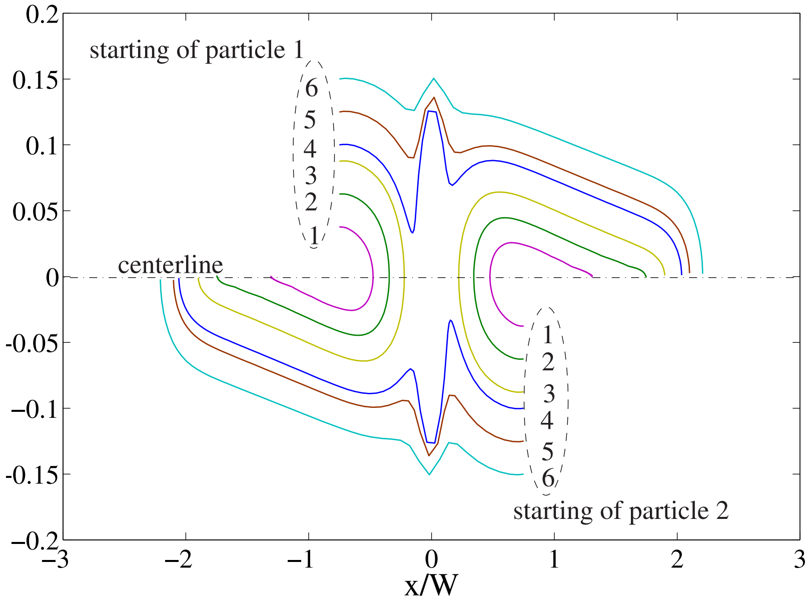

Figure 5.9: Trajectories of two mobile particles in a linear shear flow at $Re_p = 0.75$ and $Re_b = 48$, exhibiting reversal (numbers 1, 2 and 3) or bypass (4, 5, 6). Initially $l_x = \pm 0.75W$ and $l_{y1} = -l_{y2} = 0.03W, \ldots 0.3W$ for cases 1 through 6.

region between the particles present when one is fixed in place, further recirculation zones appear around each particle when both particles are off axis.

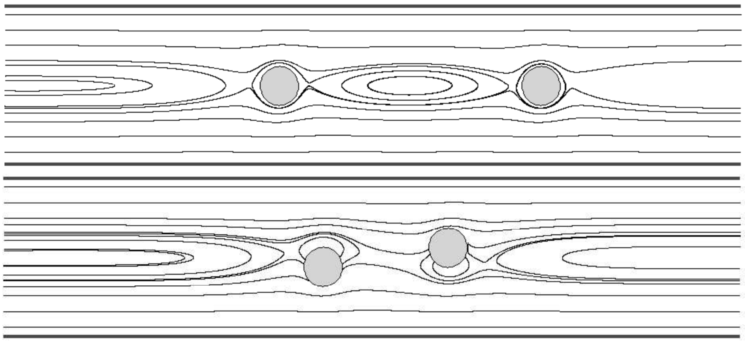

Figure 5.10: Streamlines for two mobile particles in shear flow at $Re_p = 0.75$. (A) both particles on the centerline; (B) particles displaced below and above the centerline, respectively.

5.3 Limit cycle trajectories

As we have seen, in a purely two particle system hydrodynamic interactions tend to push the particles apart, following which they can relax to stable fixed points on the channel axis because the interparticle interaction decays with separation. However, in the presence of streamwise periodicity either particle is effectively always sandwiched between two others, and if the periodic length is short enough, an interparticle interaction is always present. As we shall see, the result is to destabilize the centerline in favor of persistent cyclical motion.

5.3.1 A mobile particle in the presence of a fixed one

The simplest situation involves one mobile particle in the presence of a second fixed one. We consider a system of the same size as above, with aspect ratio $L/W = 5$ containing two particles of diameter $d = W/4$, at a particle Reynolds number $Re_p = 0.75$, and present results for a representative set of initial conditions. Different choices are found to change the details of the trajectories but not the qualitative aspects of the behavior, and generically the moving particle asymptotes to a closed limit cycle. First, we place the fixed particle at the origin, and the mobile particle at $(-2W, y_0)$ for several different choices of y_0; note that the initial separation in x is larger than in the previous section. As seen in Fig.5.11, if the mobile particle starts near the centerline it is immediately attracted to a somewhat rectangular limiting trajectory bounded to either side by the fixed particle and its periodic image. For larger values of y_0, the mobile particle is initially attracted to the centerline but is repelled by the fixed particle, and then carried downstream by the shear flow, whereupon the process repeats due to the presence of the images of the fixed particle. The particle eventually reaches the centerline after one or more “attempts,” but the centerline is unstable in the presence of a fixed particle image, and the mobile particle eventually settles onto a closed limit cycle. The second part of the figure illustrates the fact that the various limiting trajectories are in fact identical within numerical resolution, differing only by a translation in the streamwise direction by a multiple of the length period. While varying the initial spanwise displacement y_0 leads to periodically shifted final states, variation in the streamwise position leads to the same (unshifted) final state. In Fig. 5.12 we show the result when the initial position is $(x_0, 0.1W)$ for various choices of x_0.

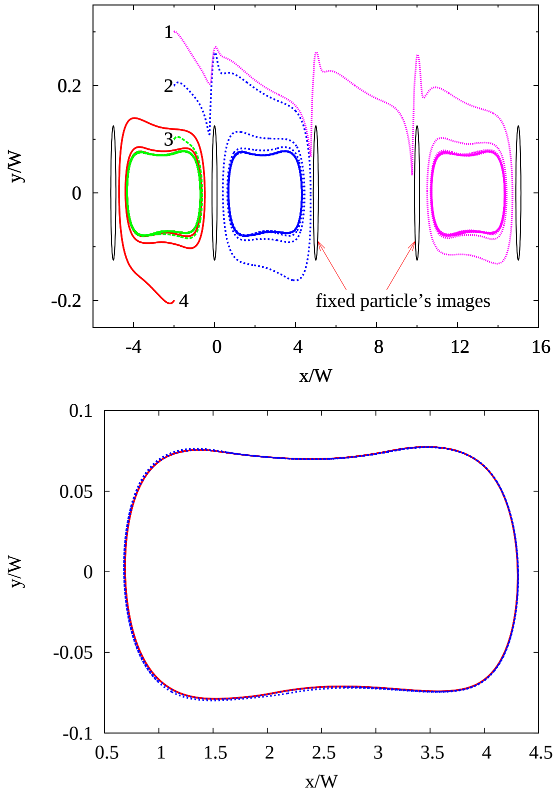

Figure 5.11: Left: Trajectories and limit cycles for a mobile particle in the presence of a fixed one at the origin in a linear shear flow with $Re_p = 0.75$. The system length is $L = 5W$, $d_1 = d_2 = W/4$, and the mobile particle is initially at $(-2W, y_0)$ for spanwise separations $y_0/W =$ (1) 0.3, (2) 0.2, (3) 0.1 and (4) -0.2. Right: Overlay of limit cycles arising from two initial positions 1 and 4, after translation by a multiple of the streamwise period. The deviation is below the numerical resolution of the calculation.

Lastly, we consider the effects of moving the fixed particle off the centerline. In

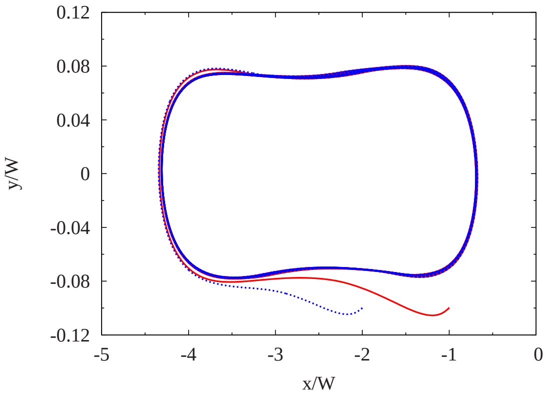

Figure 5.12: Effects of varying the initial streamwise separation on the trajectory of a mobile particle in the presence of a fixed one at the origin. The initial position of the mobile particle is at $(-2W, -W)$ and $(-W, -W)$ for the blue and red curves, respectively. The final limit cycles are identical within numerical resolution.

this case, the limiting trajectory has a different and asymmetric shape, not surprisingly, but the same generic features are present. In Fig.5.13, different trajectories for the mobile particle starting from three different initial positions are shown, along with the superposition of the periodically shifted limit cycles. Thus, the limiting trajectory shape is sensitive to the location of the fixed particle. We have also explored variation of the Reynolds number; this also changes the shape of the limit cycle but not our conclusions, and we do not display the trajectories for other Re_p because they provide no additional insight.

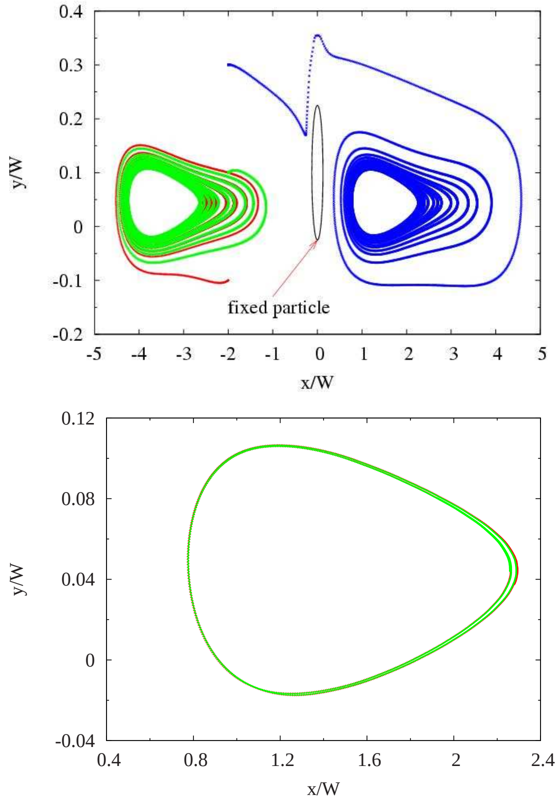

Figure 5.13: Left: Trajectories of a mobile particle in the presence of a fixed particle at $(0.0, 0.1W)$. The initial position of the mobile particle is $(-0.2W, y_0)$ for y_0/W = (1) 0.3, (2) 0.1 and (3) -0.1, respectvely, and other details are as in Fig. 5.11. Right: Overlay of ultimate limit cycles for cases 1 and 3 after translation by one streamwise period.

5.3.2 Two mobile particles

We now consider two mobile particles initially placed farther apart than in Section 4.2, where the motion is now sensitive to the presence of image particles. As in the previous Subsection, the effect of the interactions is to destabilize the centerline leading to limit cycle behavior, but now we find open limiting trajectories as well as closed ones. First we consider initial positions not far from the centerline; in the notation of Fig. 5.7 we choose $l_{y1} = -l_{y2} = 0.05W$, with various values of the streamwise separation l_x larger than those considered in Section 4.2. We again use the same aspect ratio $L = 5W$ and particle size $d = W/4$, but for variety choose a larger particle Reynolds number, $Re_p = 3.0$. As seen in Fig. 5.14, each trajectory asymptotes to a closed limit cycle, and again if we overlay the latter by a shift by one period in the streamwise direction the respective limiting trajectories are identical (figure omitted). The underlying dynamics may be appreciated by labeling positions at equal times along the respective trajectories, shown in Fig. 5.15. The two particles approach the centerline from opposite sides but each is driven across the center by interaction with the other, whereupon they attempt to approach the centerline from the opposite side of the channel, only to be driven past it again by interaction with the periodic image of the other.

If we vary the spanwise initial position for fixed streamwise separation, we again see the two particles asymptoting to pair limit cycle trajectories, provided l_y is not too large: see Fig. 5.16. For each choice of l_y the limit cycles for the two particles are identical after translation by half the length, but the shape of the cycle varies with initial separation, and also differs from that seen in Fig. 5.14. We thus have further evidence that the shape of the limit cycle is sensitive to the initial positions.

If we consider initial positions closer to the channel walls, as in Fig. 5.17, we observe a new type of trajectory which might be thought of as an open limit cycle:

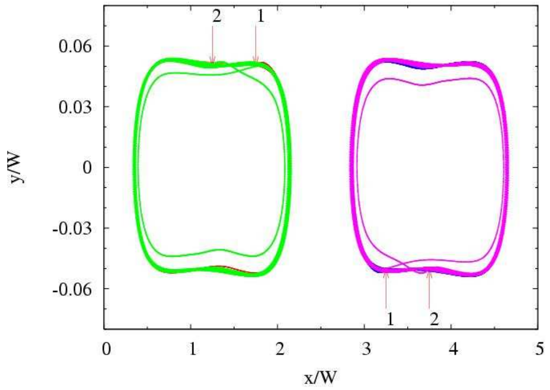

Figure 5.14: Trajectories of two mobile particles in a linear shear flow with $Re_p = 3.0$. The aspect ratio is $L/W = 5$, the particle diameters are $d_1 = d_2 = W/4$, and the initial positions are $l_{y1} = -l_{y2} = 0.05W$ and $l_x/W = 1.5$ and 2.5.

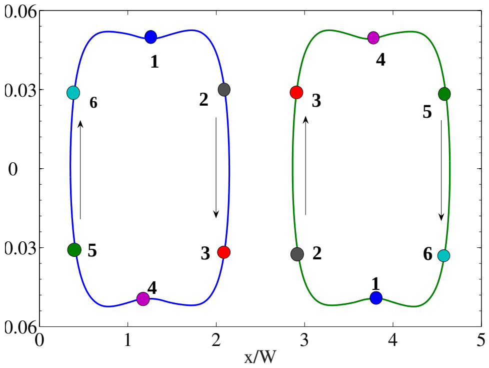

Figure 5.15: Final limit cycles in Fig. 5.14 with equal-time points labeled to illustrate the dynamics.

each particle is prevented from crossing the centerline by its repulsive interaction with the other (or its periodic images), and each moves up or downstream periodically without change. While it is possible that the particles will eventually cross the centerline and settle onto closed trajectories, we see no evidence. Within the accuracy of the calculation, and over about 100 periodic traversals of the system length in some cases, the minimum distance between each particle and the centerline is constant. The distinction between the various final states – fixed points on the centerline and closed and open limit cycles depends only on the initial positions

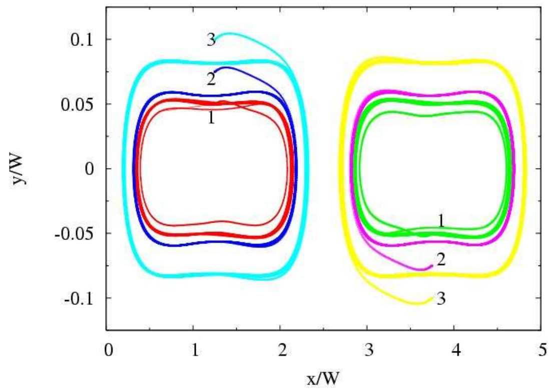

Figure 5.16: Trajectories of two mobile particles in a linear shear flow with $Re_p = 3.0$. The initial positions of the first particle are at $x_0/W = 1.125$ and $y_0/W = (1)\ 0.05$, (2) 0.075 and (3) 0.1, respectively, while the other particle starts at $(x_0 + 2.5W, -y_0)$, and other details are as in Fig. 5.14.

(for a fixed geometry and Reynolds number), and can be summarized in the phase diagram of Fig. 5.18.

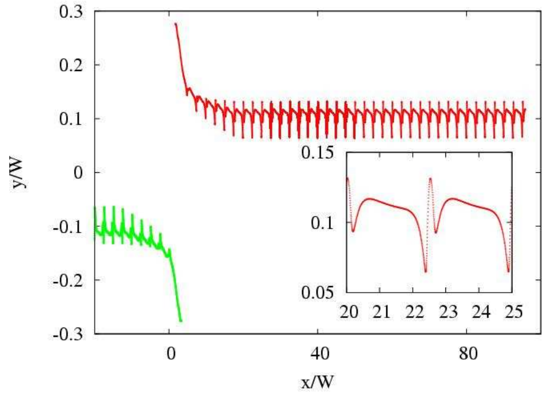

Figure 5.17: Open limit cycle trajectories for initial position near the wall, with $l_{y1} = -l_{y2} = 0.28W$ and $l_x = W$ at $Re_p = 3.0$. The inset shows the motion across one streamwise period at higher resolution, and the second particle trajectory mirrors the first at longer times.

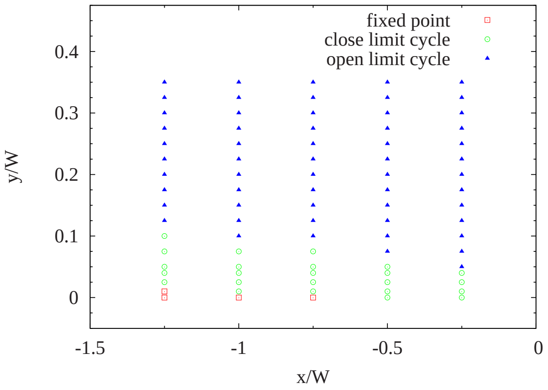

Figure 5.18: Characterization of the final state of two mobile particles interacting in confined periodic shear flow, for the case $Re_p = 3.0$, $L/W = 5$ and $d_1 = d_2 = W/4$, as a function of the initial position (x, y) of one particle (the other starts at $(-x, -y)$).

5.4 Conclusions

We have investigated the hydrodynamic interactions of two circular particles in two dimensions in a bounded periodic linear shear flow, in order to identify distinct regimes of trajectory behavior. The calculations were based on the lattice Boltzmann method, which was tested in this situation by comparison to previous results for rotation speed and migration path for a single particle. The principal new result is the observation of limit cycle behavior for appropriate initial conditions, a phenomenon which arises only at non-zero Reynolds number. In most cases, the behavior of a mobile particle interacting with a fixed particle is qualitatively similar to its behavior in the presence of a second mobile particle. The initial motion of a particle in these situations is to either bypass or be repelled by the second particle. When the particles are initially nearby, *i.e.*, distant from periodic images in the streamwise direction, a mobile particle will settle on and rotate about a stable fixed point on the centerline. If the periodicity length is short enough for image interactions to be significant, the centerline is destabilized, and the asymptotic motion occurs on a limit cycle trajectory. In most cases, the limit cycle is in the form of a closed curve, but for certain initial conditions takes the form of a periodic open trajectory which repeatedly traverses the periodic images of the system.

Appendix: Effects of the interparticle force and the initial velocity

A recurrent problem in the numerical simulation of rigid particle motion in fluids is that numerical errors lead to the inadvertent overlap of different particles. For ideal smooth particles, hydrodynamic lubrication forces should prevent overlap, but in practice the problem is ubiquitous. Although in principle the overlap problem may be resolved by improvements in accuracy and, in particular, reducing the time step in dynamical calculations, frequently the needed refinement is so severe as to hamstring the calculation. A common device, which we have adopted to prevent overlap, is the addition of a repulsive short-range force which acts to prevent collisions between approaching particles. The extra force is intended to overcome the inaccuracy in the lubrication force in the numerical calculations when there are too few fluid nodes between the particles, and further general discussion may be found in references [3, 49].

In this chapter we use the force parametrization due to Nguyen and Ladd [64], and a representative example of its implementation is shown in Fig. 5.19. A fixed particle is at the origin, and a mobile particle is released from $(-1.5W, 0.183W)$ at $Re_p = 3$. The form of the force law is [93]

$$\mathbf{F}_{lub} = -\frac{3}{2}\pi\mu\left(\frac{a_1 a_2}{a_1 + a_2}\right)^{3/2}\left(\frac{1}{h^{3/2}} - \frac{1}{h_c^{3/2}}\right)\left(\mathbf{U}_{12}\cdot\hat{\mathbf{R}}_{12}\right)\mathbf{R}_{12}, \qquad (5.5)$$

where $\mathbf{U}_{12} = \mathbf{U}_1 - \mathbf{U}_2$ is the relative velocity, $h = |\mathbf{R}_{12}| - a_1 - a_2$ is the gap between the particles' surfaces, with $a_{1,2}$ the two radii, $\hat{\mathbf{R}}_{12} = \mathbf{R}_{12}/|\mathbf{R}_{12}|$, and the critical parameter is the cutoff distance h_c beyond which the force no longer acts. The figure indicates that the extra lubrication force only weakly affects the trajectory of the mobile particle after the interaction with the fixed particle. After the interaction, the basic hydrodynamic characteristic of the trajectory is captured, namely the fixed point on the centerline. For two mobile particles, the behavior is similar. As mentioned above, mobile particles select the bifurcation in their trajectories (the choice between repulsion and bypass) before this interparticle force takes effect. Moreover, other forms of the interparticle force law [25] have also been tested in various configurations arising here, and similar results are obtained without damage to the hydrodynamic characteristics.

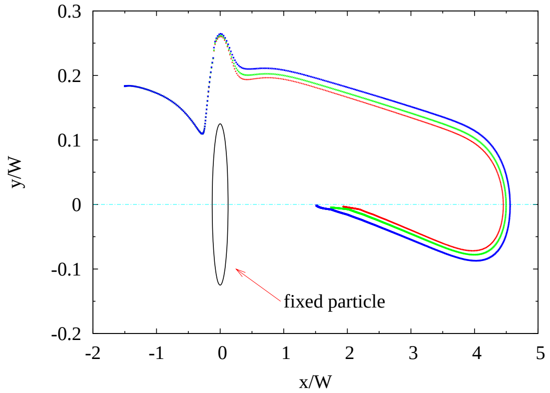

Figure 5.19: Effect of the lubrication force on mobile particle trajectories. The three curves refer to cutoff values h_c = (1) 0.5, (2) 10. and (3) 1.5, respectively, in the force law (5.5), and the final state is relatively insensitive to the value. The flow configuration is described in the text.

A second technical issue concerns the initial conditions on the particle. Physically, there are two obvious experimental protocols, in which either (1) the particle and fluid are initially at rest in a Couette cell, and wall motion commences at some time, or else (2) the fluid is set into motion and after a steady state is reached the particle is placed at rest in the fluid. From a computational point of view, another convenient choice might be (3) place the particle in a fully-developed flow field, but ramp up the force on it from zero to the value given by the fluid flow. In Fig. 5.20 we compare the trajectories resulting from these three choices, as applied to the same configuration as just described, except that the initial position is $(-2.5W, 0.2W)$. In all three cases the same form of inter-particle force is incorporated with the same effective force range. The key feature in the result is that the trajectory asymptotes to the same limit cycle in all cases.

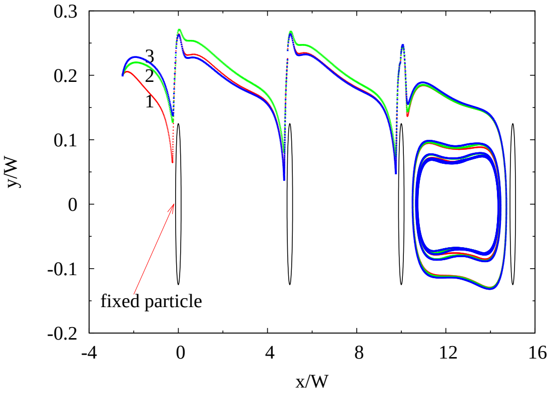

Figure 5.20: Trajectories of mobile particles in mobile to fixed particle interaction in linear shear flow with the three different initial conditions discussed in the text. A particle is fixed at the origin, a second mobile particle is released from $(-2.5W, 0.2W)$, and the domain length is $L = 5W$. Trajectories 1,2 and 3 refer to the choices of initial conditions described in the text.

Chapter 6

Future work and conclusion

When process design and analysis in industrial applications involves flow and particle transport, it is preferable to model the suspension at a macroscopic level. There are two principal issues in this macroscopic modeling. One is the ensemble averaging of the motion of the suspension materials, which provides the smoothed average behavior that a macroscopic model my hope to capture. The second is the rheology of the suspension, which is necessary in macroscopic modeling to describe the material response to driving forces and flow kinematics. in addition, for particle transport processes such as deposition and re-entrainment, the interaction between particles and the bounding walls is of important for modeling purpose. In this chapter, we will discuss these issues further.

6.1 Rheology and modeling of particle suspension flow

6.1.1 Rheology of particle suspension at finite Reynolds number

To model particle suspension as a bulk material flow, it is necessary to incorporate the rheological properties of particle and fluid materials into the suspension model. The rheology of particle suspensions depends on the local particle fraction, particle Reynolds number, and properties of fluid media. One interesting problem, both theoretically and practically, is the bulk shear viscosity at finite Reynolds number for different particle concentrations in the bulk suspension sample. To this end, we have studied a particle suspension system in a simple shear flow induced by two flat plates moving in opposite directions. Figure 6.1 shows the shear viscosity of the particle suspension for different particle concentrations, and different particle Reynolds number. In this figure, we see that even at low bulk concentrations up to 0.1, the relative shear viscosity of particle suspension to pure fluid media is about 1.5 of the viscosity of fluid media for particle Reynolds number at O(1). Moreover, for suspension with finite fluid inertia, the relative shear viscosity is close to the rheological relation in low-Reynolds number flow proposed by Morris and Boulay[61], and higher than Einstein's linear relation with bulk concentration for shear viscosity.

Because this large effect arising from particle concentration and especially from the finite fluid inertia, it is important to investigate sheared suspension for different bulk concentration and particle Reynolds number to sample the whole parameter space, and set up a systematic description of shear viscosity for suspension flow. This result could be further used in macroscopic modeling for various suspension

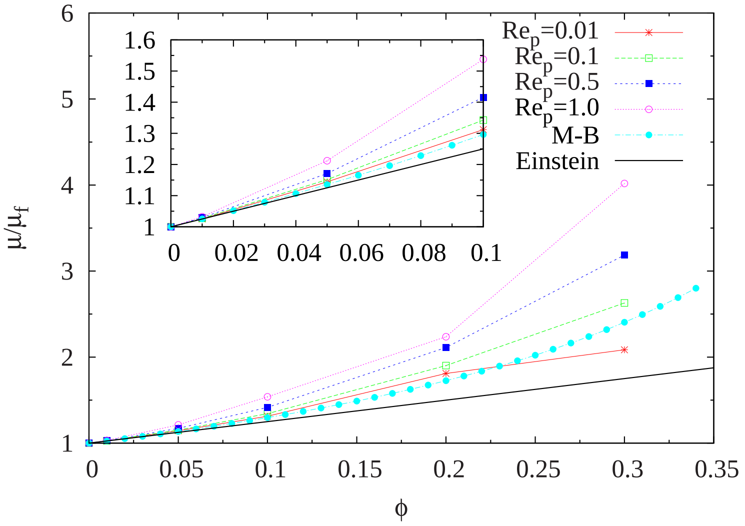

Figure 6.1: Shear viscosity of particle suspension at different bulk concentration and particle Reynolds number.

flow and particle transport processes.

6.1.2 Particle suspension modeling for concentrated particle flow and transport

For macroscopic particle suspension modeling at low Reynolds number, two models have been proposed and developed by different groups to date. The first is the diffusion flux model, initially proposed by Acrivos *et al.*, and the other one is the suspension balance model initially proposed by Nott and Brady and developed further later on by Morris et al. Generally, the suspension balance model has been shown to supercede the diffusion flux model, So here we focus mainly the former model. It is assumed that the rigid particles are non-colloidal, and hydrodynamic interaction is dominant between those particles at low Reynolds number. The description of a two-phase suspension flow requires mass and momentum balances of either the bulk suspension and one of the components, or alternatively, for the continuous media and dispersed phase, respectively. The suspension balance model adopts the former formulation, that is, to consider balance for the mixtures and the particle phase, with the assumption that the dispersed particle phase could be approximated as a continuous media in a ensemble average sense. In the Stokes flow regime (with $Re_p \ll 1$, omitting unsteady and inertia terms in the Stokes' equation), for the mass and momentum balance of suspension mixture we have

$$\nabla \cdot \mathbf{u} = 0, \tag{6.1}$$

$$\nabla \cdot \Sigma + \langle \rho \rangle \mathbf{g} = 0. \tag{6.2}$$

In the above equations, $\mathbf{u}$ is the bulk suspension ensemble-averaged velocity, Σ is bulk suspension stress tensor, and $\langle \rho \rangle \mathbf{g}$ is the mean gravity force applied to the mixture. For neutrally buoyant particles, the gravity term can be reduced to a isotropic hydrostatic pressure contribution to the bulk suspension stress. The particle phase mass balance could be represented as

$$\frac{\partial \phi}{\partial t} + \mathbf{u} \cdot \nabla \phi = -\nabla \cdot \mathbf{j}_\perp, \tag{6.3}$$

where $\mathbf{j}_\perp = \phi(\mathbf{u}_p - \mathbf{u})$ is the particle migration flux relative to the bulk motion. The subscript $\perp$ is used here to emphasize the cross-stream migration particle flux part in the total flux, and $\mathbf{u}_p$, is the particle phase average velocity. To close the above basic suspension balance model for concentrated suspension flow, we need a rheological suspension stress constitutive law. For the suspension continuous phase, the bulk suspension stress is the superposition of two parts, $\Sigma = \Sigma_f + \Sigma_p$, where Σ_f is the fluid contribution and Σ_p is the particle contribution. We could incorporate rheological properties as mentioned in the above section from different experimental measurements and theoretical analysis into the formulation for suspension stress terms. With these rheological property input, we could then solve the whole system of partial differential equations to get the concentration field and velocity, and other related flow quantities. If we could exhaust the whole parameter space including the particle Reynolds number for rheological properties of different suspension material, we could incorporate these rheological properties into this suspension model to calculate particle suspension for finite fluid inertia suspension system, and to extend our knowledge to new level for it.

6.2 Particle-surface interaction

Other than macroscopic modeling for particle suspensions, for particle transport processes such as drug delivery it is also very important to investigate the interaction between particles and surfaces, especially rough surfaces, at different length and time scales.

At the molecular level, with electrostatic interaction considered, we address the Debye length scale and hence double layer effects. In this regime, van der Waals force and electrostatic force must both be considered. Challa *et al.* and Vegeles *et al.* [] have found the forces and torques on a particle translating toward a solid wall or rotating in the vicinity of the wall by molecular dynamics simulations. Their results give us some hints what happen at the molecular scale. In this domain, even without flow a particle experiences a non-zero solvation force and also at such a scale, the no-slip boundary condition may break down very close to the wall. In general, their results match continuum model results well in certain parameter windows. The electrostatic force between particle and surfaces could be calculated by molecular dynamics simulation.

On the other hand, hydrodynamic interactions between particle and surfaces are also important to the boundary conditions in macroscopic suspension flow modeling. When a particle moves through a viscous Newtonian fluid, it is subject to a drag force that resists its motion. In a creeping flow regime, this drag force is proportional to the spherical particle's radius a, the fluid viscosity ν and the particle's velocity U, as $F_0 = 6\pi\mu U a$. Moreover, similar theoretical result exists for particle rotation in a fluid at low Reynolds number. Calculations give the following formula for the torque T acting from the fluid on a sphere rotating with an angular velocity Ω: $T = 8\pi\mu\Omega a^3$. However, when the spherical particle moves toward or away from a solid wall, planar or irregular, the case becomes complicated. If particle moves toward a planar wall the drag force on it also becomes a function of the gap h between the spherical particle and wall. Although the drag force recovers to Stokes drag at $h \to \infty$, the drag increases rapidly close to the wall and diverges as $1/h$ in the limit of $h \to 0$, and the rotation case displays a similar dynamics, which is inconsistent with our common sense. This is mostly because the surfaces of particle and wall in reality are not smooth as in the assumption of theoretical analysis. In reality, the surfaces of wall and particle are irregular, random or correlated in some way. Further research is necessary to clarify the microscopic interaction between particle and surfaces, especially rough surfaces, under different scales, and scale these results up or down to a unified frame using different multi-scale analysis techniques, from which we could incorporate more information into our modeling and calculations for different suspension flow in different configuration and different scales.

6.3 Conclusion

In this thesis, we focused on three different problems. The first one is non-Newtonian fluid flow along self-affine fracture channels, or more specifically shear thinning and shear thickening fluids. The microscopic analysis of flow fields and macroscopic properties such as permeability were presented for numerous flow conditions. The second topic is two-particle interactions in simple shear flow with finite fluid inertia.

We found different particle trajectories for different flow configurations, and through these calculations, we tried to understand particle train and cluster formation in shear and Poiseuille suspension flow. The third part is on particle suspension and deposition under gravity in finite Reynolds number fluid flow. We investigate the velocity field and concentration field in Hele-Shaw geometries, and also presented macroscopic flow properties such as fluid flux and particle flux as functions of particle Reynolds number, buoyancy number and bulk concentration of the suspension flow. With all these and future results on rheological properties of suspension material, and more on microscopic description for particle wall interaction, it is hoped to devise a unified framework to describe and solve suspension flow problems in different processes.

Bibliography

[1] P.M. Adler and J.-F. Thovert. *Fractures and Fracture Networks.* Kluwer, Dordrecht, 1999.

[2] C.K. Aidun and E-J. Ding. Dynamics of particle sedimentation in a vertical channel: Period-doubling bifurcation and chaotic state. *Phys. Fluids*, 15:1612, 2003.

[3] C.K. Aidun, Y.N. Lu, and E.-J. Ding. Direct analysis of particulate suspensions with inertia using the discrete boltzmann equation. *J. Fluid Mech.*, 373:287, 1998.

[4] G.K. Batchelor and J.T. Green. The hydrodynamic interaction of two small freely-moving spheres in a linear flow field. *J. Fluid Mech.*, 56:375–400, 1972.

[5] J. Bear. *Dynamics of Fluids in Porous Media.* Elsevier, New York, 1972.

[6] O. Behrend. Solid-fluid boundaries in particle suspension simulations via the lattice boltzmann method. *Phys. Rev. E*, 52:1164, 1995.

[7] B. Berkowitz. Charaterizing flow and transport in fractured geological media:a review. *Advances in Water Resources*, 25:861, 2002.

[8] B. Berkowitz. Charaterizing flow and transport in fractured geological media:a review. *Adv. Water Resources*, 25:861, 2002.

[9] A. Boschan, H. Auradou, I. Ippolito, R. Chertoff, and J.P. Hulin. Tracer dispersion in a non-newtonian fluid flowing in a rough fracture. *Water Resources Res.*, 43:03438, 2007.

[10] S. Bottin, O. Dauchot, F. Daviaud, and P. Mannville. Experimental evidence of streamwise vortices as finite amplitude solutions in transitional plane couette flow. *Phys. Fluids*, 10:2597–2607, 1998.

[11] E. Bouchaud. Scaling properties of cracks. *J. Phys.: Condens. Matter*, 9:4319, 1997.

[12] P.R. Nott & J.F. Brady. Pressure-driven flow of suspensions: simulation and theory. *J. Fluid Mech.*, 275:157–199, 1994.

[13] J.M. Buick and C.A. Greated. Gravity in a lattice boltzmann model. *Phys. Rev. E*, 61:5307, 2000.

[14] J.E. Butler and R.T. Bonnecaze. Imaging of particle shear migration with electrical impedance tomography. *Phys. Fluids*, 11:1982, 1999.

[15] F. Charru and E.J. Hinch. Ripple formation on a particle bed sheared by a viscous liquid. part 1. steady flow. *J. Fluid Mech.*, 550:111–121, 2006.

[16] F. Charru and E.J. Hinch. Ripple formation on a particle bed sheared by a viscous liquid. part 2. oscillating flow. *J. Fluid Mech.*, 550:123–137, 2006.

[17] F. Charru, H. Mouilleron, and O. Eiff. Erosion and deposition of partilces on a bed sheared by a viscous flow. *J. Fluid Mech.*, 519:55–80, 2004.

[18] H. Chen, S. Chen, and W. H. Matthaeus. Recovery of the navier-stokes equations using a lattice-gas boltzmann method. *Physical Review B*, 45, 1992.

[19] S. Chen and G. D. Doolen. Lattice boltzmann method for fluid flows. *Ann. Rev. Fluid Mech.*, 30:329, 1998.

[20] S. Chen, D. Martines, and R. Mei. On boundary conditions in lattice boltzmann methods. *Phys. Fluids*, 8:2527, 1996.

[21] R.P. Chhabra, J. Comiti, and I. Machac. Flow of non-newtonian fluids in fixed and fluidised beds. *Chemical Engineering Science*, 56:1–27, 2001.

[22] B. Chun and A.J.C. Ladd. Inertial migration of neutrally buoyant particles in a square duct: An investigation of multiple equilibrium positions. *Phys. Fluids*, 18:031704, 2006.

[23] D.S. Dandy and H.A. Dwyer. A sphere in shear flow at finite reynolds number: effect of shear on particle lift, drag, and heat transfer. *J. Fluid Mech.*, 216:381–410, 1990.

[24] E-J. Ding and C.K. Aidun. The dynamics and scaling law for particles suspended in shear flow with inertia. *J. Fluid Mech.*, 423:317–344, 2000.

[25] E-J. Ding and C.K. Aidun. Extension of the lattice boltzmann method for direct simulation of suspended particles near contact. *Journal of Statistical Physics*, 112:685, 2003.

[26] G. Drazer and J. Koplik. Permeability of self-affine rough fractures. *Phys. Rev. E*, 62(6):8076, 2000.

[27] G. Drazer and J. Koplik. Tracer dispersion in two-dimensional rough fractures. *Phys. Rev. E*, 63, 2001.

[28] G. Drazer and J. Koplik. Transport in rough self-affine fractures. *Phys. Rev. E*, 66(026303), 2002.

[29] J. Feder. *Fractals.* Plenum, New York, 1988.

[30] J. Feng, H.H. Hu, and D.D. Joseph. Direct simulation of initial value problems for the motion of solid bodies in a newtonian fluid. part 1. sedimentation. *J. Fluid Mech.*, 261:95, 1994.

[31] J. Feng, H.H. Hu, and D.D. Joseph. Direct simulation of initial value problems for the motion of solid bodies in a newtonian fluid. part 2. couette and poiseuille flows. *J. Fluid Mech.*, 277:271, 1994.

[32] Z.G. Feng and E.E. Michaelides. The immersed boundary-lattice boltzmann method for solving fluid-particles interaction problems. *J. Comput. Phys.*, 195:602, 2004.

[33] O. Filippova and D. Hänel. Lattice-boltzmann simulation of gas-particle flow in filters. *Computers and Fluids*, 26:697, 1997.

[34] S. Gabbanelli, G. Drazer, and J. Koplik. Lattice boltzmann method for non-newtonian (power-law) fluids. *Phys. Rev. E*, 72(046312), 2005.

[35] F. Gadala-Maria and A. Acrivos. Shear-induced structure in a concentrated suspension of solid spheres. *J. Rheol.*, 24:799–814, 1980.

[36] E. Guyon, J.-P. Nadal, and Y. Pomeau. *Disorder and Mixing.* Kluwer, Dordrecht, 1988.

[37] R.E. Hampton, A.A. Mammoli, A.L. Graham, and N. Tetlow. Migration of particles undergoing pressure-driven flow in a circular conduit. *J. Rheol.*, 41(3):621, May/June 1997.

[38] A. Hansen and E. Skjetne. High-velocity flow in a rough fracture. *J. Fluid Mech.*, 383:1, 1999.

[39] M.W. Heemels, M.H.J. Hagen, and C.P. Lowe. Simulating solid colloidal particles using the lattice-boltzmann method. *J. Comput. Phys.*, 164:48, 2000.

[40] S. Hou, Q. Zou, S. Chen, G. Doolen, and A. C. Cogley. Simulation of cavity flow by the lattice boltzmann method. *J. Comput. Phys.*, 1018:329, 1995.

[41] P.Y. Huang and D.D. Joseph. Effects of shear thinning on migration of neutrally buoyant particles in pressure driven flow of newtonian and viscoelastic fluids. *J. Non-Newtonian Fluid Mech.*, 90(2-3):159–185, 2000.

[42] E. Guazzelli J.-P. Matas, V. Glezer and J.F. Morris. Trains of particles in finite-reynolds-number pipe flow. *Phys. Fluids*, 16(11):4192, 2004.

[43] J.F. Morris J.-P. Matas and E. Guazzelli. Inertial migration of rigid spherical particles in poiseuille flow. *J. Fluid Mech.*, 515:171–195, 2004.

[44] I. Kim, W.B. Lindquist, and W.B. Durham. Fracture flow simulation using a finite-difference lattice boltzmann method. *Phys. Rev. E*, 67:046708, 2003.

[45] D.L. Koch and R.J. Hill. Fluid mechanics and rheology of dense suspensions. *Annu. Rev. Fluid Mech.*, 33:619, 2001.

[46] C.A. Kossack and A. Acrivos. Steady simple shear flow past a circular cylinder at moderate reynolds number: a numerical solution. *J. Fluid Mech.*, 66:353–376, 1974.

[47] A.J.C. Ladd. Numerical simulations of particulate suspensions via a discretized boltzmann equation. part 1. theoretical foundation. *J. Fluid Mech.*, 271:285, 1994.

[48] A.J.C. Ladd. Numerical simulations of particulate suspensions via a discretized boltzmann equation. part 2. numerical results. *J. Fluid Mech.*, 271:311, 1994.

[49] A.J.C. Ladd and R. Verberg. Lattice-boltzmann simulations of particle-fluid suspensions. *J. Stat. Phys.*, 104:516, 2001.

[50] D. Leighton and A. Acrivos. The shear-induced migration of particles in concentrated suspension. *J. Fluid Mech.*, 181:414–439, 1987.

[51] C.J. Lin, J.H. Peery, and W.R. Schowalter. Simple shear flow round a rigid sphere: inertial effects and suspension rheology. *J. Fluid Mech.*, 44:1–17, 1970.

[52] W. Lin, M.S. Ingber A.L. Graham, J.R. Abbott, and J.W. Leggoe. Hydrodynamic interaction of two neutrally-bouyant smooth spheres suspended in plane poiseuille flow: the bem simulations versus the mor approximations. *Computat. Mech.*, 36:307–319, 2005.

[53] M.K. Lyon and L.G. Leal. An experimental study of the motion of concentrated suspensions in two-dimensional channel flow. part 1. monodisperse systems. *J. Fluid Mech.*, 363:25–56, 1997.

[54] R.S. Maier, R.S. Bernard, and D.W. Grunau. On boundary conditions in lattice boltzmann methods. *Phys. Fluids*, 8:1788, 1996.

[55] B.B. Mandelbrot. *The Fractal Geometry of Nature.* W.H.FREEMAN AND COMPANY, 2000.

[56] J.-P. Matas, J.F. Morris, and E. Guazzelli. Transition to turbulence in particulate pipe flow. *Phys. Rev. Lett.*, 90(1):014501, 2003.

[57] R. Mei, L.-S. Luo, and W. Shyy. An accurate curved boundary treatment in the lattice boltzmann method. *J. Comput. Phys.*, 155:307, 1999.

[58] A.B. Metzner. Flow of non-newtonian fluids: Correlation of the laminar, transition, and turbulent flow regions. *Adv. Chem. Eng.*, 1:77, 1956.

[59] D.R. Mikulencak and J.F. Morris. Stationary shear flow around fixed and free bodies at finite reynolds numbers. *J. Fluid Mech.*, 520:215–242, 2004.

[60] R.M. Miller and J.F. Morris. Normal stress driven migration and axial development in pressure-driven flow of concentrated suspensions. *J. Non-Newtonian Fluid Mech.*, 135:149–165, 2006.

[61] J.F. Morris and F. Boulay. Curvilinear flows of noncolloidal suspensions: the role of normal stresses. *J. Rheol.*, 43:1213–1237, 1999.

[62] J.F. Morris and J.F. Brady. Pressure-driven flow of a suspension: buoyancy effects. *Int. J. Multiphase Flow*, 24(1):105–130, 1998.

[63] N.-Q Nguyen and A.J.C. Ladd. Microstructure in a settling suspension of hard spheres. *Phys. Rev. E*, 69, 2004.

[64] N.Q. Nguyen and A.J.C. Ladd. Lubrication corrections for lattice-boltzmann simulations of particle suspensions. *Phys. Rev. E*, 66:046708, 2002.

[65] J.T. Norman, H.V. Nayak, and R.T. Bonnecaze. Migration of buoyant particles in low-reynolds-number pressure-driven flows. *J. Fluid Mech.*, 523:1–35, 2005.

[66] R.R. Nourgaliev, T.N. Dinh, T.G. Theofanous, and D. Joseph. The lattice boltzmann equation method: theoretical interpretation, numerics and implications. *Int. J. Multiphase Flows*, 29:117, 2003.

[67] eds. P. Dietrich *et al.* *Flow and Transport in Fractured Porous Media.* Springer,Berlin, 2005.

[68] N.A. Patankar and H.H. Hu. A numerical investigation of the detachment of the trailing particle from a chain sedimenting in newtonian and viscoelastic fluids. *J. Fluids Engr.*, 122:517, 2000.

[69] N.A. Patankar and H.H. Hu. Finite reynolds number effect on the rheology of a dilute suspension of neutrally buoyant circular particles in a newtonian fluid. *Int. J. Multiphase Flow*, 28(3):409–425, 2002.

[70] F. Plouraboue, P. Kurowski, J.-P. Hulin, and S. Roux. Aperture of rough cracks. *Phys. Rev. E*, 51:1675, 1995.

[71] G.G. Poe and A. Acrivos. Closed streamline flows past rotating single spheres and cylinders: inertial effects. *J. Fluid Mech.*, 72:605–623, 1975.

[72] P. Poesio, G. Ooms, A.T. Cate, and J.C.R. Hunt. Interaction and collisions between particles in a linear shear flow near a wall at low reynolds number. *J. Fluid Mech.*, 555:113–130, 2005.

[73] D. Qi. Lattice-boltzmann simulations of particles in non-zero-reynolds-number flows. *J. Fluid Mech.*, 385:41, 1999.

[74] D. Qi. Rotational and orientational behaviour of three-dimensional spheroidal particles in couette flows. *J. Fluid Mech.*, 477:201, 1999.

[75] D. Qi. Lattice-boltzmann simulations of fluidization of rectangular particles. *Int. J. Multiphase Flows*, 26:421, 2000.

[76] D. Qi. Simulations of fluidization of cylindrical multiparticles in a three-dimensional space. *Int. J. Multiphase Flows*, 27:107, 2001.

[77] D. H. Rothman and S. Zaleski. *Lattice Gas Cellular Automata.* Cambridge University Press, 1997.

[78] D.H. Rothman and E. Aharonov. Non-newtonian flow (through porous media): A lattice-boltzmann method. *Geophys. Res. Lett.*, 20:679, 1993.

[79] S. Roux, F. Plouraboue, and J.-P. Hulin. Tracer dispersion in rough open cracks. *Transport in Porous Media*, 32:97, 1998.

[80] M. Sahimi. *Flow and Transport in Porous Media and Fractured Rocks*. Editions VCH, Weinheim, 1995.

[81] H. Schlichting and K. Gersten. *Boundary Layer Theory*. Springer, Berlin, 2000.

[82] G. Segré and A. Silberberg. Behaviour of macroscopic rigid spheres in poiseuille flow part 2. experimental results and interpreation. *J. Fluid Mech.*, 14:136–157, 1962.

[83] E. Skejetne, A. Hansen, and J.S. Gudmundsson. High-velocity flow in a rough fracture. *J. Fluid Mech.*, 383:1, 1999.

[84] G. Subramanian and J.F. Brady. Trajectory analysis for non-brownian inertial suspensions in simple shear flow. *J. Fluid Mech.*, 559:151, 2006.

[85] G. Subramanian and D.L. Koch. Centrifugal forces alter streamline topology and greatly enhance the rate of heat and mass transfer from neutrally buoyant particle to a shear flow. *Phys. Rev. Lett.*, 96:134503, 2006.

[86] S. Succi. *The Lattice Boltzmann Equation for Fluid Dynamics and Beyond*. Clarendon Press, 2001.

[87] S.P. Sullivan, L.F. Gladden, and M.L. Johns. Simulation of power-law fluid flow through porous media using lattice boltzmann techniques. *J. Non-Newtonian Fluid Mech.*, 133:91, 2006.

[88] R. Verberg and A.J.C. Ladd. Lattice-boltzmann simulations of particle-fluid suspensions. *J. Stat. Phys.*, 104:1191, 2001.

[89] R.F. Voss. *Fundamental Algorithms in Computer Graphics.* Springer-Verlag, Berlin, 1985.

[90] R.F. Voss. *Fundamental Algorithms in Computer Graphics*, pages 805–835. Springer-Verlag, 1985.

[91] D.A. Wolf-Gladrow. *Lattice Gas Cellular Automata and Lattice Boltzmann Models: An Introduction.* Springer-Verlag, 2000.

[92] Y. Yan, J.F. Morris, and J. Koplik. Hydrodynamic interaction of two particles in confined linear shear flow at finite reynolds number. *Phys. Fluids*, 19(113305), 2007.

[93] X.F. Yuan and R.C. Ball. Rheology of hydrodynamically interacting concentrated hard disks. *J. Chem. Phys.*, 101:10, 1994.

[94] C.M. Zettner and M. Yoda. Moderate-aspect-ratio elliptical cylinders in simple shear with inertia. *J. Fluid Mech.*, 442:241–266, 2001.

[95] Q. Zou and X. He. On pressure and velocity boundary conditions for the lattice boltzmann bgk model. *Phys. Fluids*, 9:1591, 1997.